Modeling and Experimental Validation of Disc and Reed Style Check Valves for Hydraulic Applications

A THESIS
SUBMITTED TO THE FACULTY OF THE GRADUATE SCHOOL
OF THE UNIVERSITY OF MINNESOTA
BY

Anthony Lewis Knutson

IN PARTIAL FULFILLMENT OF THE REQUIREMENTS
FOR THE DEGREE OF
MASTER OF SCIENCE

Dr. James D. Van de Ven

August 2016

Acknowledgements

I would like to express my gratitude to my advisor, Dr. James D. Van de Ven, for his exceptional mentorship. My brother, parents, and grandparents have my most sincere appreciation for their never-ending love and support.

Abstract

The goal of this thesis is to develop a computationally inexpensive, accurate, and practical mathematical model of a hydraulic reed style check valve. While the modeling of disc style check valves is well represented in literature, reed valve modeling research has focused on applications in air compressors and internal combustion engines, where the working fluid has low density, viscosity, and bulk modulus. However, in a hydraulic system, the fluid – namely oil – is dense, viscous, and stiff, contributing additional physical effects that must be considered. Furthermore, the operating pressure in hydraulic systems is higher than in pneumatic systems, creating additional challenges from a structural perspective.

In this thesis, a one degree of freedom hydraulic disc and reed style check valve model were developed using a hybrid analytical, computational, and experimental approach. The disc valve equation of motion was derived from Newton's second law applied to the disc considering forces including pressure, spring reaction, and drag. Euler-Bernoulli beam theory was used to derive the reed valve equation of motion. In each case, the valve flow rate was modeled as quasi-steady orifice flow using an empirical discharge coefficient.

A non-contact method of experimentally measuring check valve position during operation using a laser triangulation sensor (LTS) was developed. An acrylic viewing window was installed in the check valve manifold to allow optical access. To precisely measure position through air, acrylic, and oil, refraction of the laser light was accounted for using Snell's law.

Finally, the disc and reed valve models were validated in the context of a single cylinder hydraulic piston pump across a range of operating conditions. Pump delivery, which is a measure of volumetric efficiency, and check valve position were chosen as the validation metrics. Experimental results showed that both the disc and reed check valve model accurately predicted the timing of valve opening and closing. The disc valve model

predicted pump delivery within 5% of measured values for all cases while the reed valve model predicted pump delivery within 3% of measured values for all cases.

Table of Contents

vi

List of Tables

List of Figures

Chapter 1 Introduction

1.1   Background

Hydraulics are utilized in a wide variety of applications including jacks, metal fabrication, rescue spreaders, car washes, compactors, mobile construction machinery, wood splitters, hydraulic hybrid vehicles, and energy conversion such as a wind or wave power plant. The benefits of hydraulic circuits compared to competing technologies include high power density, low cost, fast response, and durability. According to a 2012 report by Oak Ridge National Labs, in 2008 between 2.0 and 2.9 Quadrillion British Thermal Units (Quads) of energy were consumed by fluid power systems in the United States producing 310 to 280 MMT of CO_2 with a 22% average efficiency. For reference, the United States consumes 100 Quads per year (Love et al. 2012). According to the report "Case studies show that much of this energy is recoverable and there are tremendous opportunities for energy savings." Despite these opportunities, the report states "As large as the [fluid power] industry is, it has had little fundamental research that could lead to improved efficiency since the late 1960s (prior to the 1970 energy crisis)."

The check valve is a passive device that allows uni-directional flow. Check valves are used in a variety of hydraulic circuits and components, including applications requiring fast valve response such as pumps, digital hydraulics, and servo hydraulic circuits. The dynamic performance of the check valve is critical for such systems, having a significant limiting effect on the operable frequencies and volumetric efficiency. Despite the importance of dynamic check valve behavior to system performance, ideal check valve models are often used that respond instantaneously to pressure differentials. Modelers can be almost certain that the accuracy of their system model will be adversely affected by the implementation of an ideal check valve model.

One potential method for systematically improving energy efficiency of fluid power circuits is optimization. The optimal design is that which, for a given set of design constraints and objective function(s), provides the best possible solution. For a given application, there are many possible objective functions including size, weight, energy

efficiency, and power density. There are also many possible constraints including material properties, part geometry, and dimensions. In order to convert input parameters from the solution space into values of the objective function, a model is needed to simulate operation of the system being optimized. Of course, the optimal solution will depend on the assumptions used to develop the model as well as how the objective functions are defined and weighted.

Optimization of a fluid power system demands an accurate system model, which in turn demands accurate component models. Consider, for example, a linkage driven piston pump. Models are required for the piston motion, check valves, transmission lines, and load. Performance of the individual components are typically tightly coupled so that a deficiency in one component model will degrade the system model, resulting in a sub-optimal solution.

In developing a system model, it is desirable to have a model that has a low computational cost and accurately simulates the actual system. Regrettably, these objectives are often competing. Depending on the size of the solution space, it may be necessary to simulate millions of individual designs during an optimization, rendering all but the fastest models impractical. Therefore, 1-D analytical models are often required in place of the decidedly more accurate empirical or computational 2- or 3-D finite element models. Regardless of the modeling approach, validation is required to ensure the model accurately simulates the actual system in terms of the quantities of interest.

Despite the limitations of simplified or ideal component models, their use justified in some cases, as it is not always practical or even possible to model every physical phenomenon in a complex system. The time and cost required to develop and validate a model at relevant conditions are barriers to creating accurate models and thus optimized systems. This thesis contributes to the field of fluid power modeling by evaluating current disc style check valve models, presenting a computationally inexpensive modeling approach for reed style check valves, and presenting a novel technique for experimentally validating check valves and more generally, measuring the dynamic motion of fluid power components during operation. Analytical and empirical techniques are combined in a novel

formalism to achieve the low computational cost of analytical methods with the high accuracy of experimental methods.

Check valves are comprised on three primary components – a moving element, a seat against which the moving element seals when the valve is closed, and a spring to tend the valve toward the closed position. A check valve may operate without a spring by relying on a pressure differential or gravity to close the valve. A stop is typically used to limit the maximum valve opening. The moving element commonly takes the shape of a disc, ball, or poppet. In the case of a reed valve, the moving element and spring are combined in a single element as a cantilever. Figure 1.1 shows a basic schematic of several check valve types. Figure 1.2 shows a reed style check valve.
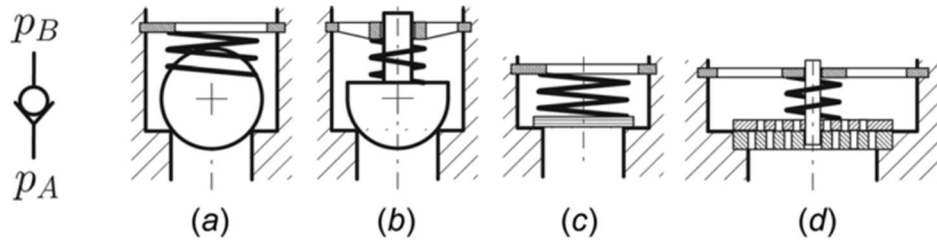
Figure 1.1. Check valve symbol and types: (a) ball valve, (b) poppet valve, (c) plate valve, and (d) multidisk plate valve (Leati et al. 2016)
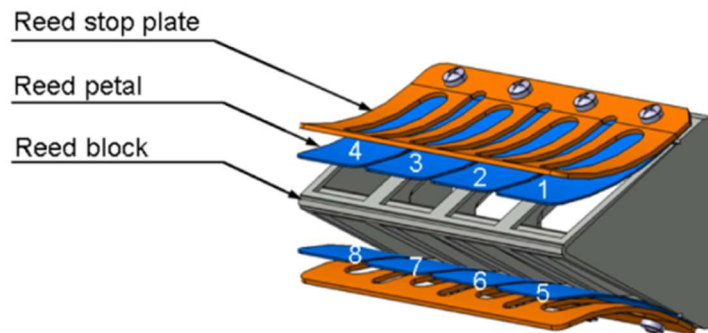
Figure 1.2. Reed valve system of a 2-stroke engine (Jajcevic et al. 2010)

1.2   Literature Review

Broadly, the literature review will be divided into three sections: disc valve modeling techniques, reed valve modeling techniques, and experimental validation techniques. Modeling of each valve type is subdivided into the mechanical and fluid domains followed by a summary of prior literature findings.

1.2.1   Disc Valve Modeling Techniques

There are several techniques of varying complexity available for modeling a check valve. Operation of the check valve may be thought of in terms of two domains: the mechanical or structural domain and the fluid domain. These domains are coupled through fluid-structure interaction. Modeling the mechanical domain is typically accomplished by calculating the forces and moments on the moving valve element and applying Newton's second law to obtain a set of differential equations that describe valve position, velocity, and acceleration. The position and dynamic motion of components in the mechanical domain provide boundary conditions for the fluid domain. Depending on how the disc valve is constrained, motion may be dominated by a single dimension, or multiple degrees of freedom may be necessary to adequately describe the behavior. Methods for modeling the fluid domain include 1-D lumped parameter (Wylie & Streeter 1993), 1-D distributed parameter (Edge et al. 1984), and computational fluid dynamics (CFD) (Xiong & Lumkes 2014; Jalil et al. 2015; Leati et al. 2016). Furthermore, CFD methods may treat the fluid as inviscid or include viscous terms, with the latter choice increasing computation time markedly over the former.

1.2.1.1 Mechanical Domain

The most common method for modeling disc and poppet valve dynamics is to treat the moving element as a 1-D spring-mass-damper (Edge et al. 1984) restricted to a single translational degree of freedom as shown in Figure 1.3. The mass term includes not only

the valve disc, but may also include contributions from the spring and added fluid mass. Damping is provided by the surrounding fluid and may be characterized as viscous at low Reynolds numbers (Edge et al. 1984) or inertial at high Reynolds numbers (Bukac 2002). Damping is also provided by deformation of the spring, but this is typically negligible compared to other sources of damping. The valve seat and stop may also be modeled as spring-mass-dampers that only contribute to valve dynamics during contact (Johnston 1991; Bukac 2002).
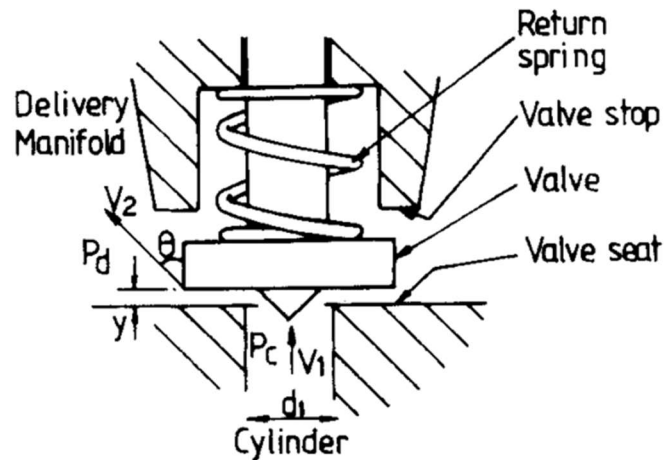
Figure 1.3. Schematic of valve (Edge et al. 1984)

The forcing function of the spring-mass-damper system is the pressure differential acting on the valve face area. The simplest method to calculate the pressure force is to multiply the valve area by the difference between the upstream and downstream pressure. Recognizing that in reality the pressure distribution on the valve is non-uniform, a more accurate method is to determine the relationship between the pressure drop across the valve, ΔP, and the thrust force on the valve, F. To accomplish this, a force coefficient, C_F, may be defined as $C_F = \dfrac{F}{\Delta PA}$ where A is the valve face area (Vaughn et al. 1992). The force can then be calculated as $F = C_F \Delta PA$. The force coefficient may be a function of several variables including valve geometry and lift.

Flow forces also contribute to valve dynamics by means of a steady and transient component (Merritt 1967; Manring 2005). The steady flow force results from a change in

momentum of the fluid as its flow path is altered by the valve (Johnston et al. 1991). Transient flow forces arise from acceleration of the fluid surrounding the valve (Del Vescovo & Lippolis 2006), which can be interpreted as an added inertial force or a decreased pressure force. Transient flow forces are especially difficult to predict as analytical estimates often differ significantly from more rigorous numerical simulations (Del Vescovo & Lippolis 2006). It is common to assume transient flow forces are negligible and omit them from the analysis.

During valve transition, when the gap height is very small, fluid must overcome large viscous forces to fill or evacuate the gap between the disc and the seat. Pressure gradients develop to drive the flow, which oppose valve motion and result in a stiction force. For simple geometries, the stiction force can be calculated analytically by solving the Reynolds equation, which applies to flows where pressure and viscous terms dominate (Hamrock et al. 2004). More complex geometries require a numerical approach to characterize the stiction force (Leati et al. 2016). In some cases, cavitation can occur in the valve gap and must be included in analysis of stiction (Scheidl & Gradl 2016; Roemer et al. 2015). Stiction is most significant when the gap height is small and valve velocity is large.

In cases where the valve disc is not constrained from tilting out of the plane normal to its primary axis of translation, valve motion may be 3-D or 2-D, as shown in Figure 1.4. Unconstrained disc valves have been shown to exhibit definitive tilting motion during operation (Knutson & Van de Ven 2016b). The tilting of the disc can be captured by adding a rotational degree of freedom in the equations of motion (Habing 2005).
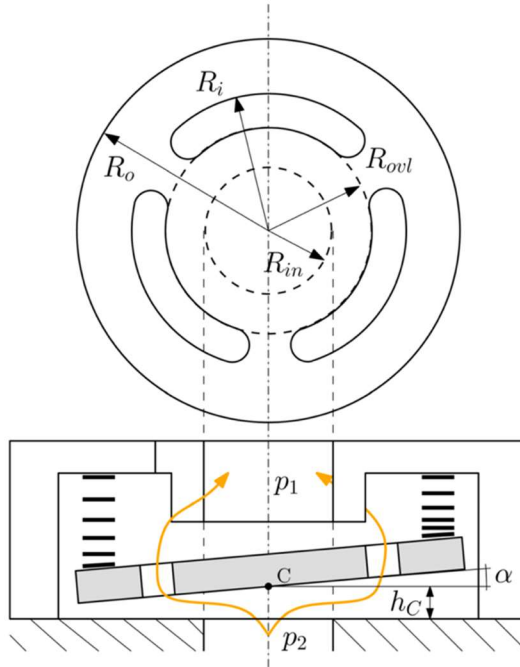
Figure 1.4. Schematic of tilting plate valve (Leati et al. 2016)

1.2.1.2 Fluid Domain

Fluid domain modeling may be accomplished by a number of methods representing a range of complexities. Simplest is a 0-D lumped parameter approach in which fluid is assumed to be at a uniform pressure across large regions of the circuit. The effects of pipe resistance, fluid inertia, and fluid capacitance may be accounted for with a 1-D model. There are two common distributed parameter time domain approaches to solve the partial differential equations (PDEs) that describe 1-D transmission line fluid dynamics.

First is the method of characteristics (MOC) that provides an exact numerical solution by evaluating the PDE at specific temporal and spatial locations (Wylie & Streeter 1993) as illustrated in Figure 1.5. These locations are defined according to strict stability criteria.
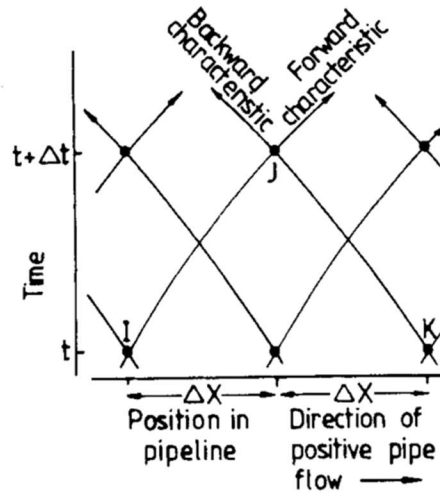
Figure 1.5. Characteristic lines indicating the progress of longitudinal waves in a pipeline (Edge et al. 1984)

Second, the finite element method (FEM) divides the transmission line into smaller elements, each with an inertive, capacitive, and resistive component. The pressure and volumetric flow rate at each element are solved for using either implicit or explicit methods. The FEM approach is significantly more computationally expensive than the MOC. Variable time step integrators can help reduce computation time but numerical stability must be retained by limiting the time step (Sanada et al. 1993).

Higher spatial dimension numerical methods provide a more comprehensive analysis of fluid behavior at the expensive of computational time. Two dimensional planar (Xiong & Lumkes 2014) and axisymmetric FEM has been successfully applied to hydraulic circuits. The three dimensional flow field around a check valve has be solved for with computational fluid dynamics (CFD) to obtain quantities such as pressure and velocity at every grid point in the domain (Leati et al. 2016). By and large, 2- and 3-D computational domains are prohibitively expensive in terms of optimization routines.

Of particular interest in valve modeling are the pressure drop across and flow rate through a check valve. These quantities give information regarding energy efficiency defined as $\eta_e = 1 - \frac{energy\ losses}{energy\ through}$ and volumetric efficiency defined as $\eta_v = 1 - \frac{backflow}{flow\ through}$. The simplest method to model flow through a check valve is to treat it as

quasi-steady flow through an orifice utilizing the steady state orifice equation (Edge et al. 1984). Valve specific numerical or empirical data is typically necessary to develop an accurate relationship between pressure drop and flow rate (Vaughn et al. 1992; Knutson & Van de Ven 2016b). Flow rate through a valve may also be determined using 2-D or 3-D computation fluid dynamics simulations (Xiong & Lumkes 2014; Leati et al. 2016).

1.2.2   Disc Valve Model Findings

Published in 2016, the journal article "Modeling of a Fast Plate Type Hydraulic Check Valve" from the Institute of Machine Design and Hydraulic Drives at Johannes Keppler University in Austria represents the state of the art in computational and empirical hydraulic check valve modeling (Leati et al. 2016). In the article, Leati et al. showed how CFD simulations could be used to develop correlations between pressure and flow rate as a function of valve opening, flow forces and pressure drop as a function of valve opening, and leakage as a function of pressure differential. They found that flow forces, which include drag and viscous friction, were found to account for 20% of hydrostatic forces at small valve openings, while having a limited contribution at larger openings. This modeling approach combines the accuracy of CFD analysis with the computational speed of correlations.

A study of leakage and stiction was conducted by Leati et al. using CFD to characterize the pressure distribution around the disc during stiction events (Leati et al. 2016). Leati et al. also identified the importance of imperfections in seat geometry in determining leakage and stiction. Figure 1.6 illustrates the variation in gap height resulting from disc deformation in the case of an imperfect seat. Using laminar flow theory, the measured leakage was used to determine the effective gap height for use in leakage and stiction modeling. A cushioning groove has been proposed as a solution to reducing stiction (Scheidl & Gradl 2015; Leati et al. 2016).

$$\Delta p = 0 \qquad\qquad \Delta p = max$$

$$h = h_{contact} \qquad\qquad h = h_{min}$$
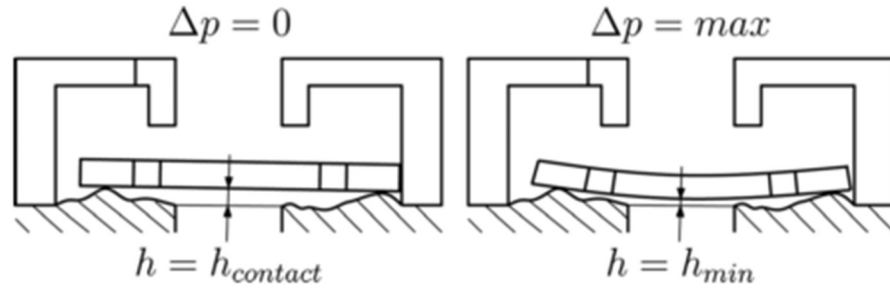
Figure 1.6. Schematic of the plate elastic deformation in case of imperfect surface

Research has shown that instabilities in an unconstrained disc result in wobbling behavior (Knutson & Van de Ven 2016b). A simple stability analysis was conducted for an unconstrained disc, which found that gap forces tend to destabilize the disc (Leati et al. 2016). Modeling the behavior of an unstable valve is too complex for the simple, computationally inexpensive model that is needed for design and optimization. Therefore, instability and its effects must be either minimized or well understood.

1.2.3 Reed Valve Modeling Techniques

Much of the previously discussed mechanical and fluid domain modeling for disc style check valves also applies to reed type check valves. The primary difference is that reed valve motion requires two dimensions to characterize if only flexure is considered and three dimensions if torsion is allowed. Therefore, quantities such as flow area are complicated as they depend on the 2- or 3-D deflection of the reed.

1.2.3.1 Mechanical Domain

A notable characteristic of reed valves is that a spring, mass, and damper are combined into a single element. As such, valve behavior is heavily dependent on material properties and geometric parameters. During deformation, the bending moment varies along the length of the reed, while shear forces vary throughout the thickness and length.

Thus, spring, inertial, and damping forces have not only temporal but spatial dependencies so that reed valve dynamics cannot be described by a single ordinary differential equation without simplifying assumptions.

Several models exist that each use a set of simplifying assumptions to aid in the analysis of beam motion, including Euler-Bernoulli, Rayleigh, Shear, and Timoshenko beam theory (Han et al. 1999). The simplest of these models is Euler-Bernoulli beam theory which describes dynamic beam motion with a single, partial differential equation. Analysis may be further simplified by only considering a single mode of vibration such that the displacement as a function of time and space can be separated into the product of the mode function, which depends only on spatial location, and the displacement at a single point on the beam which depends only on time. Then, the equation of motion reduces to a 1-D ordinary differential equation (ODE) that describes the motion of a single point on the beam as a function of time as illustrated in Figure 1.7. Motion of the rest of the beam can be related to the known point through the mode function to determine quantities such as flow area (Tarnopolsky et al. 2000). Calculation of the equivalent force, F_{eq}, is a non-trivial task for non-uniform force distribution.
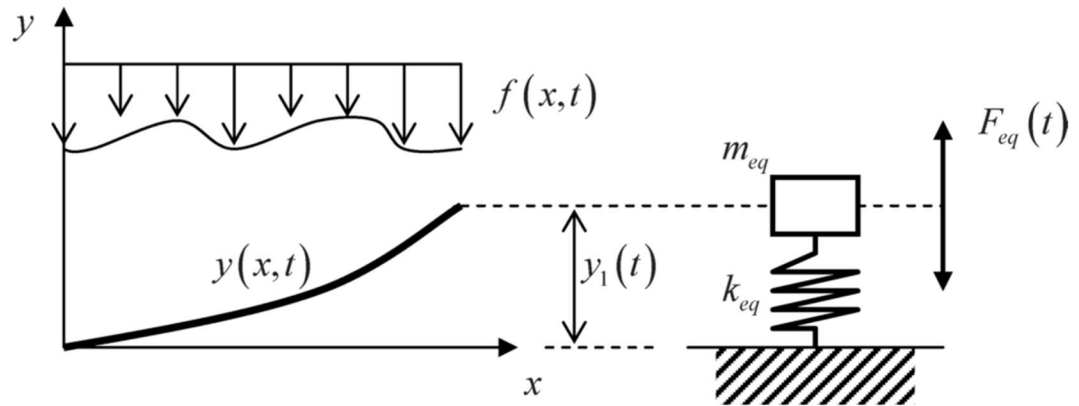
Figure 1.7. Beam model and equivalent mass-spring model (Baudille et al. 2009)

Rather than seek a 1-D ODE to describe beam motion, a finite element method may be pursued, resulting in a problem of the form $M\ddot{x} + C\dot{x} + Kx = f$ where x is the position matrix, f is the forcing function matrix, and M, C, and K are the mass, damping, and

11

stiffness matrices (Baudille et al. 2009). A schematic of an FEM reed model is shown in Figure 1.8. The forcing function matrix can be determined through CFD simulations which calculate the pressure field around the reed (Battistoni & Grimaldi 2005). One advantage of the finite element method is the ability to model more complex reed geometries compared to beam theory, for which a non-uniform cross sectional area greatly complicates analysis.
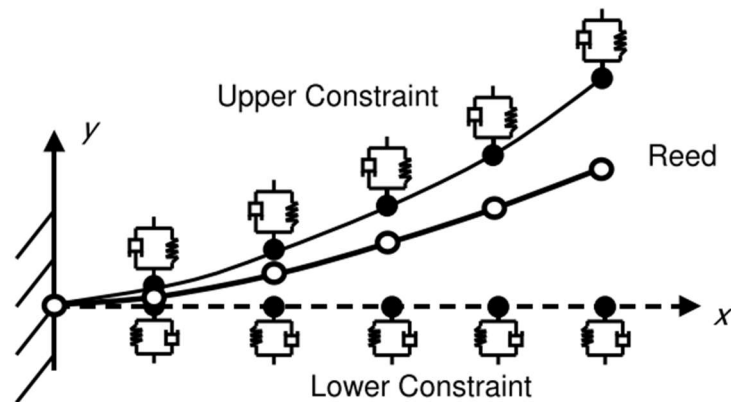
Figure 1.8. Schematic of the FE model of the reed valve with geometrical constraints (Battistoni & Grimaldi 2005)

1.2.3.2 Fluid Domain

Fluid domain modeling of reed valves follows the same general approach as was discussed for disc valves. Literature on reed valves is dominated by applications in internal combustion engines (Dave et al. 2004; Zeng et al. 2004; Battistoni & Grimaldi 2005; Rothbauer et al. 2007; Baudille & Biancolini 2008; Angeletti et al. 2009; Jajcevic et al. 2010) and compressors (Costagliola 1949; Soedel & Cohen 1976; Ferreira et al. 1989; Machu et al. 2004) where the working fluid is a gas. Research on reed valves in hydraulic applications is scarce. As a result, modeling techniques for reed check valves utilize compressible gas flow theory, which is not applicable to hydraulics. The density of air is significantly lower than that of hydraulic oil so inertial effects such as flow forces and added fluid mass are much less important and often neglected. Also, air has a dynamic

viscosity several orders of magnitude lower than oil so viscous effects that are negligible in air systems may become important in hydraulic systems. Thus, despite comprehensive literature on reed valves, further research is needed to characterize reed valve operation in stiff, dense, viscous fluids, such as hydraulic oil.

1.2.4 Reed Valve Model Findings

Reed valve literature findings predominantly concern system models that rely on the use of CFD to provide boundary conditions for an analytical or FEM valve motion models and compute flow rates. Good agreement between predicted and measured flow rates, pressures, and valve motion has been achieved. The need for a computationally inexpensive model has been identified by researchers as illustrated by the following quote (Battistoni & Grimaldi 2005):

> *A strongly non linear behavior of the system emerged by the simulations. In order to predict possible optimized configurations, a careful choice of the target and an extensive use of the simulation tool (due to its short computing time) are recommended. Moreover, as a consequence, the use of an optimization strategy, based, for example, on design of experiments, genetic algorithms or other methods, could entirely exploit the potentialities of the code.*

Several research articles have successfully addressed the need for a computationally inexpensive model by modeling reed motion as a single degree of freedom system and relating quantities such as flow area to said single dimension (Zeng et al. 2004; Knutson & Van de Ven 2016a).

Reed valve literature has focused on applications involving air which has a relatively low density and viscosity. Because of this, flow forces and stiction have been studied very little in the context of reed valves. Due to the shape of a deflected reed and varying gap height, analysis of these forces is expected to be more difficult than in the case

of a disc valve. Most analyses of stiction in cantilevers has been in MEMS applications where motion is not excited by pressure driven flow. Further, the cantilevers that have been considered are primarily uniform and the surfaces do not have holes or slots as found in a reed valve. Therefore, current literature is not adequate to model the stiction affect in reed valves. Such analysis is outside the scope of this thesis but is recognized as an important area for future reed valve research.

1.2.5   Measurement and Validation Techniques

One primary contribution of this thesis is a novel non-interfering method for measuring the dynamic motion of hydraulic system components through multiple interfaces during operation. Several methods have been used to measure check valve position. These methods can be dividing into groups including laser sensors, capacitive/inductive transducers, electrical transformers (LVDT), camera methods, and time integration of acceleration data (accelerometer). A non-exhaustive summary of measurement methods is given in Table 1.1.

Table 1.1. Methods of measuring check valve displacement

Measurement method	Source	Notes
Laser triangulation system (LTS)	(Knutson & Van de Ven 2016b) and the present work	Requires refractive index of interfaces
Laser Doppler Vibrometer (LDV)	(Jajcevic et al. 2010)	Measures velocity
Fiber optic displacement sensor	(Prasad & Woollatt 2000)	Invasive, requires calibration
Capacitance displacement transducer	(Bredesen 1974)	Requires calibration, potentially invasive
Inductive displacement transducer	(Ferreira et al. 1989)	Requires calibration, potentially invasive
Linear variable differential transformer (LVDT)	(Singh & Madavan 1987)	Invasive and mass loading
High speed camera	(Rothbauer et al. 2007)	Requires image analysis and calibration
Endoscope video method	(Ludu et al. 2000)	Requires image analysis and calibration
Stroboscopic video system	(Baudille et al. 2009)	Requires image analysis and calibration
Accelerometer	(Tarnopolsky et al. 2000)	Invasive and mass loading

1.3   Overview

Topics of research in this thesis can be divided into three groups: check valve mathematical model development, experimental validation methodology, and experimental validation results. A disc style check valve model is presented in Chapter 2 followed by a systematic approach for characterizing a general architecture with examples from a specific, commercially available check valve. Chapter 3 describes mathematical modeling of a reed style check valve based on Euler-Bernoulli beam theory. As in Chapter

2, a systematic approach to characterize a general reed valve architecture is described in Chapter 3 with examples from a specific, custom reed valve.

In Chapter 4, a mass conservative piston pump model is developed, in which the check valve models maybe incorporated. Chapter 5 describes the experimental setup consisting of an instrumented hydraulic piston pump capable of measuring valve position, cylinder and load pressure, and pump delivery. A novel technique to measure check valve position in an operating hydraulic system is presented. A series of pumping experiments are described across a range of operating conditions from approximately 600 to 900 rpm and 400 psia (2.76 MPa) to 550 psia (3.79 MPa). Experimental measurements of both the inlet and delivery check valve position and pump delivery are directly compared to predictions from both the disc and reed valve model. Conclusions regarding model capabilities and limitations based on results from Chapter 5 and recommendations for future work comprise Chapter 6 and conclude this thesis.

Chapter 2 Disc Valve Modeling

A check valve is a passive device that allows unidirectional flow. Often, check valves are used in quasi-static situations, such as component bypass and cylinder locking, where the dynamic behavior of the check valve is not critical. However, some applications require fast valve response to pressure changes with minimal backflow, such as pumps, digital hydraulics, and servo hydraulic circuits. While the behavior of a valve could be predicted through a multi-dimensional, multi-domain computational fluid dynamics simulation, this approach is computationally expensive and not appropriate for iterative design and optimization. In this chapter, a dynamic check valve model, developed through a coupled analytical and experimental approach, will be presented.

2.1   Disc Valve Design

The check valve modeled in this chapter is a disc style, although the process for modeling a poppet or ball style valve is similar. One advantage of a disc valve, compared to the poppet or ball, is the low mass of the moving element, which allows for faster response. A picture and diagram of the disc valve are shown in Figure 2.1. The disassembled valve is shown in Figure 2.2.
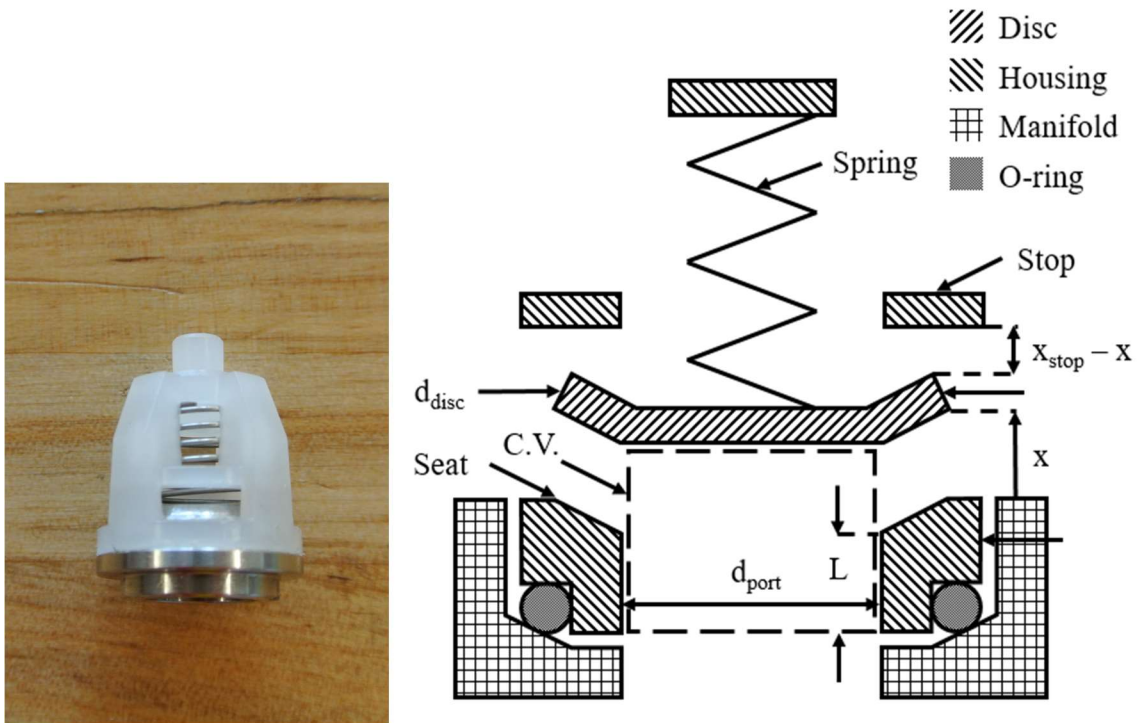
Figure 2.1. Disc check valve

Figure 2.2. From top to bottom: disc valve housing, spring, disc, and seat

During positive flow, fluid enters the control volume through the port, which is a circular opening of diameter d_{port}. Fluid exits the control volume between the seat and disc. Depending on the valve geometry and disc opening, x, the flow may be modeled as either Poiseuille flow or orifice flow. The disc travel is limited by a stop, which allows for a maximum opening of x_{stop}.

2.2   Disc Valve Equation of Motion

The valve motion governing equations are derived by applying Newton's second law to the valve disc and replacing a single, second order differential equation with two, first order differential equations as follows

$$\frac{dx}{dt} = u \tag{2.1}$$

$$\frac{du}{dt} = \frac{F}{m} \tag{2.2}$$

where x and u are the valve position and velocity respectively, F is the net force acting on the valve, and m is the mass to be accelerated. Although the disc shown in Figure 2.1 and Figure 2.2 is not constrained to a single degree of freedom, only 1-D motion of the disc valve was modeled in this work. Details on modeling disc valves with more than a single degree of freedom can be found in the literature (Habing 2005; Leati et al. 2016).

In addition to the disc mass, there is a mass contribution from two additional sources – the spring and fluid. Based on an equivalent kinetic energy analysis, the effective spring mass is calculated to be one third of the total spring mass, m_s. Additionally, as the disc accelerates, it must accelerate a mass of surrounding fluid, m_f. Therefore, acceleration of the disc is computed as

$$\frac{du}{dt} = \frac{F}{m_{disc} + \frac{1}{3}m_s + m_f} \tag{2.3}$$

The forces acting on the valve disc that will be considered are the pressure force, F_p, spring force, F_{spr}, seat and stop contact forces, F_c, fluid drag force, F_{drag}, steady flow force, $F_{flow,s}$, and transient flow force, $F_{flow,t}$. The net force acting on the valve is then calculated as

$$F = F_p + F_{spr} + F_c + F_{drag} + F_{flow,s} + F_{flow,t} \tag{2.4}$$

2.2.1   Added Fluid Mass

As the disc accelerates, a mass of fluid in its vicinity must also be accelerated, created an added mass effect. The added mass depends on several factors including fluid density, disc geometry, and enclosure geometry. Furthermore, the added mass is not expected to remain constant at all times. However, the added fluid mass was found to have little effect on valve behavior so it was neglected in the model. Note that the spring mass contribution is also typically negligible but was included in the model due its ease of implementation.

2.2.2   Pressure Force

Disc motion is driven by a pressure differential across the valve. The pressure force is calculated by integrating the pressure differential over the disc area:

$$F_p = \int_0^{2\pi} \int_0^{R_o} \Delta P(r,\theta) r\, dr\, d\theta \tag{2.5}$$

where ΔP is the pressure differential across the disc. The pressure distribution is spatially non-uniform, particularly between the valve seat and disc bevel where large pressure gradients drive the flow through the valve. A method is sought to either compute the pressure distribution directly or estimate the net resultant pressure force on the disc.

A computational approach such as a 2-D axisymmetric or 3-D transient computational fluid dynamics simulation could provide a high resolution, accurate pressure distribution that could be integrated to yield the pressure force. Such a method would be especially useful as it would eliminate the need to calculate the drag and flow forces, which are simply corrections to account for effects near the disc when pressure is only know a distance from the disc or in the free stream.

Despite the utility of directly computing the pressure distribution, the added computation time would make the valve model impractical for cases such as an optimization routine, which can require millions of simulation runs. Therefore, a lumped parameter approach was taken where large parts of the pressure field are assumed to be uniform. The highly non-uniform region of pressure between the seat and disc was analyzed analytically to keep the model simple. A diagram of the assumed pressure field around a disc valve is shown in Figure 2.3. Since the pressure is known in the free stream, not on the disc surface, drag and flow forces are required to provide corrections for pressure on the surface of the disc.
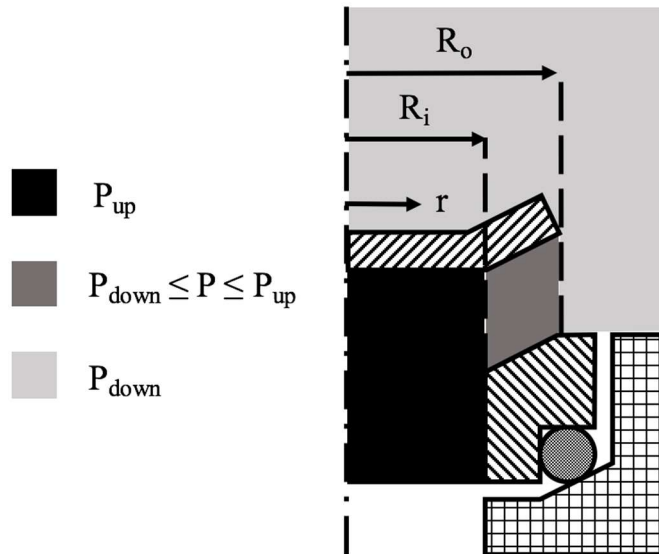
Figure 2.3. Pressure distribution around the disc valve

Two cases were considered for analysis of the pressure field. First, when the disc opening is much smaller than the width of the valve seat, pressure and viscous forces

dominate, resulting in Poiseuille flow between two plates. Second, for larger openings, the valve is treated as an orifice. For both cases, as shown in Figure 2.3, the pressure differential is assumed to be equal to the total pressure drop in the inner radius of the disc so that

$$\Delta P = \Delta P_{u-d}, \qquad r < R_i \qquad (2.6)$$

where $\Delta P_{u\text{-}d} = P_{up} - P_{down}$.

2.2.2.1 Reynolds Equation

In situations where the fluid may be considered incompressible and the pressure and viscous forces dominate others, such as inertia or body forces, the Navier-Stokes equations simplify considerably to a form known as the Reynolds equation, which may be solved analytically for simple geometries. The Reynolds equation, which describes the pressure distribution in a fluid, is commonly used in fluid film lubrication (Hamrock et al. 2004). For small valve openings, the pressure distribution between the seat and disc was determined from the Reynolds equation.

To satisfy continuity when the valve is opening or closing, fluid must fill or evacuate the gap between the disc and the seat. To drive this flow, a pressure gradient develops that opposes the valve motion, resulting in what is commonly referred to as stiction. Consider the disc valve geometry shown in Figure 2.4. The Reynolds equation is valid when $x' \ll R_o' - R_i'$ where $R_i' = R_i/\sin(\theta)$ and $R_o' = R_o/\sin(\theta)$.
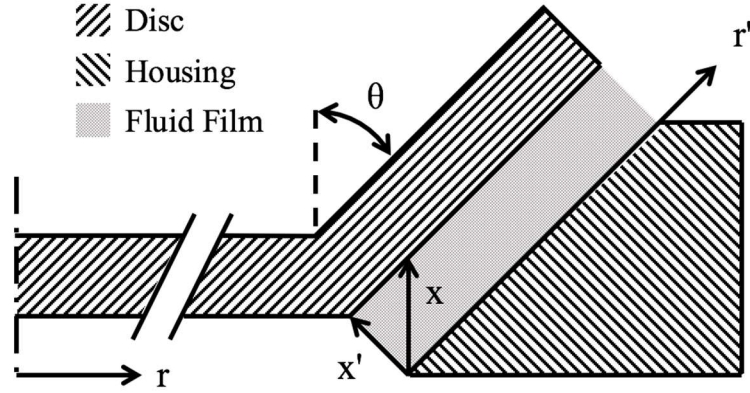
Figure 2.4. Disc valve fluid film

In addition to a relative velocity of the disc normal to the seat, $u' = dx'/dt$, there is a relative translational velocity in the r' direction between the disc and seat that occurs when the disc bevel angle, θ, is not equal to 90 degrees. Combined with pressure driven flow, the result is Couette-Poiseuille flow. Assuming $\partial P/\partial x' = 0$ and the effects of the shear-driven Couette flow contribution are negligible, the Reynolds equation in simplifies to

$$\frac{d}{dr'}\left(r'x'^3 \frac{dP}{dr}\right) = 12\mu r'u' \tag{2.7}$$

Substituting $x' = x*\sin(\theta)$ and $u' = u*\sin(\theta)$ into Equation 2.7 yields

$$\frac{d}{dr'}\left(r' \frac{dP}{dr'}\right) = \frac{12\mu u}{x^3 \sin^2\theta} r' \tag{2.8}$$

Equation 2.8 is integrated twice to give pressure as a function of r':

$$P(r') = \frac{3\mu r'^2 u}{x^3 \sin^2\theta} + A \ln r' + B, \qquad R_i' \leq r \leq R_o' \tag{2.9}$$

23

where A and B are constants of integration that are determined from Dirichlet pressure boundary conditions; $P(r' = R_i') = P_{up}$, $P(r' = R_o') = P_{down}$. To obtain an expression for the pressure differential, the downstream pressure is subtracted from Equation 2.9, resulting in the following:

$$\Delta P(r) \tag{2.10}$$

$$= \frac{\Delta P_{u-d} \ln\frac{R_o{}'}{r'} - \frac{3\mu u}{x^3 \sin^2\theta}\left(r'^2 \ln\frac{R_i{}'}{R_o{}'} + R_i{}'^2 \ln\frac{R_o{}'}{r'} + R_o{}'^2 \ln\frac{r'}{R_i{}'}\right)}{\ln\frac{R_o{}'}{R_i{}'}},$$

$$R_i' \leq r' \leq R_o'$$

Pressure on the disc as a function of the r coordinate is found by substituting $r' = r/\sin(\theta)$, $R_i' = R_i/\sin(\theta)$, and $R_o' = R_o/\sin(\theta)$ into Equation 2.10:

$$\Delta P(r) = \frac{\Delta P_{u-d} \ln\frac{R_o}{r} - \frac{3\mu u}{x^3 \sin^4\theta}\left(r^2 \ln\frac{R_i}{R_o} + R_i{}^2 \ln\frac{R_o}{r} + R_o{}^2 \ln\frac{r}{R_i}\right)}{\ln\frac{R_o}{R_i}}, \tag{2.11}$$

$$R_i \leq r \leq R_o$$

Having determined the pressure field around the disc, the pressure force can be calculated according to Equation 2.5:

$$F_p = \Delta P_{u-d}\pi R_i{}^2 + 2\pi \int_{R_i}^{R_o} \Delta P(r) r \, dr \, d\theta \tag{2.12}$$

Performing integration and separating terms into contributions from Poiseuille flow and valve motion or stiction, the pressure force is expressed as

$$F_p = C_1 \Delta P_{u-d}\pi R_o{}^2 - C_2 \frac{u}{x^3} \tag{2.13}$$

where

$$C_1 = \left[\frac{1 - \left(\frac{R_i}{R_o}\right)^2}{2 \ln \frac{R_o}{R_i}}\right] \tag{2.14}$$

and

$$C_2 = \frac{3\pi\mu}{2sin^4\theta} R_i{}^4 \left[\left(\frac{R_o}{R_i}\right)^4 - 1\right]\left\{1 - \frac{\left(\frac{R_o}{R_i}\right)^2 - 1}{\left[\left(\frac{R_o}{R_i}\right)^2 + 1\right]\ln\frac{R_o}{R_i}}\right\} \tag{2.15}$$

The Poiseuille flow pressure coefficient, C_1, is a function of the disc radius ratio, R_i/R_o only and is between 0 and 1. A plot of C_1 as a function of R_i/R_o is shown in Figure 2.5.
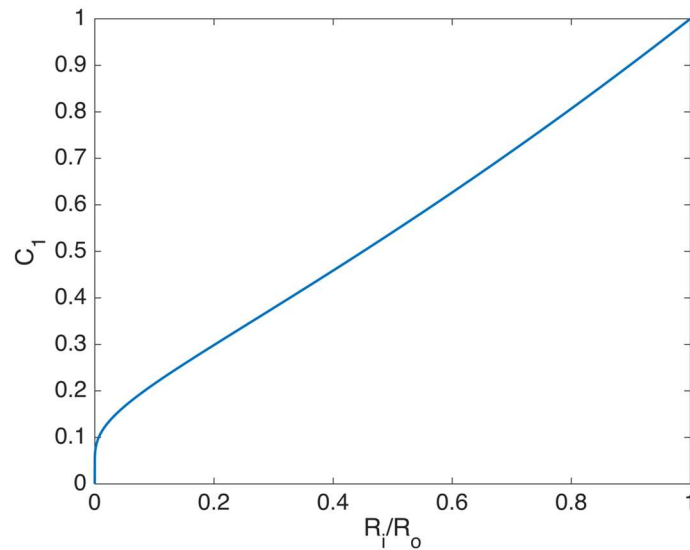
Figure 2.5. Poiseuille flow pressure coefficient, C_1, as a function of the disc radius ratio, R_i/R_o

In the stiction coefficient, C_2, there is a strong inverse dependence on θ. For smaller values of θ, the gap size is small compared to the valve displacement thereby increasing the effect of stiction.

As the gap height approaches zero, the stiction force, $C_2 \frac{u}{x^3}$, which opposes valve motion approaches infinity. Physically this implies a negative pressure in the fluid film, which is not possible. When the pressure of the fluid reaches the vapor pressure, P_{vap}, cavitation will occur; thus, the minimum possible fluid film pressure is the vapor pressure. If all the fluid in the gap is cavitating, the pressure force is limited to

$$F_{p,min} = \Delta P_{u-d} A_{port} + (P_{vap} - P_{down})(A_{disc} - A_{port}) \tag{2.16}$$

Therefore, a simple limiter on the pressure force is as follows:

$$F_p = max\left(F_{p,min}, \quad C_1 \Delta P_{u-d} A_{disc} - C_2 \frac{u}{x^3}\right) \tag{2.17}$$

More complex limiters, such as calculating the pressure field and only limiting the pressure in regions of cavitation, may better predict the pressure force. A more rigorous cavitation model such as the discrete free gas model involves tracking vapor volume and pressure during cavitation events (Wylie, E.B. 1984). However, a detailed analysis of cavitation is beyond the scope of this work.

2.2.2.2 Orifice Regime

When the valve opening is large relative to the sealing width, the pressure differential across the entire disc area was assumed to be ΔP_{u-d} so that $F_p = \Delta P A_{disc}$.

2.2.2.3 Pressure Force Equation

In summary, when the valve gap height is small, the fluid pressure between the seat and disc is influenced by the pressure differential across the valve as well as valve motion.

The pressure gradient that develops to drive Poiseuille flow and the pressure gradient that develops due to valve motion are superimposed to compute the pressure field. The pressure gradient due to Poiseuille flow decreases the pressure between the seat and disc, thereby decreasing the pressure force in the positive x-direction. The pressure gradient that develops from valve motion always acts to oppose valve motion. Since the Reynolds equation is valid for $x' = x*\sin(\theta) \ll R_o' - R_i' = (R_o - R_i)/\sin(\theta)$, the pressure force was determined from the following function:

$$F_p = \begin{cases} max\left(F_{p,min}, \quad C_1 A_{disc} \Delta P_{u-d} - C_2 \dfrac{u}{x^3}\right) \; if \; \dfrac{x\sin^2(\theta)}{R_o - R_i} < \epsilon_0 \\ \Delta P_{u-d} A_{disc} \; otherwise \end{cases} \qquad (2.18)$$

where ϵ_0 is the Poiseuille-orifice flow transition parameter that determines whether flow is modeled as Poiseuille or orifice. ϵ_0 is the maximum ratio of gap height to flow-wise passage length at which flow is modeled as Poiseuille. A value of $\epsilon_0 = 1/10$ is typical to ensure the assumptions of Poiseuille flow hold.

2.2.3   Spring and Contact Forces

The valve spring, seat, and stop provide elastic and dissipative forces that oppose valve displacement and velocity. In this work, elastic forces were modeled as Hookean, where the force is proportion to displacement. Dissipative forces were modeled as viscous damping, where the force is proportional to velocity. The spring force is then given by

$$F_{spr} = -k_{spr}\left(x + x_{pre}\right) \qquad (2.19)$$

where k_{spr} is the spring stiffness x_{pre} is the pre-compression of the spring when the disc valve is closed ($x = 0$). Typically, damping from the spring itself is negligible compared to other forces. This is especially true in the case of a disc valve where fluid damping is significant. For materials or geometries with a non-linear force-displacement relationship,

linearization may be applied over small displacements to yield a linear, Hookean relationship. This is what was done to model the seat and stop elastic forces.

The contact force of the seat and stop is the sum of the elastic and dissipative reaction forces are as follows:

$$F_c = \begin{cases} -k_{seat}x - c_{seat}u, & \text{if } x < 0 \\ 0, & \text{if } 0 \leq x \leq x_{stop} \\ -k_{stop}(x - x_{stop}) - c_{stop}u, & \text{if } x > x_{stop} \end{cases} \qquad (2.20)$$

where k_{seat} and k_{stop} are the spring stiffness of the valve seat and stop respectively and c_{seat} and c_{stop} are the damping coefficients of the valve seat and stop respectively. Note that the seat spring stiffness and damping coefficient may depend not only on the material properties and geometry of the disc and housing, but also the O-ring if there is space between the housing and manifold, as in Figure 2.1.

Determination of the stiffness is straightforward and may be done experimentally or computationally by measuring the force-displacement relationship, or analytically for select geometries. Modeling material damping, however, is more difficult and typically requires empirical data. Furthermore, the fluid film provides an additional source of damping. Underestimating damping causes a physical bouncing of the disc off the seat and stop. Overestimating damping delays valve operation as the disc would be "stuck" to the seat or stop. In an attempt to prevent either extreme, while estimating the damping coefficient with a methodical approach, critical damping is assumed. Consider a damped harmonic oscillator with the following governing equation:

$$\ddot{x} + \frac{c}{m}\dot{x} + \frac{k}{m}x = f \qquad (2.21)$$

Equation 2.21 may also be expressed as

$$\ddot{x} + 2\zeta\omega_n\dot{x} + \omega_n{}^2x = f \qquad (2.22)$$

where ζ is the damping ratio and ω_n is the undamped natural frequency. In the case of critical damping, $\zeta = 1$. Comparing Equation 2.21 and 2.22 and noting that $\omega_n^2 = k/m$, the critical damping coefficient may be expressed as

$$C_{critical} = 2\sqrt{k * m}$$

(2.23)

The mass term in Equation 2.23 is taken to be the combined disc and spring contribution.

2.2.4 Drag Force

Applying dimensional analysis to an object moving through a fluid to determine the functional relationship between the drag force, F_{drag}, and relevant parameters yields the following relationship

$$C_D = \frac{F_{drag}}{\frac{1}{2}\rho u^2 A_{ref}} = f(Re)$$

(2.24)

where ρ is the fluid density, A_{ref} is the reference area, and the Reynolds number is defined as

$$Re = \frac{\rho u L_{ref}}{\mu}$$

(2.25)

where L_{ref} is the reference length and μ is the fluid dynamic viscosity. Experimental data suggests that at low Reynolds numbers, where viscous forces dominate drag, C_D is inversely proportional to Re such that

$$F_{drag} \sim \mu u L_{ref}$$

(2.26)

At high Reynolds numbers where inertial forces dominate drag, empirical data shows that C_D becomes independent of Re such that

$$F_{drag} \sim \rho u^2 A_{ref} \tag{2.27}$$

For the disc valve, the reference area was chosen to be the disc face area. The total drag force was then approximated as the sum of the asymptotic viscous and inertial damping terms with the disc dimeter as the reference length:

$$F_{drag} \cong c_{visc}\mu u d_{disc} + \frac{1}{2}\rho|u|u C_{D,\infty} A_{disc} \tag{2.28}$$

where c_{visc} is the viscous damping coefficient. For reference, according to Stokes' law, a sphere with the diameter as the reference length has $c_{visc} = 3\pi \approx 9.42$.

2.2.5   Flow Forces

Steady and transient flow forces acting on a spool valve were derived by Merritt (1967). In a similar fashion, flow forces acting on a check valve can be derived by applying Reynolds transport theorem to the momentum within a control volume of fluid in the vicinity of the valve, such as that shown in Figure 2.1, as follows:

$$F_{C.V.} = \int_{C.S.} \rho\vec{u}_f(\vec{u}_{f,rel} \cdot \hat{n})dA + \frac{d}{dt}\int_{C.V.} \rho\vec{u}_f dV \tag{2.29}$$

where $F_{C.V.}$ is the net force acting on the control volume and u_f is the fluid velocity. Noting axial symmetry, the net force is in the x-direction. For the purposes of estimating the flow forces, the control volume may be approximated as a cylinder with a length $L + x$ and cross-sectional area A_{port}. Since fluid velocity may be expressed as the volumetric flow rate divided by the cross sectional area, the surface integral in Equation 2.29 can be rewritten as

$$\int_{C.S.} \rho \vec{u}_f (\vec{u}_{f,rel} \cdot \hat{n}) dA = -\rho \left(\frac{Q^2}{A_{port}} - \frac{Q_o^2}{A_o} \cos \theta_{jet} \right) \tag{2.30}$$

where Q is volumetric flow rate through the port, Q_o is the volumetric flow rate through the orifice, A_o is the orifice area, and is θ_{jet} is the angle of the fluid exiting the control volume, relative to the x-axis. It is assumed the jet angle is approximately equal to the angle of the disc bevel angle and that

$$\int_{C.V.} \rho \vec{u}_f dV \cong \rho Q(L + x) \tag{2.31}$$

Then, the force on the control volume is expressed as

$$F_{C.V.} = -\rho \left(\frac{Q^2}{A_{port}} - \frac{Q_o^2}{A_o} \cos \theta \right) + \rho \left[Qu + (L + x)\frac{dQ}{dt} \right] \tag{2.32}$$

To prevent dividing by zero as the orifice area goes to zero, note that

$$\frac{Q_o^2}{A_o} = 2C_d^2 A_o \frac{|\Delta P|}{\rho} \tag{2.33}$$

The force on the control volume is then rewritten as

$$F_{C.V.} = -\rho \left(\frac{Q^2}{A_{port}} - 2C_d^2 A_o \frac{|\Delta P|}{\rho} \cos \theta \right) + \rho \left[Qu + (L + x)\frac{dQ}{dt} \right] \tag{2.34}$$

Equation 2.34 may be separated into steady and transient components so that the flow force is calculated as

$$F_{flow} = F_{flow,s} + F_{flow,t} = -F_{C.V.} \tag{2.35}$$

The steady flow force, which represents the change in momentum of the fluid entering and exiting the control volume, is given by

$$F_{flow,s} = \rho \left(\frac{Q^2}{A_{port}} - 2C_d{}^2 A_o \frac{|\Delta P|}{\rho} \cos\theta \right) \tag{2.36}$$

The transient flow force represents the force associated with the change of momentum of the fluid within the control volume as it accelerates and is given by

$$F_{flow,t} = -\rho \left[Qu + (L+x)\frac{dQ}{dt} \right] \tag{2.37}$$

2.3 Disc Valve Flow Rate Model

The flow rate through the check valve was calculated by modeling it as an orifice. For steady flow of an incompressible fluid, the volumetric flow rate through an orifice, Q_o, is related to the pressure differential across the orifice, ΔP, by

$$Q_o = C_d A_0 \sqrt{\frac{2|\Delta P|}{\rho}} \, sign(\Delta P) \tag{2.38}$$

where C_d is the discharge coefficient and A_o is the orifice area. Although Equation 2.38 is derived for steady flow, it is commonly assumed to approximate transient flow rates. In addition to orifice flow, fluid is displaced by disc motion. To develop and expression for the orifice area of the disc valve, consider the flow rate diagram as shown in Figure 2.6.
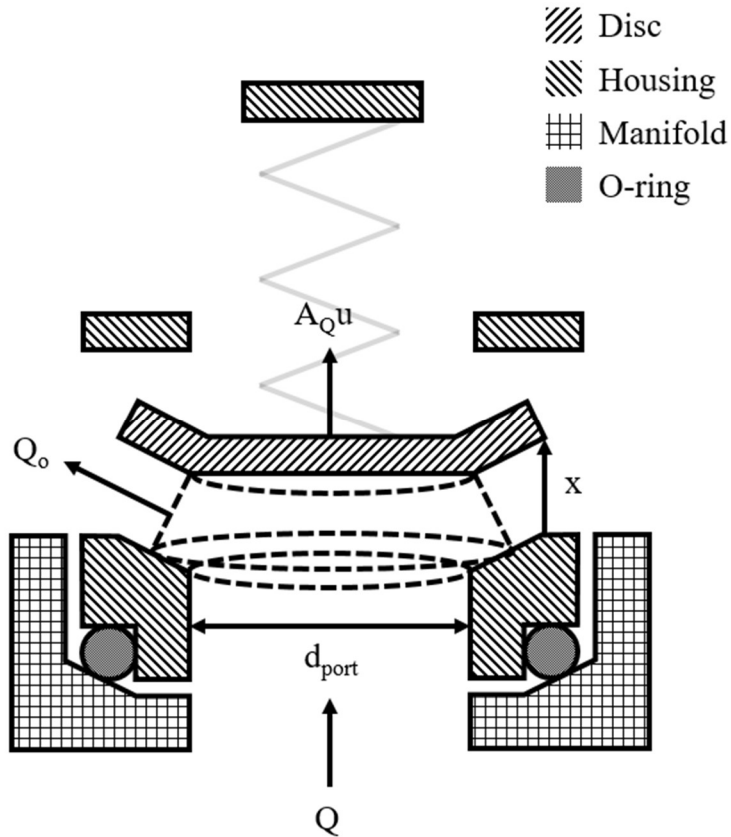
Figure 2.6. Disc valve orifice area and flow rate diagram

The orifice area takes the shape of conical frustum which is given by:

$$A_o = \pi d_{port} \sin \theta \, x - \cos \theta \sin^2 \theta \, x^2 \qquad (2.39)$$

For small values of x such that $x \ll \frac{\pi d_{port}}{\sin \theta \cos \theta}$, the higher order term in Equation 2.39 may be neglected. Noting that for negative values of x when the disc is pressing into the seat the orifice area remains zero, the orifice area becomes

$$A_o = max\left(0, \pi d_{port} \sin \theta \, x\right) \qquad (2.40)$$

Since the discharge coefficient is a function of the Reynolds number and therefore the flow rate, an iterative process is required to calculate the flow rate. The total volumetric flow

rate through the disc valve is the sum of the orifice flow rate through the valve and the rate of fluid displacement caused by the disc displacement:

$$Q = C_d(Re)A_o \sqrt{\frac{2|P_{up} - P_{down}|}{\rho}} \, sign(P_{up} - P_{down}) + A_Q u \tag{2.41}$$

Assuming orifice flow implies that the pressure drops instantaneously across the orifice boundary such that the pressure differential is zero around an outer annulus of the disc. While this seems inconsistent with Equation 2.18, the orifice area is assumed for the purposes of defining the discharge coefficient. Since the orifice flow rate is determined experimentally as a function of $\Delta P_{u\text{-}d}$ and x, the choice of assumed orifice geometry is arbitrary and does not affect the flow rate calculations. Therefore, it is appropriate to assume an orifice geometry for the purposes of calculating the flow rate, while not requiring other aspects of the model such as pressure force to be consistent with the assumed orifice geometry.

2.3.1   Fluid Displacement Area

As the disc moves, it displaces fluid at a rate proportional to the velocity. The constant of proportionality is the fluid displacement area, A_Q. Assuming the value of A_Q has a theoretical lower limit, A_1, and upper limit, A_2, and that A_Q may depend on the direction of valve motion, it can be expressed as

$$A_Q(u) = \begin{cases} A_1 + f_1(A_2 - A_1), & u < 0 \\ A_1 + f_2(A_2 - A_1), & u > 0 \end{cases} \tag{2.42}$$

where f_1 and f_2 are the fluid displacement parameters with values between 0 and 1. The value of A_Q is at a minimum in the case where the valve seat completely obstructs fluid motion due to valve displacement such that $A_1 = A_{port}$. The maximum value of A_Q represents the case where the valve seat does not obstruct fluid motion such that $A_1 = A_{disc}$.

2.4 Determination of Experimental Disc Valve Parameters

In this section, the experimental disc valve, shown in Figure 2.1 and Figure 2.2 will be characterized. A detailed analysis including analytical, computational, and experimental methods of determining its parameters will be performed. The purpose of this section is twofold; first to provide practical methods of determining disc valve model parameters and second to calculate parameters of the disc valve used for experimental validation.

2.4.1 Disc and Spring Mass

The mass of the check valve disc was measured on a digital scale by weighing four discs at once to increase resolution. The resulting average disc mass was 2.5 g. The spring mass was determined by measuring the wire diameter and length to calculate the volume, which was then multiplied by the material density to get a spring mass of 0.6 g. A summary of the mass contributions is given in Table 2.1.

Table 2.1. Mass contribution of disc and spring components

Component	Mass (g)	% of Total
Disc	2.5	93
1/3 Spring	0.2	7
Total	**3.9**	**100**

2.4.2 Pressure Coefficients

Recall from Section 2.2.2.1, the pressure coefficients C_1 and C_2 are a function of R_i, R_o, μ, and θ. For the disc shown in Figure 2.2, $R_i = 5.24$ mm, $R_o = 7.5$ mm, and $\theta = 54°$. Mobil DTE 25 hydraulic oil was used during experimental validation. As shown in Appendix B, at room temperature, the hydraulic oil has a dynamic viscosity of $\mu = 0.0683$ Pa*s. According to Equation 2.14 and 2.15, $C_1 = 0.714$ and $C_2 = 7.630 \times 10^{-11}$ Nm^{2}s.

2.4.3 Spring and Contact Forces

2.4.3.1 Spring Stiffness

An analytical expression for the stiffness of a helical spring is as follows:

$$k_{spr} = \frac{d^4 G}{8 D^3 N_a}$$

<div align="right">(2.43)</div>

where d is the wire diameter, G is the shear modulus, D is the spring diameter, and N_a is the number of active coils or the number of coils that experience deformation. Properties of the disc valve spring, shown in Figure 2.2, are listed in Table 2.2. Inputting the values from Table 2.2 into Equation 2.43, the spring stiffness was calculated to be 220 N/m.

Table 2.2. Disc valve compression spring properties

Parameter	Symbol	Value	Units
Wire diameter	d	0.61	mm
Spring diameter	D	9.9	mm
Shear modulus (music wire)	G	80	GPa
Number of active coils	N_a	6.5	unitless

In addition to the analytical calculation, the spring stiffness was measured experimentally by placing the spring on a scale and measuring the force at several displacements. A least-squares linear fit gave a measured spring stiffness of 213 N/m. A difference of 7.85% between the calculated and measured stiffness values represents good agreement suggesting Equation 2.43 can be used for design and optimization purposes when direct measurements are impractical. In this work, the measured value was used due to the uncertainty in spring geometry and material properties.

2.4.3.2 Seat and Stop Stiffness and Damping Coefficient

The stiffness of simple geometries, such as a helical spring or solid rod, may be calculated with analytical formulae. The seat and stop geometry, however, are significantly more complex, rendering analytical analysis impractical. By contrast, finite element analysis provides a straightforward method to determine the force-displacement relationship. For small displacements, such as those experienced in a disc valve, the force-displacement relationship may be approximated as linear with a proportionality constant of k_{seat} or k_{stop} as in Equation 2.20.

The seat shown in Figure 2.2 was modeled in commercial FEA software with AISI type 304 stainless steel material properties. A force of 600 N was applied to the seat in the negative x-direction, yielding the predicted displacement shown in Figure 2.7. The displacement at four points around the seat midpoint were measured to determine an average displacement of 1.945×10^{-4} mm. Therefore, the seat stiffness is $k_{seat} = \frac{600\ N}{1.985 \times 10^{-7}\ m} = 3.02 \times 10^9\ \frac{N}{m}$. From Equation 2.23, the critical damping coefficient of the seat is $c_{seat} = 2\sqrt{3.02 \times 10^9\ \frac{N}{m} * 3.9 \times 10^{-3}\ kg} = 6860\ \frac{Ns}{m}$.
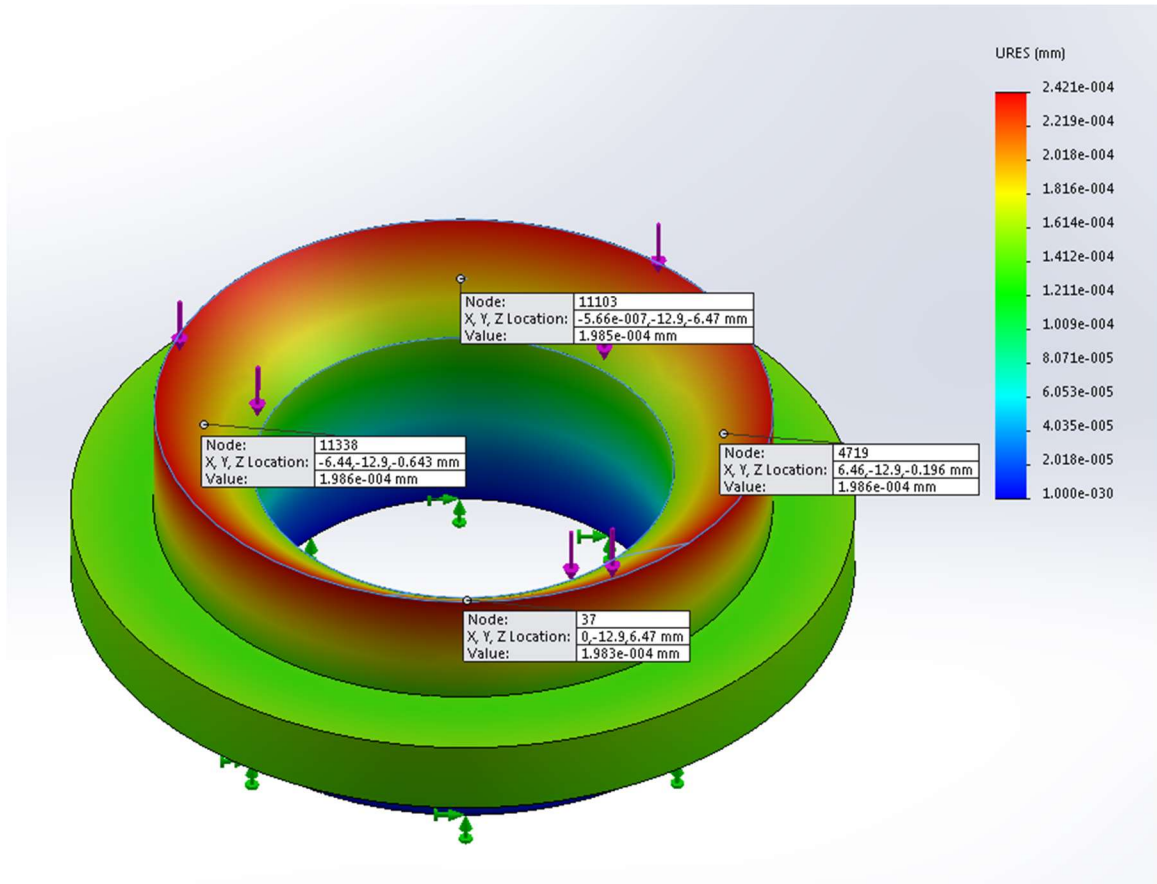
Figure 2.7. FEA computation of seat stiffness

In cases where the housing seat is not fully pressured against the manifold, leaving a gap as shown in Figure 2.1, the effective stiffness is significantly lowered as the rubber O-ring, which has a significantly lower stiffness than the stainless steel seat, is allowed to compress. The effective seat stiffness in this case was calculated by measuring the (negative) pressure differential across the closed valve and deflection of the seat and O-ring during pumping experiments, which will be described in Section 5.4, in order to obtain a force-displacement relationship. Assuming a linear force-displacement relationship of the seat and O-ring, the stiffness was calculated to be 1.5×10^6 N/m. The damping coefficient of the valve seat in this case is $c_{seat} = 2\sqrt{1.5 \times 10^6 \ \frac{N}{m} * 3.9 \times 10^{-3} \ kg} = 153 \ \frac{Ns}{m}$.

The stop stiffness and damping coefficient were determined with same approach as the seat. A model of the housing, shown in Figure 2.2, was created with ABS plastic

material properties. A force of 125 N was applied to the stop as shown in Figure 2.8. The displacement at four points around the stop midpoint were measured to determine an average displacement of 6.53×10^{-2} mm. Therefore, the stop stiffness is $k_{stop} = \frac{125\ N}{6.53 \times 10^{-5}\ m} = 1.91 \times 10^6\ \frac{N}{m}$. From Equation 2.23, the critical damping coefficient of the seat is $c_{stop} = 2\sqrt{1.91 \times 10^6\ \frac{N}{m} * 3.9 \times 10^{-3}\ kg} = 173\ \frac{Ns}{m}$.
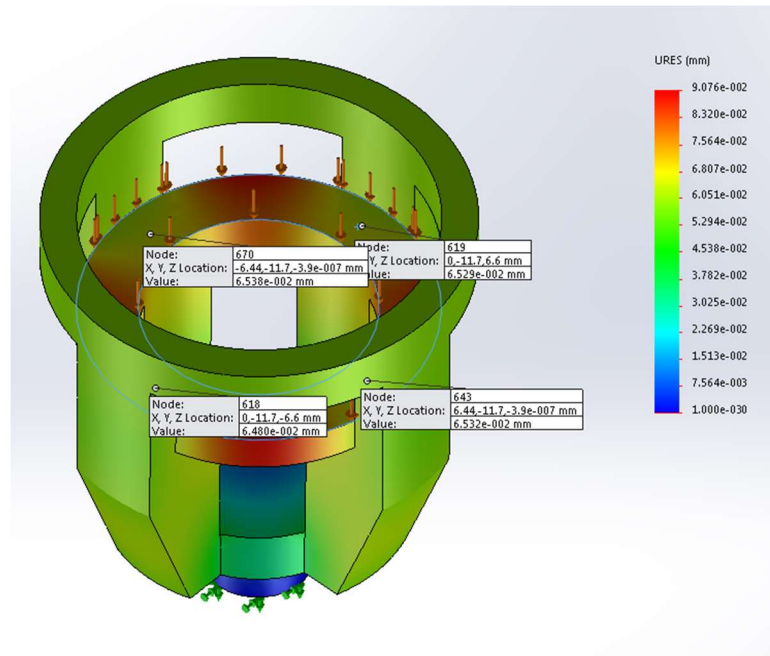
Figure 2.8. FEA computation of stop stiffness

2.4.4 Drag and Viscous Damping Coefficient

The value of c_{visc} and $C_{D,\infty}$ required to calculate the drag force in Equation 2.28 can be determined from a plot of the drag coefficient as a function of Reynolds number. Typical estimate of $C_{D,\infty}$ are approximately 1.17, however, this value is expected to increase in confined areas such as a disc valve housing and manifold. Therefore, in this work, $C_{D,\infty}$ is estimated to be 2. Drag coefficient plots show little difference between a sphere and disc in the viscous, low Re region, so that an appropriate estimate of c_{visc} for a disc is 10. Recall that, according to Stokes' law, c_{visc} for a sphere is approximately 9.42. Although the

39

preceding drag analysis is not rigorous, the drag force is quite small compared to other forces, such as pressure, so it is reasonable for the purpose of this thesis.

2.4.5 Discharge Coefficient

In this work, the discharge coefficient is defined as

$$C_d = \frac{Q_o}{A_o\sqrt{\frac{2\Delta P}{\rho}}} = \frac{\dot{m}}{A_o\sqrt{2\rho\Delta P}} \tag{2.44}$$

To experimentally determine the discharge coefficient of the check valve, a hydraulic power unit was placed in series with a needle valve, which allows the flow rate through the check valve to be prescribed. Two pressure transducers measured the pressure differential across the check valve while a gear flow meter measured the flow rate through it. The check valve disc displacement was set with a shim that controlled the maximum disc opening, allowing calculation of the orifice area. Figure 2.9 shows a schematic of the experimental setup.
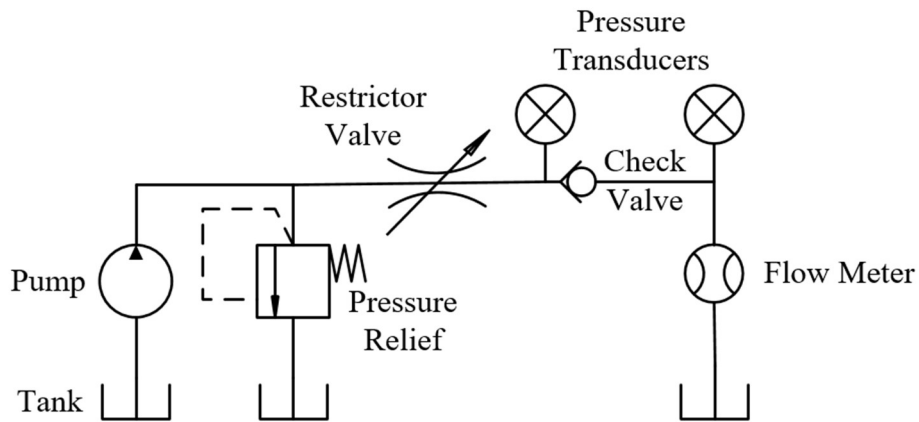
Figure 2.9. Discharge coefficient experimental setup

It is well known that for high Reynolds number flow, the discharge coefficient approaches a constant value – approximately 0.6 for a sharp edged orifice. For low

Reynolds number flow, the discharge coefficient exhibits a Reynolds number dependence. For a non-circular orifice such as that of a check valve, the Reynolds number may be defined by the hydraulic diameter, D_H:

$$Re = \frac{\rho V D_H}{\mu} \qquad (2.45)$$

Noting that $D_H = 4A_o/p$ where p is the orifice perimeter and $V = Q_o/A_o$, the Reynolds number is related to the orifice flow rate by

$$Re = \left(\frac{4\rho}{\mu p}\right) Q_o \qquad (2.46)$$

For a disc valve orifice, such as that in Figure 2.6, the perimeter is approximately twice the circumference of the valve port. Therefore, the Reynolds number is proportional to the orifice flow rate by a constant. Wu et al. (2002) proposed an empirical discharge coefficient model of the form

$$C_d = C_{d\infty} + Ae^{-B\sqrt{Re}} - (C_{d\infty} + A)e^{-C\sqrt{Re}} \qquad (2.47)$$

A nonlinear least squares fit was then applied to experimental measurements to obtain the following correlation

$$C_d = 0.9720 - 1.0801e^{-0.1058\sqrt{Re}} + 0.1080e^{-0.9505\sqrt{Re}} \qquad (2.48)$$

The experimental results and empirical correlation given by Equation 2.48 are shown in Figure 2.10, where x in the legend is the valve displacement. The results show that the discharge coefficient is a strong function of the Reynolds number. However, there is no clear dependence on valve opening. Note that Equation 2.48 is only valid across the range of Reynolds numbers used to obtain the correlation. As such, the value 0.9720 should

not be interpreted as an accurate estimate of the asymptotic value of the discharge coefficient for large Reynolds numbers.
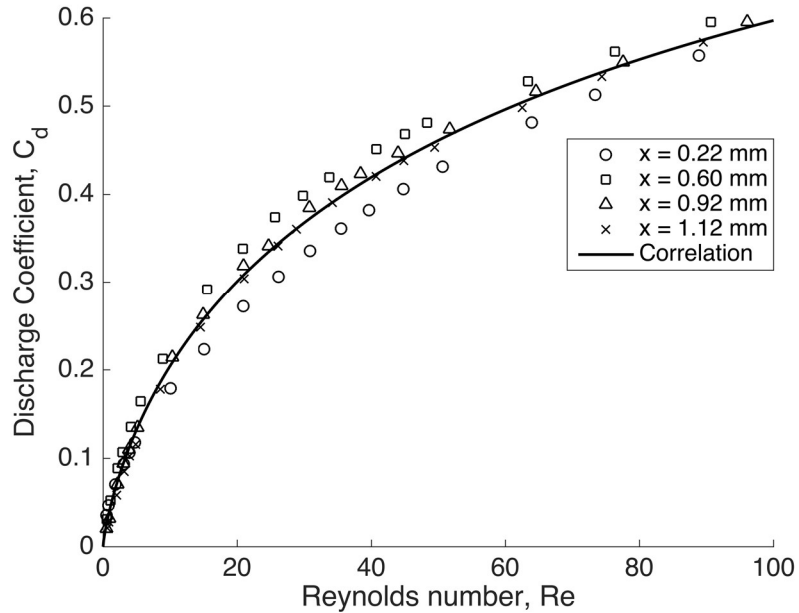
Figure 2.10. Disc valve discharge coefficient correlation

2.4.6   Fluid Displacement Area

The fluid displacement area depends on the flow field around the valve. The model developed in this work is not designed to capture the flow field and thus A_Q must be determined experimentally or estimated analytically. The disc valve studied in this work has a beveled seat so it is reasonable to expect the disc to displace fluid relatively easily compared to a flat seat that may obstruct flow or induce recirculation. Therefore, it was estimated that for the disc valve, $f_1 = f_2 = 1$ such that $A_Q = A_2 = A_{disc}$.

2.5   Summary

A summary of the calculated disc check valve parameters computed in this chapter is given in

Table 2.3.

Table 2.3. Disc valve experimental parameters.

Parameter	Symbol	Value	Units
Theoretical minimum value of A_Q	A_1	86.3	mm^2
Theoretical maximum value of A_Q	A_2	177	mm^2
Disc face area	A_{disc}	177	mm^2
Fluid displacement area	A_Q	177	mm^2
Valve seat damping coefficient – inlet	c_{seat}	6860	N*s/m
Valve seat damping coefficient – delivery	c_{seat}	153	N*s/m
Valve stop damping coefficient	c_{stop}	173	N*s/m
Poiseuille flow pressure coefficient	C_1	0.714	dimensionless
Stiction coefficient	C_2	7.630×10^{-11}	N*m^{2}s
Valve port diameter	d_{port}	10.48	mm
Disc face diameter	d_{disc}	15.00	mm
First fluid displacement area parameter	f_1	1	dimensionless
Second fluid displacement area parameter	f_2	1	dimensionless
Valve spring stiffness	k	213	N/m
Valve seat spring stiffness – inlet	k_{seat}	3.02×10^9	N/m
Valve seat spring stiffness – delivery	k_{seat}	1.5×10^6	N/m
Valve stop spring stiffness	k_{stop}	1.91×10^6	N/m
Port length	L	5.2	mm
Disc mass	m	2.5	g
Spring mass	m_s	0.6	g
Disc inner radius	R_i	5.24	mm
Disc outer radius	R_o	7.50	mm
Hydraulic oil temperature	T	21	°C
Valve spring preload	x_{pre}	6.2	mm
Maximum valve opening – inlet	x_{stop}	1.19	mm
Maximum valve opening – delivery	x_{stop}	1.01	mm
Poiseuille-orifice flow transition parameter	ϵ_0	0.1	dimensionless
Hydraulic oil dynamic viscosity	μ	0.0683	Pa*s
Disc bevel angle	θ	54	degrees

2.6   Conclusion

In this chapter, the development of a general disc style check valve model was presented. The techniques were then applied to a specific valve architecture for the purpose of experimental validation that will be described in Chapter 5. As with previous literature, many forces were considered including pressure, spring reaction, stiction, viscous damping and inertial drag, seat and stop elastic and dissipative reaction forces, steady and transient flow forces. Elastic seat and stop reaction forces were estimated from a 3-D static FEA load analysis. For the disc valve model used in this thesis, stiction and flow forces were neglected.

Two flow regimes were identified; Poiseuille and orifice. Flow rate was modeled as quasi-steady orifice flow with an empirical discharge coefficient. The rate of fluid displacement due to valve motion was estimated from disc geometry. The pressure field was computed in the Poiseuille flow regime from the Reynolds equation yielding two terms; a stiction due to valve motion and a Poiseuille flow term from pressure driven flow.

Chapter 3 Reed Valve Modeling

Reed valves are a type of check valve commonly found in a wide range of applications, including air compressors and internal combustion engines. Because the spring and mass components of a reed valve are contained in a single element, it is light and compact compared to traditional disc, poppet, or ball style check valves. These advantages make reed valves promising for use in high frequency hydraulic applications such as piston pumps, switch-mode hydraulics, and digital hydraulics.

In this chapter, a prototype reed valve design, which was constructed as a proof of concept, is presented. A general modeling approach is then developing with linear beam theory as the basis for modeling the dynamic behavior of the reed. Next, a fluid flow rate model is discussed, based on the orifice equation. The remainder of the chapter presents a detailed description of the model parameters including physical interpretations and methods of calculating terms with the prototype reed as the archetypal example. An emphasis is placed on computationally inexpensive methods to make the model practical for use in optimization routines.

3.1   Reed Valve Design

3.1.1   Prototype Reed Valve

Before modeling, a prototype hydraulic reed valve was designed and built to test the concept and guide model development. The reed valve assembly, shown in Figure 3.1, is comprised of three parts – the reed itself, a stop to limit the maximum opening, and a seat to provide the reed with support during negative pressure differentials.
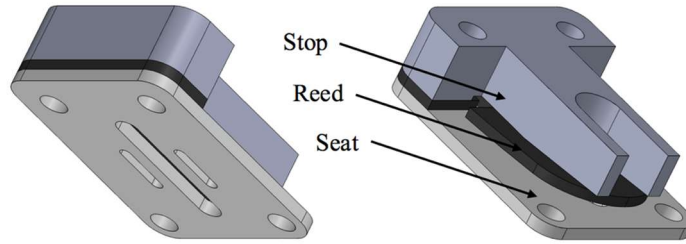
Figure 3.1. Prototype reed valve assembly

The design of the seat slots is an important consideration. Larger slots allow for a larger flow area, while smaller slots allow for greater support of the reed, thus lowering its stress. Similarly, for the stop, a larger maximum opening allows for a smaller pressure drop across the reed, while a smaller maximum opening helps prevent plastic deformation of the reed and allows it to close faster, resulting in less backflow. An iterative process was used to design the seat. First, a seat was designed to provide sufficient support for the reed at the highest negative pressure differential expected. Next, the maximum pressure drop across the seat was estimated. After several iterations, the design shown in Figure 3.2 was found to provide a good compromise between design parameters.
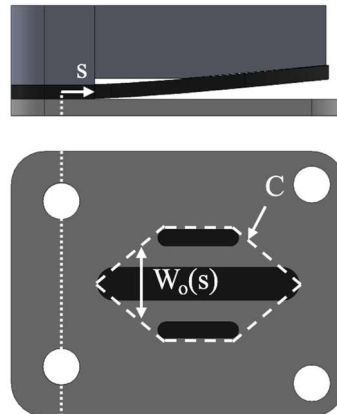
Figure 3.2. Prototype reed valve assembly shown in the fully open position. The dashed line C represents the perimeter of the assumed orifice area. W_o is the width of the orifice area. The reed is clamped at the dotted line ($s = 0$)

Shallow grooves were cut into the upstream side of the prototype reed as shown in Figure 3.3. The purpose of these grooves is twofold. First, by reducing the contact area between the reed and the seat, stiction is reduced. Second, the area of the reed that is directly exposed to upstream pressure while the valve is closed is increased. Both stiction and a reduced reed area exposed to the upstream pressure delay valve opening in response to a positive pressure differential.
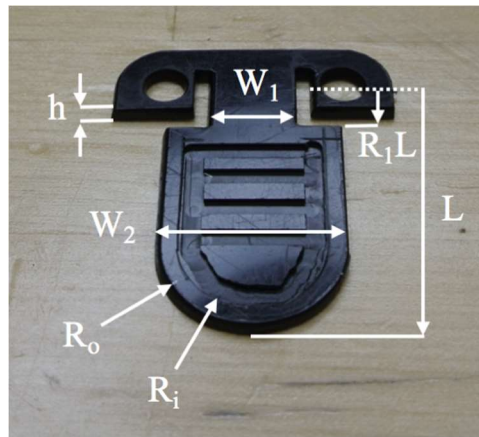
Figure 3.3. Prototype reed geometry including thickness, h, width of the first section, W_1, width of the second section, W_2, length, L, step location parameter, R_1, inner radius, R_i, and outer radius, R_o

To ensure the prototype reed would not experience any plastic deformation, a 3-D finite element analysis was performed using commercial software. At the maximum opening, the maximum von Mises stress in the reed is 26.2 MPa compared to a yield stress of 63.0 MPa for Delrin. The prototype reed shown in Figure 3.3 will be used to generate empirical correlations that will be discussed in Sections 3.8.5 and 3.8.6.

3.1.2   Summary of Reed Geometries

During development of the reed model, four different reed geometries, shown in Figure 3.4 and Figure 3.5, were studied. The different geometries were chosen to evaluate the model for reeds with specific geometric features including a step change in width, a

rounded tip, and shallow grooves. The properties of the four reed geometries are summarized in Table 3.1.
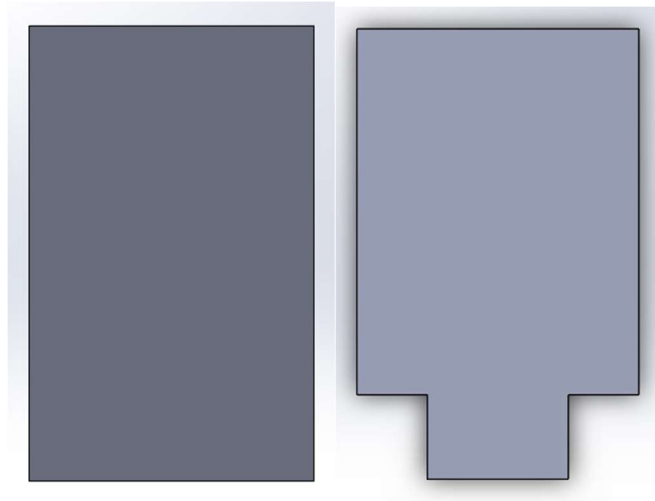
Figure 3.4. Uniform reed (left) and stepped reed #1 (right)
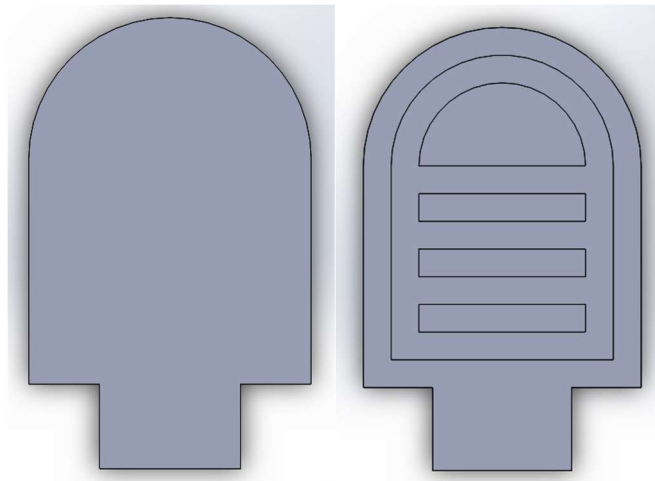
Figure 3.5. Stepped reed #2 (left) and prototype reed (right)

Table 3.1. Reed parameters (Delrin 2700 NC010)

Parameter	Symbol	Value	Units
Reed material elastic modulus	E	2.9	GPa
Nominal thickness	h	1.35	mm
Groove depth	h_g	0.508	mm
Length from clamped end	L	25.4	mm
Step location parameter	R_1	0.1875	dimensionless
Tip outer radius	R_o	0 or 7.94	mm
Tip inner radius	R_i	6.35	mm
Width of first section	W_1	7.94 or 15.9	mm
Width of the second section	W_2	15.9	mm
Width ratio	W_{21}	1 or 2	dimensionless
Groove width	W_g	1.588	mm
Reed (cantilever) material density	ρ_c	1410	kg/m^3

3.2   Beam Theory

There are several methods of modeling beam motion that represent a range of assumptions, complexity, and accuracy including analytical and finite element methods. While finite elements methods can be used to model beams of complex shapes, this thesis focuses on analytical methods for the sake of computation time. In modeling a reed valve, exact solutions are not as important as the overall dynamical behavior. As such, the simplest approach that predicts reed behavior with sufficient accuracy is desired. Furthermore, only the first mode of vibration was considered, rendering accuracy of higher order vibration modes inconsequential.

Analytical models of traversal vibrating beams include Timoshenko, shear, Rayleigh, and Euler-Bernoulli beam theory. Assumptions common each of these are (Han et al. 1999):

1.   Axial length is much larger than the width or thickness

2. The material is linearly elastic (Hookean)

3. Poisson effect is neglected

4. The cross-sectional area is symmetric such that the centroid and neutral axis coincide

5. Planes perpendicular to the neutral axis remain perpendicular during deformation

6. Angle of rotation is small (small angle approximation)

Euler-Bernoulli beam theory further simplifies the problem by neglecting both rotational inertia and shear deformation. Shear theory includes the shear term while neglecting rotary inertia whereas Rayleigh theory neglects shear deformation while accounting for rotary inertia. In this work, Euler-Bernoulli beam theory was chosen as the basis for a reed valve model.

3.2.1   Comparison of Beam Theories

Perhaps the simplest way to evaluate the performance of a dynamic beam model is by comparing the predicted natural frequency to the actual value. A reed valve in a hydraulic system is subjected to a large pressure force and is heavily damped by the surrounding fluid, making it far from the case of free vibration. Nonetheless, the equation of motion sought to model a reed valve should be able to capture the dynamics of a reed in free vibration and therefore natural frequency is a useful performance metric.

Traill-Nash and Collar measured the natural frequency of eight beams between 162 and 216 Hz and compared to values calculated from Euler-Bernoulli, shear, and Timoshenko beam theory. Their results are summarized with the average error in Table 3.2.

Table 3.2. Average percent deviation in natural frequency from experimental values
(Traill-Nash & Collar 1953)

Beam Theory	First Natural Frequency	Second Natural Frequency
Euler-Bernoulli	+21%	+112%
Shear	+2%	+3%
Timoshenko	+1%	+1%

Several important conclusions can be drawn from the results of Traill-Nash and Collar's study. First, the exclusion of shear flexibility in Euler-Bernoulli beam theory causes the shear stiffness to be over-predicted thus over-predicting the natural frequency. Second, this effect is greater in higher mode vibrations. Third, while accounting for shear forces significantly increases the accuracy of natural frequency calculations, the inclusion of rotary inertia only adds an incremental improvement in accuracy. Since a reed valve is expected to bend only at the first mode, the decreasing accuracy at higher modes isn't a concern. The question of whether or not Euler-Bernoulli beam theory is accurate enough for modeling reed valves must now be answered.

3.2.2 Euler-Bernoulli Beam Natural Frequency Analysis

To evaluate the accuracy of Euler-Bernoulli beam theory in the context of a reed valve, a geometry similar to what is expected in a reed valve, namely a slender reed with a step change in width, was examined. Theory on the natural frequency of a uniform reed is first discussed, then it is extended to a reed with a step change in width. The purpose of this section is to determine whether Euler-Bernoulli beam theory adequately captures the reed valve dynamics by evaluating its ability to predict natural frequency.

3.2.2.1 Uniform Width

The circular natural frequency of a uniform Euler-Bernoulli beam is given by

$$\omega_n = \alpha^2 \sqrt{\frac{EI}{mL^4}} \qquad (3.1)$$

where ω_n is the circular natural frequency, α is the natural frequency parameter, E is elastic modulus, I is the area moment of inertia, m is mass per length, and L is length. The natural frequency parameters are solutions to the equation

$$\cosh \alpha \cos \alpha + 1 = 0 \qquad (3.2)$$

The solution for the fundamental or first natural frequency parameter is $\alpha \approx 1.875$. For a rectangular cross section, the area moment of inertia is given by

$$I = \frac{Wh^3}{12} \qquad (3.3)$$

where W is the beam width and h is the thickness. Therefore, the natural frequency can be calculated as

$$\omega_n = \alpha^2 \frac{h}{L^2} \sqrt{\frac{E}{12\rho}} \qquad (3.4)$$

According to Equation 3.4, the natural frequency of the uniform reed defined in Table 3.1 is 3046 rad/s. It is worth noting that for a beam of uniform width, the natural frequency is independent of width.

3.2.2.2 Step Change in Width

The natural frequency of a beam with a step change in cross section can also be calculated using Euler-Bernoulli beam theory as follows (Naguleswaran 2002):

$$\omega = \alpha_1{}^2 \sqrt{\frac{EI_1}{m_1 L^4}} = \alpha_2{}^2 \sqrt{\frac{EI_2}{m_2 L^4}} \qquad (3.5)$$

where the subscripts on α, I and m indicate the first or second section of the beam. For a beam with a rectangular cross section, a uniform thickness, and a step change in width, the following can be derived from Equation 3.3:

$$\frac{I_1}{m_1} = \frac{I_2}{m_2} = \frac{h^2}{12\rho} \qquad (3.6)$$

therefore, the circular natural frequency of a beam with a step change in width is

$$\omega = \alpha^2 \frac{h}{L^2} \sqrt{\frac{E}{12\rho}} \qquad (3.7)$$

Note that this is the same equation as that of a uniform reed, however, the natural frequency parameter will have a different value. Details on calculating the natural frequency parameter and tabulated values can be found in the literature (Naguleswaran 2002). It turns out that the natural frequency parameter is a function of step location parameter and the width ratio.

To evaluate the accuracy of Euler-Bernoulli beam theory for a beam of similar geometry to the prototype reed, consider stepped reed #1. According to the method developed by Naguleswaran, the natural frequency parameter of stepped reed #1 is 1.674 and from Equation 3.7, the natural frequency is 2427 rad/s.

3.2.3   Finite Element Method Frequency Analysis

Having calculated the natural frequency of the uniform reed and stepped reed #1 according to Euler-Bernoulli beam theory, the actual natural frequency must be determined. Two possible methods of determining the actual natural frequency are

experiments and finite element analysis (FEA). In this work, the latter was used for its turnaround time and to avoid experimental uncertainty.

The Finite Element Method (FEM) is capable of calculating the natural frequency of complex shapes with high accuracy and can therefore be used to evaluate the accuracy of Euler-Bernoulli beam theory for a specific type of geometry. Each of the four reed geometries shown in Figure 3.4 and Figure 3.5 and defined in Table 3.1 were modeled and meshed in commercial CAD software capable of FEM frequency analysis. As an example the stepped reed #1 mesh is shown in Figure 3.6.
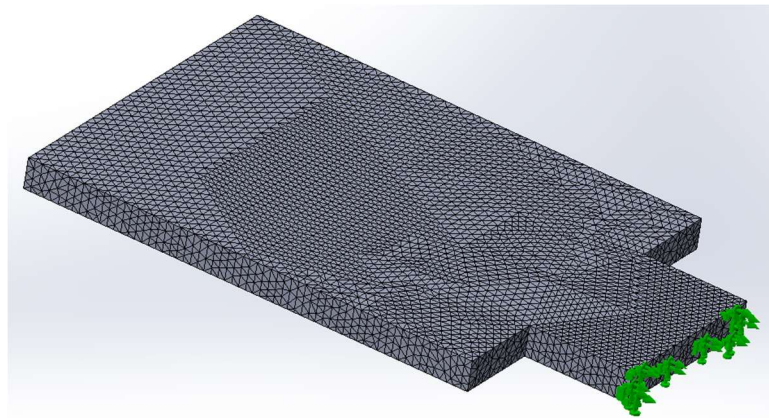
Figure 3.6. Meshed reed for comparison of Euler-Bernoulli and FEM beam natural frequency.

A convergence study was performed to ensure the solution was independent of mesh size. With a refined mesh, frequency analysis yielded the results summarized in Table 3.3.

Table 3.3. Natural frequency comparison between Euler-Bernoulli beam theory and FEA

Case	ωn (E-B)	ωn (FEA)	% Error
Uniform Reed	3046 rad/s	3123 rad/s	–2.466
Stepped Reed #1	2427 rad/s	2383 rad/s	+1.550
Stepped Reed #2	N/A	2673 rad/s	N/A
Prototype Reed	N/A	2523 rad/s	N/A

Percent deviation in natural frequency calculated with Euler-Bernoulli beam theory from the FEM value for stepped reed #1 is +1.550%. The presence of a rounded tip and shallow grooves are not expected to further violate assumptions enough to cause reeds of geometry similar to the prototype reed to be poorly modeled by Euler-Bernoulli beam theory, considering stepped reed #1 is modeled quite well by it. Therefore, it is reasonable to conclude that Euler-Bernoulli beam theory provides a sufficiently accurate analytical approach to modeling the reed valve dynamics.

3.3   Reed Equation of Motion

The equation of motion of a dynamic Euler-Bernoulli beam can be obtained from Hamilton's variation principle considering the kinetic and potential energy of the beam as well as the non-conservative work done on the beam (Han et al. 1999). If internal damping of the beam is accounted for, the dynamic Euler-Bernoulli beam equation of motion is (Tarnopolsky et al. 2000)

$$m_c(s)\frac{\partial^2 v(s,t)}{\partial t^2} + R(s)\frac{\partial v(s,t)}{\partial t} + \frac{\partial}{\partial s^2}\left[EI(s)\frac{\partial^2 v(s,t)}{\partial s^2}\right] = q(s) \tag{3.8}$$

where the subscript c refers to the cantilever or reed, v is the reed displacement, s is the coordinate along the length of the reed, R is the viscous damping coefficient per unit length, and q is the forcing function per unit length. For a reed valve operating in hydraulic oil, damping is provided both by internal damping of the reed as it dissipates energy during deformation and fluid damping as the reed does work on the fluid. Therefore, R includes an internal damping component, R_c and viscous fluid damping component, R_f, such that $R = R_c + R_f$. The first term on the left hand side of Equation 3.8 represents kinetic energy per unit length along the length of the beam. The second term represents the energy dissipation due to material deformation. The third term represents potential energy associated with the beam bending.

A reed in a fluid experiences an added mass and aerodynamic drag effect that, when accounted for, result in a modification of Equation 3.8 as follows:

$$\left[m_c(s) + m_f(s)\right]\frac{\partial^2 v}{\partial t^2} + R(s)\frac{\partial v}{\partial t} + \frac{1}{2}\rho\left(\frac{\partial v}{\partial t}\right)^2 C_D W(s) \tag{3.9}$$

$$+ \frac{\partial}{\partial s^2}\left[EI(s)\frac{\partial^2 v}{\partial s^2}\right] = q(s)$$

where the subscript f refers to the fluid, ρ is the fluid density, and C_D is the drag coefficient. Equation 3.9 is a partial differential equation describing the reed motion along the entire length of the reed. A much simpler equation of motion would be an ordinary differential equation (ODE) describing the motion of a single point on the reed. Then, quantities of interest could be related to the motion of a single point, reducing the problem to a one-dimensional ODE. Such an approach requires knowledge of the shape of the deflected reed. To simplify the analysis, the reed deflection at each point may be normalized by the maximum deflection, which occurs at the tip. If it is assumed that the normalized deflection depends only on the location along the reed, then a mode function, ψ, may be defined by

$$v(s, t) = [x(t) - x_0]\psi(s) \tag{3.10}$$

where x is the tip deflection and x_0 is the initial tip deflection. The mode function is useful because it allows the time and space varying deflection to be separating into the product of the time varying tip deflection and a spatially varying coefficient between zero and one.

Next, the added fluid mass per unit length must be determined. To begin, consider a vibrating beam where $L/W \gg 1$ with a uniform, rectangular cross section. The natural frequency of such a reed vibrating in fluid, ω_f, is given by (Van Eysden & Sader 2006):

$$\omega_f = \omega_{vac}\left(1 + \frac{\pi\rho W}{4\rho_c h}\Gamma_f(\kappa_n)\right)^{-1/2} \tag{3.11}$$

where ω_{vac} is the natural frequency in the absence of a surrounding fluid, Γ_f is hydrodynamic function for flexural vibration, and κ_n is the normalized mode number for the nth mode of vibration defined as

$$\kappa_n = \alpha_n \frac{W}{L} \tag{3.12}$$

The exact analytical solution of the hydrodynamic function is unwieldy. A simple and accurate approximation is the Padé approximant representation, given for the flexural mode of vibration as

$$\Gamma_f(\kappa_n) = \frac{1 + 0.74273\kappa_n + 0.14862\kappa_n{}^2}{1 + 0.74273\kappa_n + 0.35004\kappa_n{}^2 + 0.058364\kappa_n{}^3} \tag{3.13}$$

Figure 3.7 shows the Padé approximant representation of the hydrodynamic function for the flexural mode of vibration as a function of the normalized mode number. For infinitely long beams, W/L approaches 0 and Γ_f approaches 1. Conversely, for short beams where W/L approaches infinity, Γ_f approaches 0.
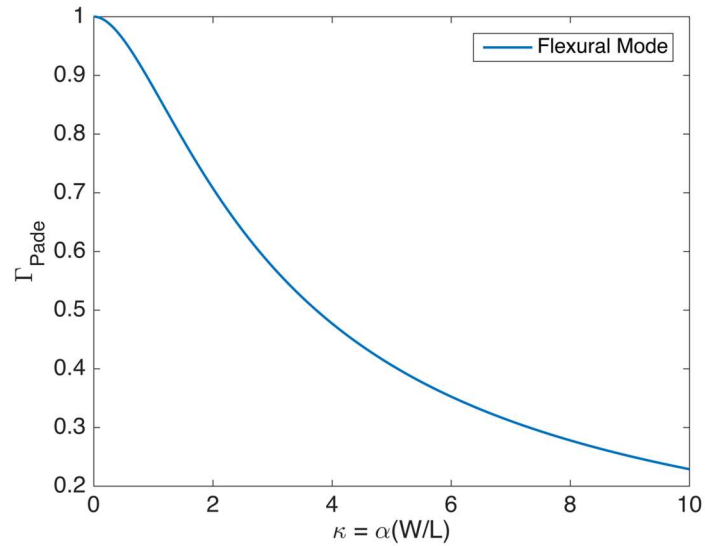
For a reed of non-uniform width, the aspect ratio, L/W, is not defined. If, as an approximation, the area averaged width is used, the normalized mode number can be expressed as

$$\kappa_n = \alpha_n \frac{A}{L^2} \tag{3.14}$$

where A is the area of the reed face. Noting that $k \sim m\omega_n{}^2$ where k is spring stiffness per unit length and assuming the fluid has a spring stiffness of zero, Equation 3.11 can be rewritten as

$$\left(\frac{k_c}{m_c + m_f}\right)^{1/2} = \left(\frac{k_c}{m_c}\right)^{1/2}\left(1 + \frac{\pi\rho W}{4\rho_c h}\Gamma_f\right)^{-1/2} \tag{3.15}$$

Solving for the ratio of added fluid mass per unit length to cantilever mass per unit length yields

$$\frac{m_f}{m_c} = \frac{\pi\rho W}{4\rho_c h}\Gamma_f \tag{3.16}$$

Since $m_c = \rho_c W h$, the added fluid mass is given by

$$m_f = \frac{\pi}{4}\rho W^2 \Gamma_f \tag{3.17}$$

One interpretation of Equation 3.17 is that, the added fluid mass per unit length takes the shape of a circle around the vibrating reed with a diameter equal to the reed width. Equation 3.9, Equation 3.10 and Equation 3.17 are combined to yield the following equation of motion:

$$\psi \left(\rho_c hW + \rho \frac{\pi}{4} W^2 \Gamma_f \right) \ddot{x} + \psi R \dot{x} + \psi^2 \frac{1}{2} \rho \dot{x}^2 C_D W \tag{3.18}$$

$$+ (x - x_0) \frac{d}{ds^2} \left[EI(s) \frac{d^2 \psi(s)}{ds^2} \right] = q$$

where Newton's notation is used to indicate ordinary differentiation with respect to time. Multiplying Equation 3.18 by $\psi(s)$ and integrating from $s = 0$ to $s = L$ yields

$$\ddot{x} \int_0^L \psi^2 \left(\rho_c hW + \rho \frac{\pi}{4} W^2 \Gamma_f \right) ds + \dot{x} \int_0^L \psi^2 R \, ds \tag{3.19}$$

$$+ \frac{1}{2} \rho \dot{x}^2 C_D \int_0^L \psi^3 W ds$$

$$+ (x - x_0) \int_0^L \psi \frac{d}{ds^2} \left[EI \frac{d^2 \psi}{ds^2} \right] ds = \int_0^L \psi q ds$$

Allowing for reeds of non-uniform thickness, the effective thickness is defined as

$$h_{eff} = \frac{\int_0^L \psi^2 hW ds}{\int_0^L \psi^2 W ds} \tag{3.20}$$

Next, Equation 3.19 and 3.20 are combined and divided by $\int_0^L \psi^2 W ds$. The quantities involving an integrals are then defined according to Table 3.4.

Table 3.4. Definition of reed parameters involving integration of the mode function

Parameter	Symbol	Definition	Units
First mode function parameter	γ_1	$\dfrac{\int_0^L \psi W\,ds}{\int_0^L \psi^2 W\,ds}$	dimensionless
Second mode function parameter	γ_2	$\dfrac{\int_0^L \psi^3 W\,ds}{\int_0^L \psi^2 W\,ds}$	dimensionless
Third mode function parameters	γ_3	$\dfrac{1}{W_2}\dfrac{\int_0^L \psi^2 W^2\,ds}{\int_0^L \psi^2 W\,ds}$	dimensionless
Viscous damping coefficient	c	$\dfrac{\int_0^L \psi^2 R\,ds}{\int_0^L \psi W\,ds}$	Pa*s/m
Reed stiffness	κ	$\dfrac{\int_0^L \psi \dfrac{d^2}{ds^2}\left[EI\dfrac{d^2\psi(s)}{ds^2}\right]ds}{\int_0^L \psi W\,ds}$	Pa/m
Pressure load multiplier	X	$\dfrac{1}{\Delta P_{u-d}}\dfrac{\int_0^L \psi q\,ds}{\int_0^L \psi W\,ds}$	dimensionless

The choice of length scale used to non-dimensionalize γ_3 is arbitrary. By choosing W_2, the value of γ_3 ranges between 0 and 1, if W_2 is the largest width. It is assumed that X is a function of reed opening only. The equation of motion can then be written in terms of the parameters defined in Table 3.4 as

$$\left(\rho_c h_{eff} + \gamma_3 \rho W_2 \frac{\pi}{4}\Gamma_f\right)\ddot{x} + \gamma_1 c\dot{x} + \gamma_2 \frac{1}{2}\rho\dot{x}^2 C_D + \gamma_1\kappa(x - x_0) \tag{3.21}$$

$$= \gamma_1 \Delta P_{u-d} X(x)$$

Approximating R and c as constant along the length of the reed, it can be shown that c includes an internal damping component, c_c, and viscous fluid damping component, c_f, such that $c = c_c + c_f$.

The added fluid mass component in Equation 3.21, $\gamma_3 \rho W_2 \frac{\pi}{4}\Gamma_f$, was included to illustrate one possible approach. However, for reed valves, it should be acknowledged that

the fluid dynamics deviate significantly from the assumptions used to calculate the added mass contribution. Specifically, potential flow theory was applied to a reed vibrating in a stationary fluid to derive Equation 3.11. However, added fluid mass was found to have a relatively small effect on reed valve behavior and was therefore neglected in subsequent reed valve analysis.

3.4 Flow Rate Model

Flow through the reed valve is calculated as the sum of orifice flow between the reed and seat and the rate of fluid displaced by the reed motion. Orifice flow is modeled as quasi-steady, utilizing the orifice equation:

$$Q_o = C_d(Q_o)A_o(x)\sqrt{\frac{2|\Delta P_{u-d}|}{\rho}}\, sign(\Delta P_{u-d}) \tag{3.22}$$

where C_d is the discharge coefficient, Q_o is the orifice flow rate through the valve, A_o is the orifice area, and ΔP_{u-d} is the pressure drop across the valve. In addition to orifice flow, as the reed deflects, it displaces fluid at a rate proportional to reed velocity so that the total flow rate through the valve is expressed as

$$Q = C_d(Q_o)A_o(x)\sqrt{\frac{2|\Delta P_{u-d}|}{\rho}}\, sign(\Delta P_{u-d}) \\ +A_Q\dot{x} \tag{3.23}$$

where A_Q is the fluid displacement area.

The reed valve orifice area is calculated by considering the smallest flow path between the seat and reed. The perimeter of this area is assumed to be the dashed curve C, shown in Figure 3.2. This curve is then projected onto the reed to create a corresponding closed curve. The area enclosed by these two curves is the orifice area, which is calculated by integrating the reed deflection around the curve C:

$$A_o = \int_C v(s)ds = x \int_C \psi(s)ds \tag{3.24}$$

The integral quantity in Equation 3.24 is the orifice area per unit tip opening. This quantity is denoted as l_o so that

$$A_o(x) = l_o x \tag{3.25}$$

3.4.1 Fluid Displacement Area

Recall Equation 2.42, which defined the fluid displacement area as

$$A_Q(u) = \begin{cases} A_1 + f_1(A_2 - A_1), & u < 0 \\ A_1 + f_2(A_2 - A_1), & u > 0 \end{cases} \tag{3.26}$$

To determine A_1, consider the case where the seat completely obstructs fluid displacement, such that only fluid within the orifice boundary shown in Figure 3.2 is displaced by valve motion. In this case, the rate of fluid displacement is found by integrating over the reed within the orifice area boundary as follows:

$$Q_u = \frac{d}{dt} \int_0^L W_o(s)v(s)ds = \left[\int_0^L W_o(s)\psi(s)ds \right] \dot{x} \tag{3.27}$$

Therefore

$$A_1 = \int_0^L W_o(s)\psi(s)ds \tag{3.28}$$

Similarly, to determine A_2, consider the case where the seat does nothing to obstruct fluid displacement. In this case, the entire reed area contributes to fluid displacement during valve motion. The fluid displacement area is then

$$A_2 = \int_0^L W(s)\psi(s)ds \qquad (3.29)$$

3.5 Analytical Reed Stiffness Model

Typically, spring or cantilever stiffness is defined as the force per unit displacement. For a two-dimensional system such as a cantilever, the concept of stiffness becomes more ambiguous as the deflection is different at each location along the cantilever length. Further, the deflection depends not only on the magnitude of force applied but how it is distributed. To obtain a precise definition of the reed stiffness, consider a static reed subjected to a uniform pressure differential with $x_0 = 0$. From the definition of the pressure load multiplier given in Table 3.4, for a uniform pressure distribution, since $q = \Delta PW = constant$, the pressure load multiplier is unity. Solving the resultant equation of motion for κ yields

$$\kappa = \frac{\Delta P}{x} \qquad (3.30)$$

From Equation 3.30, it is clear that κ is the pressure differential per unit tip displacement and is hence referred to as the reed stiffness.

There are now two unique ways of calculating the reed stiffness – one given in Table 3.4 and the other by Equation 3.30. The former requires the ability to calculate smooth, higher order derivatives of the mode function, which is difficult to do without an analytical expression, which may not be known. The latter, however, may be determined experimentally, numerically, or analytically by applying a pressure load and measuring the tip deflection.

In this section, an analytical approach to determining reed stiffness will be developed and validating with finite element analysis. The reed geometry that was modeled is one with a rectangular cross section and uniform thickness. A step change in width and a rounded tip were allowed. Figure 3.8 shows a top view of the resulting reed geometry.
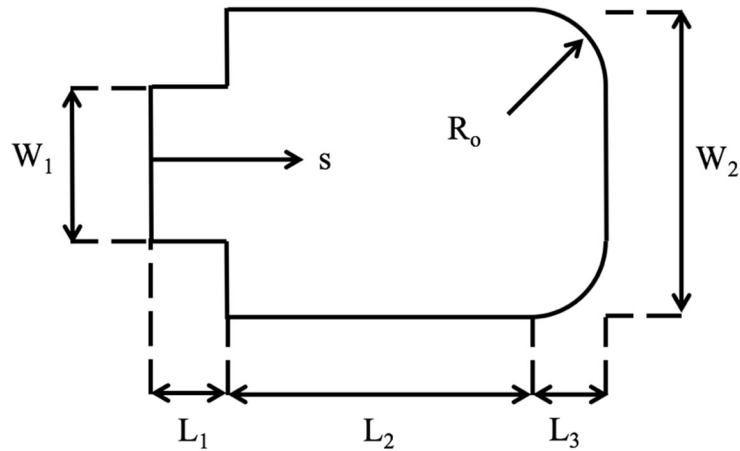
Figure 3.8. Parameters defining the two-dimensional geometry of a reed with a step change in width and rounded tip.

To calculate the tip deflection of the reed given a pressure load, ΔP, the reed will be broken up into three sections and the deflections of each section will be calculated separately. Forces, F, and moments, M, between adjacent sections will be calculated to determine appropriate boundary conditions. It is assumed that deflection of the tip section, L_3, is negligible compared to the total tip deflection. A schematic of the approach is shown in Figure 3.9. Inherent in this approach is the assumption of small deflections.

64
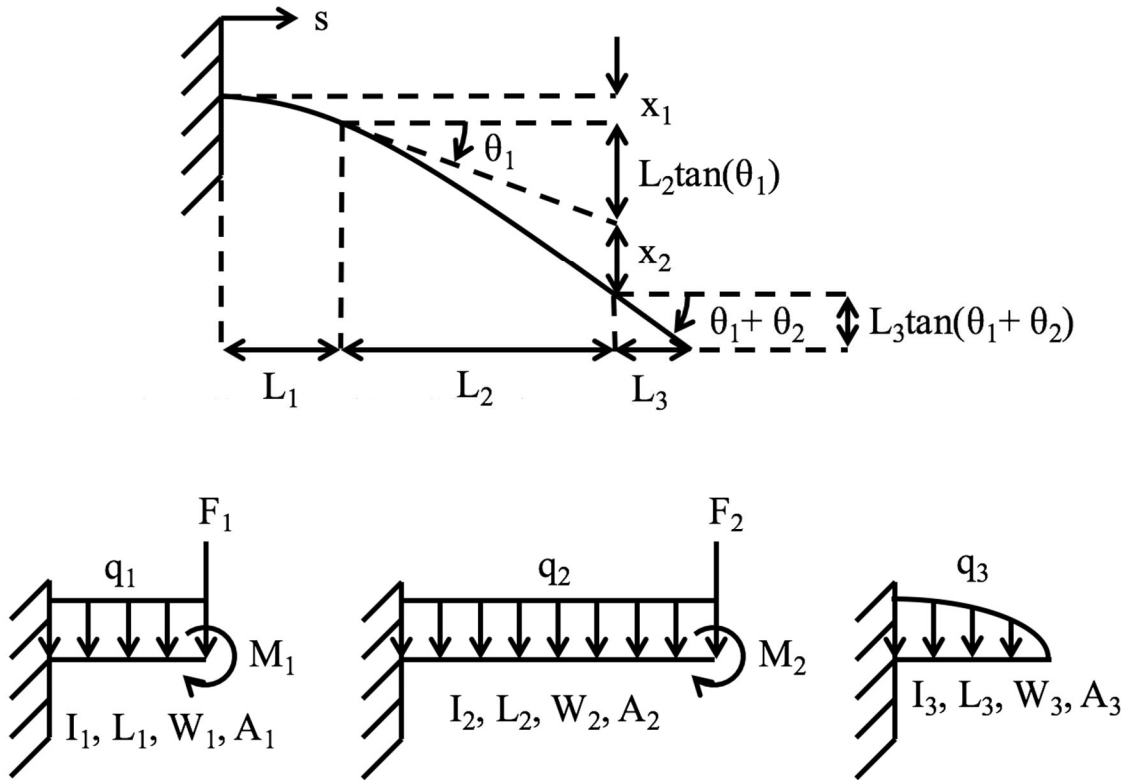
Figure 3.9. Schematic for analytically determining the deflection of a reed with a step change in width and rounded tip.

The force per unit length or distributed load is denoted by *q*. *I* is the area moment of inertia of the reed, and *A* is the face area. *θ* is the angle of the reed relative to horizontal. Calculation of the length and area of each section is straightforward and summarized in Table 3.5.

Table 3.5. Geometric formulas for a stepped reed with rounded tip

Quantity	Subscript		
	1	2	3
Length, L	$R_1 L$	$L - L_1 - L_3$	R
Area, A	$L_1 W_1$	$L_2 W_2$	$R\left[W_2 - \left(2 - \dfrac{\pi}{2}\right)R\right]$

Deflection of each cantilever reed section can be calculated from the distributed loads, forces and moments using beam deflection formulas, which assume a uniform, homogenous, linear elastic, slender beam experiencing small deflection. From the small angle approximation,

$$\frac{dv}{ds} = \tan \theta(s) \cong \theta(s) \tag{3.31}$$

The radius of curvature, ρ, is related to the bending moment by the flexural rigidity, EI:

$$\frac{1}{\rho} = \frac{M}{EI} \tag{3.32}$$

Considering a differential arc of the reed, the radius of curvature is related to the differential change in angle of the reed as

$$ds = \rho d\theta \tag{3.33}$$

Combining Equation 3.31 through 3.33 yields the following relationships between the moment, shear force, V, distributed load, flexural rigidity, and beam deflection:

$$M(s) = EI \frac{d^2 v}{ds^2} \tag{3.34}$$

66

$$V(s) = \frac{dM}{ds} = EI\frac{d^3v}{ds^3} \tag{3.35}$$

$$q(s) = \frac{dV}{ds} = EI\frac{d^4v}{ds^4} \tag{3.36}$$

Four boundary conditions are required to solve for the deflection as a function of distributed load. For a cantilever, the boundary conditions at the clamped end are: $v(0) = \frac{dv}{ds}(0) = 0$. At the free end, in the absence of an applied force or moment, the boundary conditions are: $M(L) = V(L) = 0$. If, at the free edge, a force or moment is applied, Dirichlet boundary conditions are used instead. Integrating over the length of the cantilever gives the total deflection. Deflections from distributed loads, forces and moments can be superimposed. A summary of the quantities calculated for a beam bending analysis is given in Table 3.6. Deflection and slope formulas for a range of beam boundary conditions and loading cases can be found many mechanics of materials texts (Gere & Timoshenko 1997).

Table 3.6. Beam bending formulas for a stepped reed with rounded tip

Quantity	Symbol	Formula – Subscript 1	Formula – Subscript 2
Distributed Load	q	$\Delta P W_1$	$\Delta P W_2$
Force	F	$\Delta P(A_2 + A_3)$	$\Delta P A_3$
Moment	M	$\Delta P A_2 \dfrac{L_2}{2} + F_2 L_2 + M_2$	$\Delta P R^2 \left(\dfrac{W_2}{2} - \dfrac{R}{3}\right)$
Tip Displacement	x	$\dfrac{q_1 L_1^{\,4}}{8EI_1} + \dfrac{F_1 L_1^{\,3}}{3EI_1} + \dfrac{M_1 L_1^{\,2}}{2EI_1}$	$\dfrac{q_2 L_2^{\,4}}{8EI_2} + \dfrac{F_2 L_2^{\,3}}{3EI_2} + \dfrac{M_2 L_2^{\,2}}{2EI_2}$
Tip Angle	θ	$\dfrac{q_1 L_1^{\,3}}{6EI_1} + \dfrac{F_1 L_1^{\,2}}{2EI_1} + \dfrac{M_1 L_1}{EI_1}$	$\dfrac{q_2 L_2^{\,3}}{6EI_2} + \dfrac{F_2 L_2^{\,2}}{2EI_2} + \dfrac{M_2 L_2}{EI_2}$

Calculation of the bending moment between the second and third sections is complicated by the presence of a rounded tip. The moment is calculated as follows:

$$M_2 = \int_{L_1+L}^{L} \Delta P W(s)(s - L_1 - L_2)\,ds = \Delta P R^2 \left(\frac{W_2}{2} - \frac{R}{3}\right) \tag{3.37}$$

Finally, the tip deflection is calculated by summing the deflection of each section along with additional displacement due to the initial angle of the second and third sections.

$$x = x_1 + L_2 \tan(\theta_1) + x_2 + L_3 \tan(\theta_1 + \theta_2) \tag{3.38}$$

The small angle approximation, $\tan(\theta) \approx \theta$, further simplifies calculation of tip deflection.

$$x = x_1 + L_2 \theta_1 + x_2 + L_3 (\theta_1 + \theta_2) \tag{3.39}$$

Reed stiffness can now be computed by dividing ΔP by x as calculated according to Equation 3.30. For stepped reed #2 this method yields a stiffness of 8.702 MPa/m. Note that for small angles, the stiffness is independent of ΔP and x.

For the case where $R_o = 0$, such as stepped reed #1, computation of the reed stiffness simplifies to the following expression, which is a function of the reed geometry and material elastic modulus only:

$$\kappa = \frac{24EI_1}{3W_1L_1{}^4 + (4W_1 + 8W_2)L_1{}^3L_2 + 18W_2L_1{}^2L_2{}^2 + 12W_2L_1L_2{}^3 + \frac{3}{2}W_2L_2{}^4} \quad (3.40)$$

Inputting the appropriate values from Table 3.1 into Equation 3.40 yields a reed stiffness of 7.345 MPa/m.

3.5.1 Finite Element Analysis Validation

A convenient, computationally efficient method of estimating the reed stiffness was developed in the previous section. This method makes use of several assumptions, the validity of which may not be immediately obvious. Therefore, to validate the method, it was compared to FEA results for two reed geometries – stepped reed #1 and stepped reed #2.

First, stepped reed #1 was modeled in commercial CAD software capable of a static FEM load analysis. The clamped end was fixed and a uniform pressure load was applied as shown in Figure 3.10. Dividing the applied pressure load by the tip deflection yielded a reed stiffness of 7.087 MPa/m. The FEA solution was considered the correct solution so that the percent error in the analytical model (Euler-Bernoulli or E-B) is $\frac{\kappa_{E-B} - \kappa_{FEA}}{\kappa_{FEA}} =$ +3.64%.
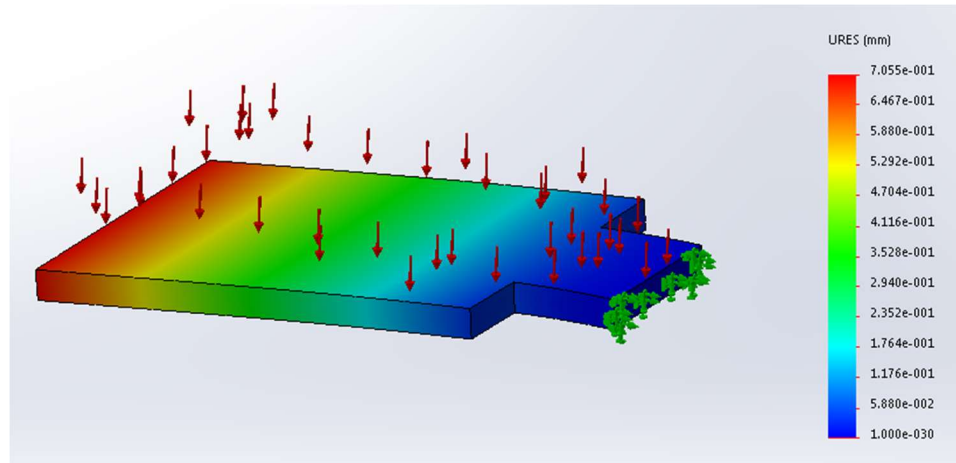
Figure 3.10. FEM static load analysis of stepped reed #1.

Second, the stepped reed #2 was considered. In this case, the analytical method gave a reed stiffness of 8.702 MPa/m. As expected, rounding the tip increases the reed stiffness since it decreases reed area near the tip where force has the largest effect on deflection. FEM static load analysis of the rounded reed is shown in Figure 3.11. The applied pressure force was divided by tip deflection to yield a stiffness value of 8.399 MPa/m. Percent error in the analytical model is then $\frac{\kappa_{E-B} - \kappa_{FEA}}{\kappa_{FEA}} = +3.61\%$.
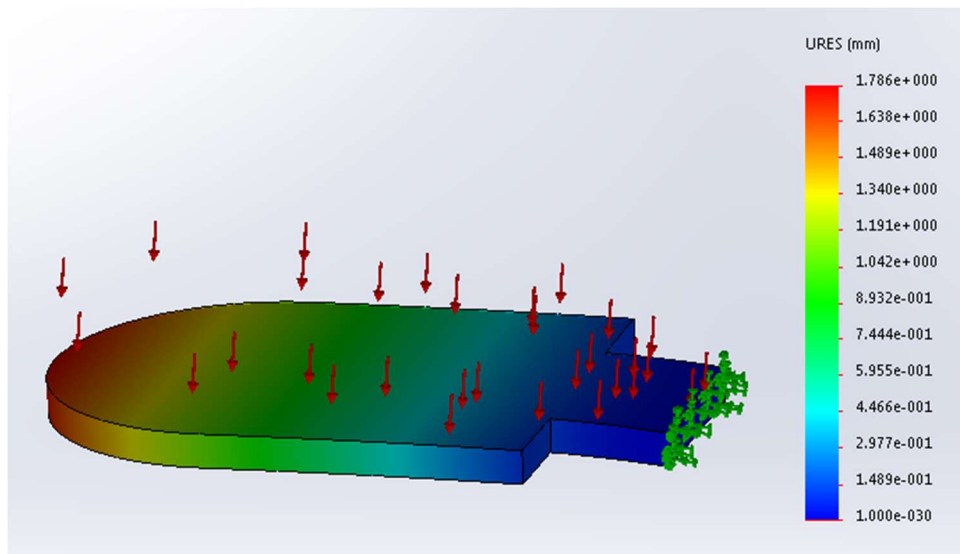
Figure 3.11. FEM static load analysis of stepped reed #2.

As expected, the stiffness of the reed is slightly over-predicted by Euler-Bernoulli beam theory. Exclusion of shear flexibility causes the shear stiffness and therefore reed stiffness to be over-predicted. However, the error is quite small, suggesting the analytical model is valid for estimated reed stiffness within ~4%.

3.5.2 Stiffness Uncertainty

In addition to error in the modeling and design of reed valves, uncertainty in reed stiffness due to manufacturing tolerances is to be expected. Uncertainty in reed thickness, h, is the dominant uncertainty so that other sources are negligible.

$$\frac{\delta\kappa}{\kappa} \cong \frac{1}{\kappa}\frac{\partial\kappa}{\partial h}\delta h = 3\frac{\delta h}{h} \tag{3.41}$$

A reasonable manufacturing tolerance for reed materials such as spring steel on the order of 1 mm thick is ±5%. Therefore, the relative uncertainty in reed stiffness due to manufacturing tolerances is 30%. This is nearly an order of magnitude higher than the error associated with using Euler-Bernoulli beam theory to calculate stiffness, illustrating the importance of tight tolerance for the reed thickness.

3.6 Mode Function and Mode Function Parameters

Knowledge of the beam mode function is necessary to determine many of the reed valve model parameters, such as those defined in Table 3.4. In this section, methods of calculating the mode function and mode function parameters will be developed. Values of the mode function parameters for a uniform reed and stepped reeds #1 and #2 will be given.

3.6.1 Direct Analytical Calculation of Mode Function Parameters

To compute the mode function for a beam with a step and rounded tip, the same approach used to calculate the tip displacement was employed. However, the cantilever

deflection as a function of location along the reed must be determined rather than simply at tip. Assuming a uniform, homogenous, linear elastic, slender, beam experiencing small deflection, deflection due to distributed loads, forces and moments may be calculated using the formulas in Table 3.7.

Table 3.7. Uniform cantilever beam deflection formulas

Distributed load, q	$v(s) = \dfrac{qs^2}{24EI}(s^2 + 6L^2 - 4Ls)$
Force, F, at free end	$v(s) = \dfrac{Fs^2}{6EI}(3L - s)$
Moment, M, at free end	$v(s) = \dfrac{Ms^2}{2EI}$

Deflection of the first and second reed section is found by superimposing deflection caused by the distributed pressure load and force and moment at the free end:

$$v(s) = \frac{q_1 s^2}{24EI_1}\left(s^2 + 6L_1{}^2 - 4L_1 s\right) + \frac{F_1 s^2}{6EI_1}(3L_1 - s) + \frac{M_1 s^2}{2EI_1}, \qquad (3.42)$$

$$s < L_1$$

$$v(s) = x_1 + (s - L_1)\theta_1 \qquad (3.43)$$

$$+ \frac{q_2(s - L_1)^2}{24EI_2}\left[(s - L_1)^2 + 6L_2{}^2 - 4L_2(s - L_1)\right]$$

$$+ \frac{F_2(s - L_1)^2}{6EI_2}[3L_2 - (s - L_1)] + \frac{M_2(s - L_1)^2}{2EI_2},$$

$$L_1 \leq s \leq L_1 + L_2$$

Since the deflection of the third section is neglected and the small angle approximation is employed, deflection of the third section is described by:

$$v(s) = x_1 + (s - L_1)\theta_1 + x_2 + (s - L_1 - L_2)(\theta_1 + \theta_2), \qquad (3.44)$$

$$s > L_1 + L_2$$

By definition, the mode function is then calculated as

73

$$\psi(s) = \frac{v(s)}{v(L)} \tag{3.45}$$

To understand how the mode functions depends on the load case and reed geometry, the mode function for several cases are shown in Figure 3.12. Details on the mode shape of a stepped reed in free vibration can be found in the literature (Naguleswaran 2002). The mode function parameters of each case shown in Figure 3.12 were calculated according to their definition as given in Table 3.4. The results are summarized in Table 3.8.
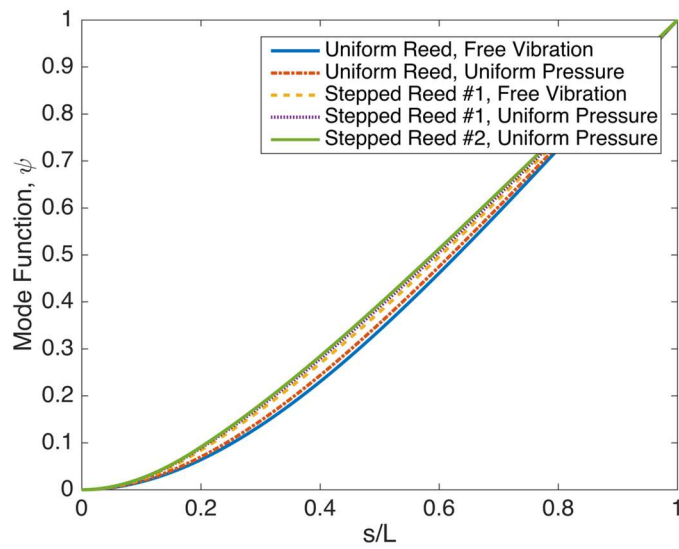
Figure 3.12. Mode functions for a uniform and stepped reeds in free vibration and under a uniformly distributed load

Table 3.8. Comparison of mode function parameters for the uniform and stepped reeds in free vibration and under a uniform distributed load

Case	γ_1	γ_2	γ_3
Uniform Reed, Free Vibration	1.566	0.7389	1
Uniform Reed, Uniform Load	1.558	0.7405	1
Stepped Reed #1, Free Vibration	1.541	0.7415	0.9998
Stepped Reed #1, Uniform Load	1.534	0.7430	0.9998
Stepped Reed #2 Uniform Load	1.640	0.6986	0.8663

Note that the mode function has not been calculated for the prototype reed or stepped reed #2 in free vibration. The author is unaware of simple analytical methods for determining the mode function in these cases. However, since the mode function parameters are relatively insensitive to reed geometry, estimates may be reasonably made from reeds of similar geometry with known mode functions.

3.6.2 Alternate Methods for Calculating First Mode Function Parameter

In the preceding section, the mode function parameters were computed directly by numerically integrating the mode function. For simple geometries, such as the uniform reed or stepped reed #1, the first mode function parameter may be calculated for a reed in free vibration using a simplified approach. Consider a reed freely vibrating in a vacuum with no damping. In this case, the equation of motion simplifies to

$$\ddot{x} + \frac{\gamma_1 \kappa}{\rho_c h_{eff}} x = 0 \qquad (3.46)$$

From the solution to Equation 3.47, it follows that the natural frequency of the reed is given by

$$\omega_n = \sqrt{\frac{\gamma_1 \kappa}{\rho_c h_{eff}}} \tag{3.47}$$

Combining Equation 3.46 and 3.47, the first mode function parameter can be calculated as

$$\gamma_1 = \frac{\rho_c h_{eff} \omega_n^2}{\kappa} \tag{3.48}$$

Returning to stepped reed #1, as previously calculated, the analytical natural frequency and reed stiffness are 2427 rad/s and 7.345 MPa/m respectively. From Equation 3.48, the first mode function parameter is calculated to be 1.527. This value is slightly lower than the value 1.534 calculated from integrating the mode function directly. The likely reason for the discrepancy is that analytical calculation of the reed stiffness assumes a uniform pressure load on a static reed, which is not the case for a reed in free vibration.

Alternatively, for complex geometries, finite element analysis can provide values of the reed natural frequency and stiffness instead of seeking analytical expressions. As calculated previously with FEA, the natural frequency and reed stiffness of stepped reed #1 is 2383 rad/s and 7.087 MPa/m respectively. Inputting these values into Equation 3.49 gives a value of 1.525 for the first mode function parameter. Again, it should be emphasized that this method gives an estimation of the mode function parameter that decreases computational cost at the expense of accuracy. A comparison of the three methods discussed for calculating the first mode function parameter is given in Table 3.9.

Table 3.9. Comparison of methods to calculate the first mode function parameter for stepped reed #1

Method	ω_n (rad/s)	κ (MPa/m)	γ_1
E-B direct integration	2427	7.345	1.534
E-B alternative	2427	7.345	1.527
FEA alternative	2383	7.087	1.525

3.7   Pressure Load Multiplier

Development of a single degree of freedom, lumped parameter, analytical reed valve model greatly simplifies simulation and significantly decreases computational cost. It is imperative, however, to keep in mind that fluid flow through the valve and reed motion are, in reality, three dimensional. This does not necessarily mean a single degree of freedom, lumped parameter model is insufficient. Rather, two or three dimensional phenomena that have a significant effect on reed valve behavior must be identified and accounted for in the model.

The pressure and flow field around a check valve are both three dimensional and non-uniform. To capture the flow physics through a check valve, experiments can be done to measure the discharge coefficient resulting in an accurate flow rate model (Knutson & Van de Ven 2016b). In a similar fashion, the pressure field, which drives reed motion, can be characterized through the pressure load multiplier, defined in Table 3.4. If the pressure differential varies in two dimensions, *s* and *t*, on the reed surface, the pressure load multiplier can be calculated as

$$X = \frac{1}{\Delta P_{u-d}} \frac{\iint_A \psi \Delta P \, dA}{\int_0^L \psi W ds} \tag{3.49}$$

Two regimes of flow through the valve were considered in this work. First, when the reed opening is small relative to the sealing width, the flow has a low Reynolds number and is comparable to Poiseuille flow between plates, which can be described by the Reynolds equation (Hamrock et al. 2004). Second, when the reed opening is large relative to the sealing width, the flow is comparable to flow through an orifice. While analysis of the latter lends itself quite well to experimental analysis, the former is more difficult to quantify, especially if stiction forces are significant. As such, analysis of the Poiseuille flow regime is intended to be approximate rather than exact. More complex methods such as computational fluid dynamics, could be used to provide a more accurate analysis, but are beyond the scope of this work.

3.7.1 Poiseuille Flow Regime

For small valve openings, flow between the reed and seat is expected to be dominated by pressure and viscous terms. In this case, a pressure gradient develops across the sealing width to balance viscous friction. The pressure in this region is varies between P_{down} and P_{up} as shown in Figure 3.13. Although the reed is not necessarily parallel with the seat, for small openings, when the angle of the reed relative to the seat is small, a parallel plate assumption is reasonable.
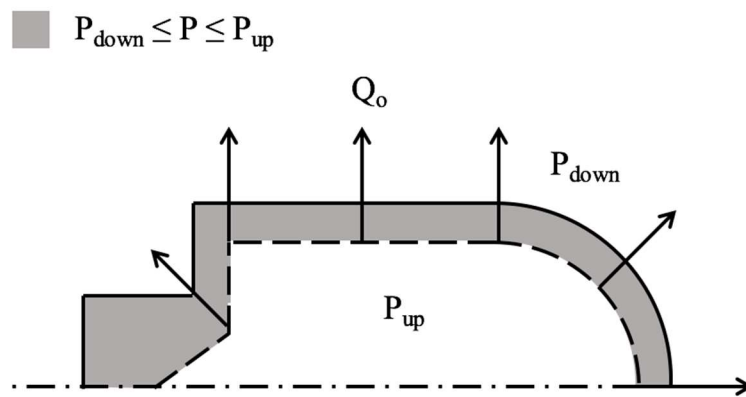
Figure 3.13. Pressure on the upstream side of the reed.

Four distinct sections of the reed, shown in Figure 3.14, will be considered for the purpose of estimating the pressure on the upstream side of the reed. The first section is directly exposed to upstream pressure. The second section is the sealing width along the side of the reed which will be analyzed as flow between parallel surfaces of infinite length in one dimension. The third section is the sealing width along the rounded tip, which will be analyzed as flow between a parallel plate and annulus. In the fourth section of the reed – the base – it is less clear what the flow field looks like. However, as will be shown, the pressure in the fourth section does not have a significant effect on the deflection of the reed and therefore the pressure load multiplier is relatively insensitive to the pressure in this section.
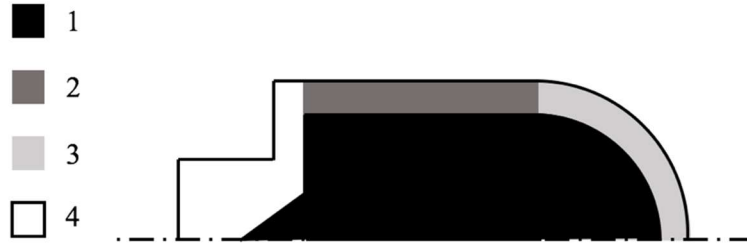
Figure 3.14. Reed sections assumed for determining the pressure differential

For analysis, the spatially averaged pressure across the sealing width will be considered rather than the spatially varying pressure. In calculation of the pressure load multiplier, the pressure differential is multiplied by the mode function, which is a function of location along the length of the reed. Therefore, the use of spatially averaged pressure will introduce error, however, for relatively small sealing widths, the error is expected to be insignificant.

3.7.1.1 Parallel Surface of Infinite Length

To determine the pressure in reed Section 2, consider a plate of width W and infinite length such that the flow is one dimensional. The plate is moving normal to the surface at a velocity u. Dirichlet boundary conditions for pressure are imposed on either side if the finite width. Figure 3.15 shows a diagram of the problem.
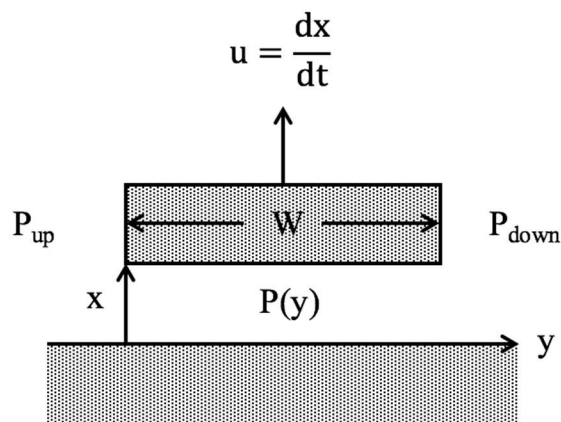
Figure 3.15. Plate of finite width and infinite length parallel to a surface.

For the problem of flow between a plate of infinite length parallel to a surface, the Reynolds equation in Cartesian coordinates simplifies to

$$\frac{d^2P}{dy^2} = \frac{12\mu u}{x^3} \tag{3.50}$$

where μ is the dynamic viscosity of the fluid. Boundary conditions are $P(y = 0) = P_{up}$ and $P(y = W) = P_{down}$. Integrating Equation 3.50 and subtracting the downstream pressure results in an expression for the pressure differential across the width of the plate:

$$\Delta P(y) = \left(\Delta P_{u-d} - 6\mu Wy\frac{u}{x^3}\right)\left(1 - \frac{y}{W}\right) \tag{3.51}$$

When there is a normal relative velocity between the plate and surface, a stiction effect occurs. Stiction has an inverse cubic dependence on gap height, x, so that even if variation in gap height is small as previously assumed, variation in the inverse cubic of gap height may be significant. In such a case, the pressure distribution is two dimensional and the assumption of one dimensional flow is invalid. To simplify the analysis, stiction will be neglected. Neglecting stiction, the pressure differential becomes

$$\Delta P(y) = \Delta P_{u-d}\left(1 - \frac{y}{W}\right) \tag{3.52}$$

The average pressure differential across the width of the plate is then

$$\overline{\Delta P} = \frac{1}{W}\int_0^W \Delta P_1(y)dy = \frac{1}{2}\Delta P_{u-d} \tag{3.53}$$

3.7.1.2 Parallel Surface and Annulus

To model flow between the seat and the reed tip, consider an annulus of inner radius R_i and outer radius R_o as shown in Figure 3.16.
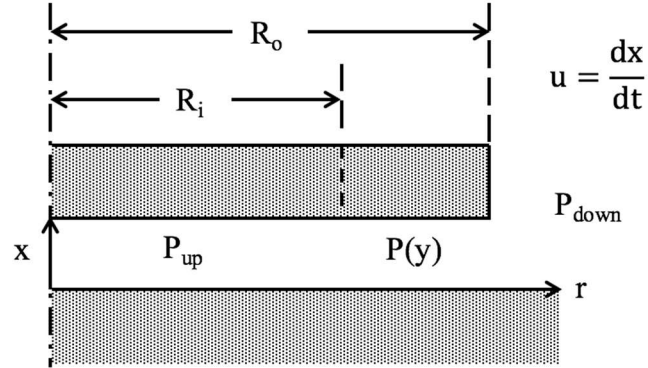
Figure 3.16. Annulus parallel to a surface.

If the flow is assumed to be axially symmetric so that the pressure is a function of radial coordinate only, the Reynolds equation in cylindrical coordinates simplifies to

$$\frac{d}{dr}\left(rx^3\frac{dP}{dr}\right) = 12\mu r u \tag{3.54}$$

For positive flow through the reed valve, the boundary conditions are $P(r = R_i) = P_{up}$ and $P(r = R_o) = P_{down}$. Solving Equation 3.54 and subtracting the downstream pressure results in an expression for the pressure differential across the radius of the annulus:

$$\Delta P(r) = \frac{\Delta P_{u-d}\ln\frac{R_o}{r} - \frac{3\mu u}{x^3}\left(r^2\ln\frac{R_i}{R_o} + R_i\ln\frac{R_o}{r} + R_o\ln\frac{r}{R_i}\right)}{\ln\frac{R_o}{R_i}} \tag{3.55}$$

Neglecting stiction effects, the pressure differential becomes

$$\Delta P(r) = P_{u-d} \frac{\ln \frac{R_o}{r}}{\ln \frac{R_o}{R_i}} \tag{3.56}$$

The spatially averaged pressure around the annulus is calculated as follows:

$$\overline{\Delta P} = \frac{1}{\left[\frac{\pi\left(R_o{}^2 - R_i{}^2\right)}{2}\right]} \int_0^\pi \int_{R_i}^{R_o} \Delta P(r) r \, dr \, d\theta \tag{3.57}$$

$$= \left[\frac{1}{2 \ln \frac{R_o}{R_i}} - \frac{1}{\left(\frac{R_o}{R_i}\right)^2 - 1}\right] \Delta P_{u-d}$$

3.7.1.3 Pressure Load Multiplier Calculation

For both a plate of infinite length and an annulus, when stiction is ignored, the average pressure is a constant fraction of the overall pressure drop. An average pressure differential fraction, F, is defined as

$$F = \frac{\overline{\Delta P}}{\Delta P_{u-d}} \tag{3.58}$$

In reed section 1, which is directly exposed to upstream pressure, the average pressure differential is simply the total pressure drop so that $F_1 = 1$. From Equation 3.53, the second section has an average pressure differential fraction of 0.5. From inspection of Equation 3.57, the average pressure differential fraction for the third section is

$$F_3 = \frac{1}{2 \ln \frac{R_o}{R_i}} - \frac{1}{\left(\frac{R_o}{R_i}\right)^2 - 1} \tag{3.59}$$

Without an analytical method to compute the flow field in the fourth section, the value of F_4 remains unknown. The pressure load multiplier is expressed in terms of the average pressure differential fraction as

$$X = \frac{\iint_A \psi F \, dA}{\int_0^L \psi W \, ds} \tag{3.60}$$

3.7.2   Orifice Flow Regime

While the reed valve is treated as an orifice for the purpose of computing the flow rate, in reality the pressure decreases from the upstream to the downstream over a finite distance rather than instantaneously. It is therefore difficult to compute the pressure field analytically when the reed valve opening is large relative to the sealing width and Poiseuille flow can no longer be assumed. Also, the pressure field may change as a function of reed opening further complicating analysis. Therefore, a computational or experimental method is required to characterize the pressure field in the orifice flow regime. The former method has been used to compute the pressure load multiplier for reed valves in secondary air injection applications (Battistoni & Grimaldi 2005). Advantages of a computational fluid dynamics approach include the ability to visualize the pressure field and simulate steady state backflow.

Experimental determination of the pressure load multiplier can be made by measuring the opening of the reed valve and pressure drop across it. Solving the equation of motion for X, gives the following expression:

$$X = \frac{\kappa(x - x_0)}{\Delta P_{u-d}} \tag{3.61}$$

Given the reed stiffness, the pressure load multiplier can be computed from experimental measurements of pressure drop and reed tip displacement in order to develop an empirical correlation.

3.8 Determination of Experimental Reed Valve Parameters

Thus far, an approach to modeling reed valves of a generic geometry with validation and examples of specific geometries has been presented. In this section, the prototype reed valve will be characterized. A detailed analysis including analytical, computational, and experimental methods of determining its parameters will be performed. The purpose of this section is twofold; first to provide practical methods of determining reed valve model parameters and second to calculate parameters of the reed valve prototype for experimental validation of the valve model.

3.8.1 Effective Thickness

Previously, the concept of an effective reed thickness was introduced as a means to account for a non-uniform reed thickness. In the case of reed grooves, the depth and location will affect static and dynamic behavior of the reed. To account for variable thickness, consider a reed freely vibrating in a vacuum with no damping. Solving Equation 3.48 for the effective thickness yields

$$h_{eff} = \frac{\gamma_1 \kappa}{\rho_c \omega_n^2} \tag{3.62}$$

To calculate the effective thickness, all quantities of the right hand side of Equation 3.63 must be known. Recognizing that the mode function is relatively insensitive to geometric variations, the first mode function parameter for stepped reed #2 under a uniform load will be used as an approximation. From Table 3.8, the value of the first mode function parameter for this case is 1.640. Next, the reed stiffness must be determined. Consider the static prototype reed subjected to a uniform pressure distribution with $x_0 = 0$ as shown in Figure 3.17.
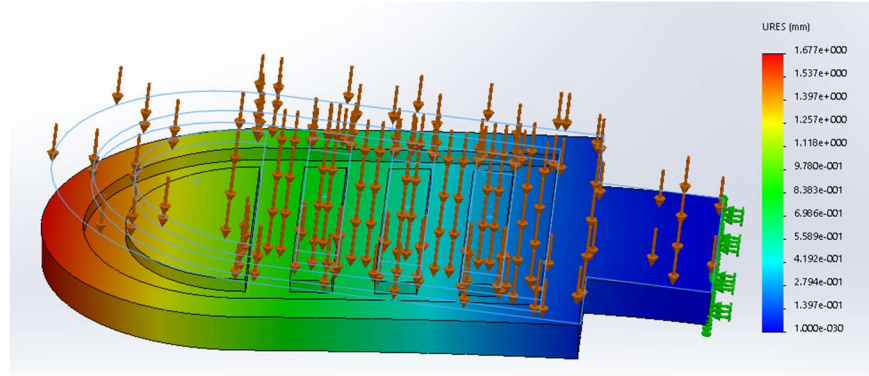
Figure 3.17. FEA determination of reed stiffness.

Using commercial FEA software, a uniform pressure load was applied to the reed face and the tip deflection was measured. The reed stiffness was then calculated to be 6.353 MPa/m from Equation 3.30. In the same FEA software, the natural frequency was calculated to be 2523 rad/s. Given a density of 1410 kg/m^3 for Delrin, the effective thickness of the reed is 1.161 mm according to Equation 3.62.

3.8.2   Internal Damping Coefficient and Reed Stiffness

Internal damping is difficult to accurately characterize analytically so experiments are often used to develop empirical damping models. Further, while reed stiffness is easy to calculate using FEA, uncertainty in material properties and manufacturing tolerances lead to an uncertainty in stiffness, which can be significant, as previously discussed. For these reasons, the reed internal damping and stiffness were measured experimentally.

3.8.2.1 Experimental Measurement of Internal Damping and Reed Stiffness

To determine c and κ, the prototype reed was clamped and mounted vertically in air. The reed was plucked to provide a position step input and its response was measured with a laser triangulation sensor (LTS) as shown in Figure 3.18.
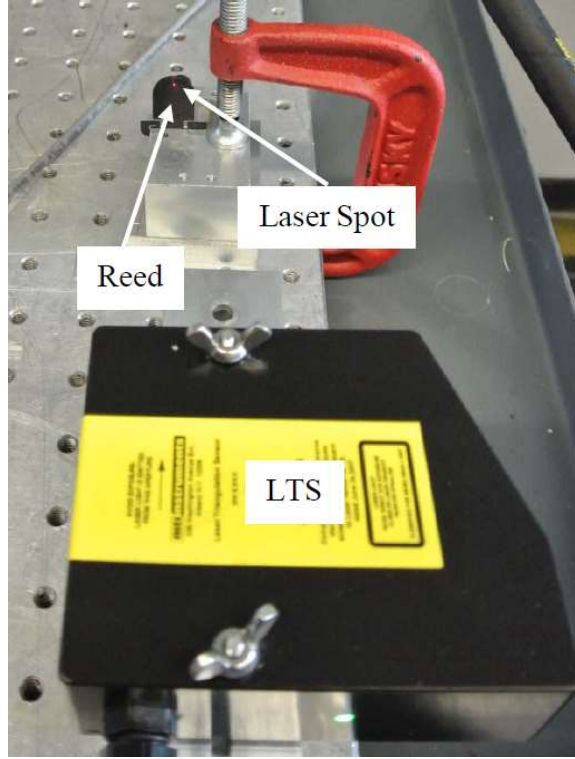
Figure 3.18. Experimental measurement of reed vibration using an LTS.

The LTS outputs a voltage differential, ΔV, proportional to displacement of the target. In air, the scale factor, C_{LTS}, is 2.5 mm/V. For the experiments described in this section, the sampling frequency was set to 20 kHz.

Assuming the added fluid mass and fluid damping of air are negligible, the equation of motion becomes

$$\ddot{x} + \frac{\gamma_1 c_c}{\rho_c h_{eff}} \dot{x} + \frac{\gamma_1 \kappa}{\rho_c h_{eff}} (x - x_0) = 0 \tag{3.63}$$

Noting that x = v/ψ, the equation of motion may also be expressed in terms of reed displacement, v, at a location other than the tip as

$$\ddot{v} + \frac{\gamma_1 c_c}{\rho_c h_{eff}} \dot{v} + \frac{\gamma_1 \kappa}{\rho_c h_{eff}} (v - v_0) = 0 \tag{3.64}$$

Equation 3.64 is a second-order ordinary differential equation that has an analytical solution. For an underdamped system, the solution is

$$v(t) - v_0 = C_3 exp\left(-\frac{\gamma_1 c_c}{2\rho_c h_{eff}}t\right)\sin(\omega_d t + \varphi) \tag{3.65}$$

where C_3 and ϕ are a constants and ω_d is the damped natural frequency. Since $v(t) - v_0 = C_{LTS}\Delta V(t)$, the reed response may be written directly in terms of the LTS output voltage as

$$\frac{\Delta V(t)}{V_{max}} = \frac{A_1}{V_{max}C_{LTS}} exp\left(-\frac{\gamma_1 c_c}{2\rho_c h_{eff}}t\right)\sin(\omega_d t + \varphi) \tag{3.66}$$

Noting that A_1, V_{max}, and C_{LTS} are constants, the reed response can be expressed in terms of a constant C_4 as

$$\frac{\Delta V(t)}{V_{max}} = C_4 exp\left(-\frac{\gamma_1 c_c}{2\rho_c h_{eff}}t\right)\sin(\omega_d t + \varphi) \tag{3.67}$$

A total of six responses were measured as shown in Figure 3.19.
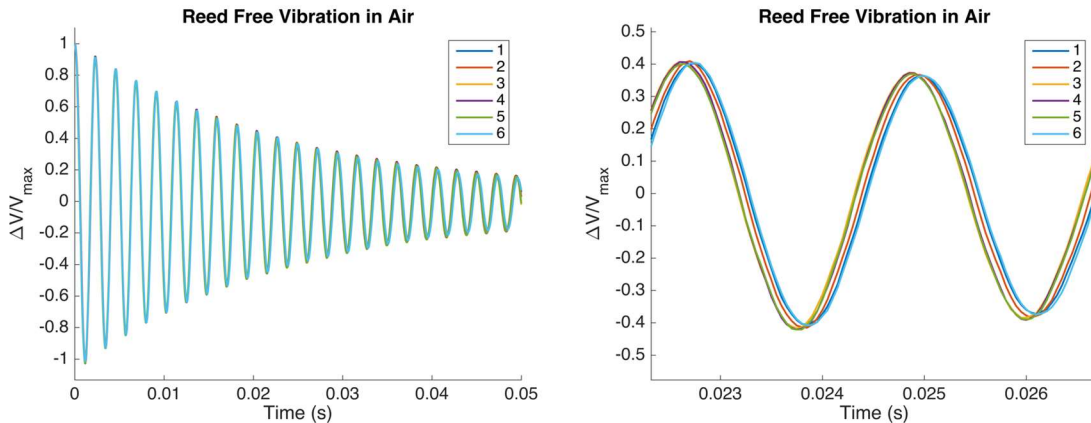
Figure 3.19. Experimental measurement of reed in free vibration

The reed response was remarkably repeatable. Data was curve fit with Equation 3.67 using a non-linear least squares method as shown in Figure 3.20.
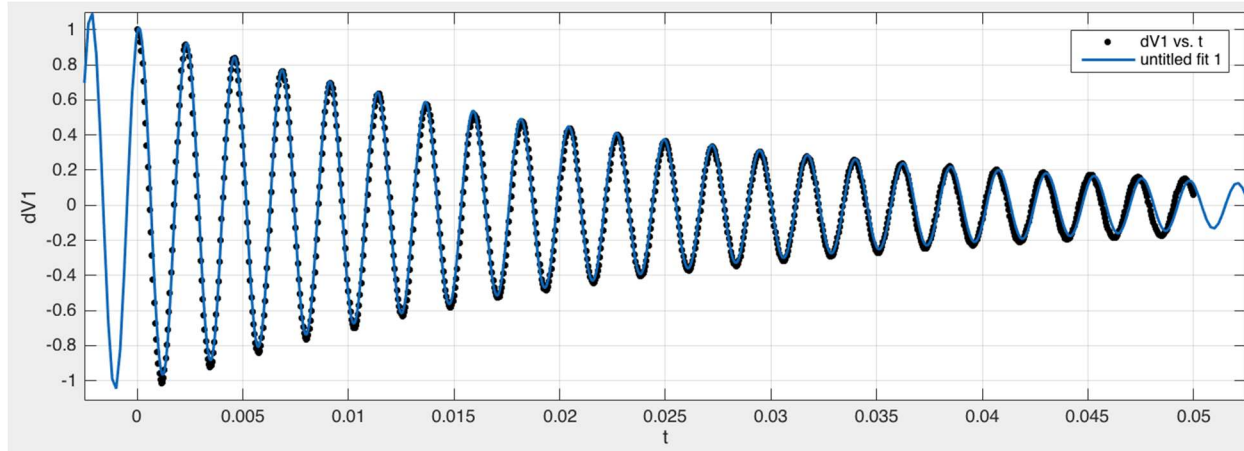
Figure 3.20. Curve fit (blue) of experimental data (black), run 1.

By definition, the damped natural frequency, ω_d, is given by

$$\omega_d{}^2 = (1 - \zeta^2)\omega_n{}^2 \tag{3.68}$$

where

$$\zeta^2 = \left(\frac{\gamma_1 C_c}{2\rho_c h_{eff}\omega_n}\right)^2 \tag{3.69}$$

Combining Equations 3.68 and 3.69 yields an expression for the undamped natural frequency:

$$\omega_n = \sqrt{\omega_d{}^2 + \left(\frac{\gamma_1 C_c}{2\rho_c h_{eff}}\right)^2} \tag{3.70}$$

In terms of the damping ratio and undamped natural frequency, the governing equation of a spring-mass-damper system is

$$\ddot{v} + 2\zeta\omega_n\dot{v} + \omega_n{}^2(v - v_0) = 0 \tag{3.71}$$

Solving Equation 3.48 for the square of the undamped natural frequency yields

$$\omega_n{}^2 = \frac{\gamma_1\kappa}{\rho_c h_{eff}} \tag{3.72}$$

Solving Equation 3.72 for the reed stiffness yields

$$\kappa = \frac{\rho_c h_{eff}\omega_n{}^2}{\gamma_1} \tag{3.73}$$

Curve fits provided values of $\frac{\gamma_1 c_c}{2\rho_c h_{eff}}$ and ω_d. In order to determine c_c, the value of γ_1 must be known. In the absence of an exact method to calculate γ_1, the value for stepped reed #2 under a uniform load – 1.640 – was used. The undamped natural frequency was then calculated according to Equation 3.70 and the reed stiffness was determined from Equation 3.73. A summary of the experimental results is given in Table 3.10.

Table 3.10. Prototype reed free vibration experimental results

Run	c_c (Pa*s/m)	ω_d (rad/s)	ω_n (rad/s)	κ (MPa/m)
1	79.18	2780	2780	7.674
2	77.52	2787	2787	7.713
3	75.88	2792	2792	7.741
4	76.00	2791	2791	7.735
5	77.07	2789	2789	7.724
6	79.34	2779	2779	7.669
Mean	77.50	2786	2786	7.709
Standard Deviation	1.501	5.573	5.573	0.03087
Uncertainty (±%)	0.3953	0.04083	0.04083	0.8174

The mean experimental reed stiffness of 7.709 MPa/m is 21% higher than the stiffness of 6.353 MPa/m determined by finite element analysis. The likely cause is a discrepancy in material properties and/or dimensions between the modeled and physical reed. The experimental value is chosen as the correct value for modeling purposes.

3.8.2.2 Effect of Added Mass and Damping

The effects of added fluid mass and damping on reed motion were neglected in calculation of internal damping and stiffness for a reed vibrating in air. To justify this assumption, the relative importance of reed mass and internal damping and fluid mass and damping will be investigated for air and hydraulic oil. Considering the added fluid mass and damping, the equation of motion of a reed freely vibrating in fluid is

$$\left(\rho_c h_{eff} + \gamma_3 \rho_{fluid} W_2 \frac{\pi}{4} \Gamma_f\right) \ddot{x} + \gamma_1 c \dot{x} + \gamma_2 \frac{1}{2} \rho_{fluid} \dot{x}^2 C_D \tag{3.74}$$
$$+ \gamma_1 \kappa (x - x_0) = 0$$

To determine the hydrodynamic function, Γ_f, the normalized mode number, κ_n, which depends on the natural frequency parameter, α, must be determined. For reeds of

complex geometry, and analytical solution may not exist for the natural frequency parameter. The natural frequency, however, may be determined experimentally or through FEA. Solving Equation 3.7 for the natural frequency parameter yields the following relationship where all the terms on the right hand side are known.

$$\alpha_1 = L \left(\frac{\omega}{h_{eff}} \right)^{1/2} \left(\frac{12\rho_c}{E} \right)^{1/4} \tag{3.75}$$

Note that this equation is derived for a reed of uniform thickness and is therefore not formally correct for a reed with grooves. Nonetheless, it will be used with the effective thickness as an approximation to estimate the value of the hydrodynamic function for a reed with grooves. A summary of the natural frequency and natural frequency parameter for reeds of various geometries is given in Table 3.11.

Table 3.11. Natural frequency and natural frequency parameter

Case	ω_n (FEA)	α (FEA)	α (Analytical)
Uniform Reed	3123 rad/s	1.899	1.875
Stepped Reed #1	2383 rad/s	1.695	1.674
Stepped Reed #2	2673 rad/s	1.757	N/A
Prototype Reed	2523 rad/s	1.845	N/A

With a natural frequency parameter of 1.845, the normalized mode number of the prototype reed, according to Equation 3.14, is 0.9677. From the Padé approximant representation, the value of the hydrodynamic function is 0.8850. The ratio of air mass to reed mass is then given by

$$\frac{air\ mass}{reed\ mass} = \frac{\gamma_3 \rho_{air} W_2 \frac{\pi}{4} \Gamma_f}{\rho_c h} \cong 0.0062 \ll 1 \tag{3.76}$$

The added fluid mass of air is less than 1% of the reed mass for the experiments, validating the assumption that fluid damping was negligible in the air experiments.

To determine the magnitude of fluid damping compared to internal damping of the reed, the drag coefficient must be determined. For a flat plate oscillating in liquid, the drag coefficient is considered independent of Reynolds number for $Re_W > 250$ (Buchanan & Shih 1971) where

$$Re_W = \frac{\rho_f U_{max} W}{\mu_f} \qquad (3.77)$$

and U_{max} is the maximum velocity reached during oscillation. A plot of measured reed velocity at the laser spot location is shown in Figure 3.21
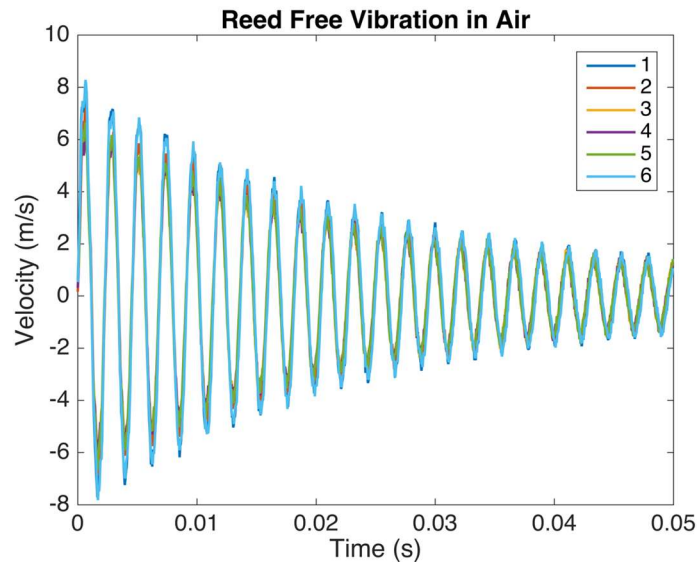
Figure 3.21. Reed velocity at the laser spot.

At 1 m/s, the Reynolds number according to Equation 3.78 is 1050. It is therefore reasonable to conclude that most of the reed is in the high Reynolds number regime where inertial forces dominate fluid damping and the drag coefficient is independent of Reynolds number. In an unconfined volume of fluid, the drag coefficient on a flat plate is approximately 1. The ratio of fluid damping to internal reed damping is therefore

$$\frac{inertial\ air\ damping}{internal\ damping} = \frac{\gamma_2 \frac{1}{2} \rho_{air} \dot{x}^2 C_D}{\gamma_1 c \dot{x}} \tag{3.78}$$

The ratio of fluid damping to internal reed damping is highest at the maximum velocity of approximately 8 m/s where Equation 3.78 yields a value of 0.027 $\ll$ 1, validating the assumption that fluid damping was negligible in the air experiments.

For a reed valve operating in hydraulic oil, the fluid viscosity is significantly higher than air. Furthermore, the reed is in a confined space close to a wall which increases the drag coefficient. Therefore, fluid damping may be significant in the context of a hydraulic reed valve, especially in high speed applications.

3.8.3   Viscous Fluid Damping Coefficient

Research on the damping of a reed in fluid has almost exclusively focused on the case of a reed vibrating at a circular frequency ω. In the case of a reed valve that contacts the stop, motion is closer to a square wave than sinusoidal. However, for a reed that doesn't hit the stop, such as the one examined in this thesis, the spring-mass effect of the reed induces vibrations in the fully open positon. The frequency of this vibration is expected to be near the damped natural frequency of the reed unless the surrounding fluid or pressure field induces vibration at a different frequency.

The viscous fluid damping coefficient per unit length, R_f, is a function of the kinetic Reynolds number, defined as (Naik et al. 2003):

$$R_k = \frac{\rho \omega W^2}{4\mu} \tag{3.79}$$

As an approximation, the frequency of vibration is estimated to be the reed undamped natural frequency, ω_n. From the experimental results summarized in Table 3.10, the prototype reed natural frequency is 2786 rad/s. Alternatively, a predictive, analytical

estimate of natural frequency could be made according to Equation 3.72. Recognizing that very little fluid damping is expected to come from the base of the prototype reed, the width used to compute the kinetic Reynolds is taken to be W_2. From Equation 3.79, the kinetic Reynolds number of the prototype reed is calculated to be 2250.

The relationship between kinetic Reynolds number and viscous fluid damping coefficient is shown in Figure 3.22 (Naik et al. 2003). For $R_k = 2250$, the non-dimensional viscous fluid damping coefficient, c_v/μ, is approximately 500. Note that c_v in Figure 3.22 is equivalent to R_f in this thesis. Therefore, $R_f = (c_v/\mu)\mu = 34.15$ Pa*s.
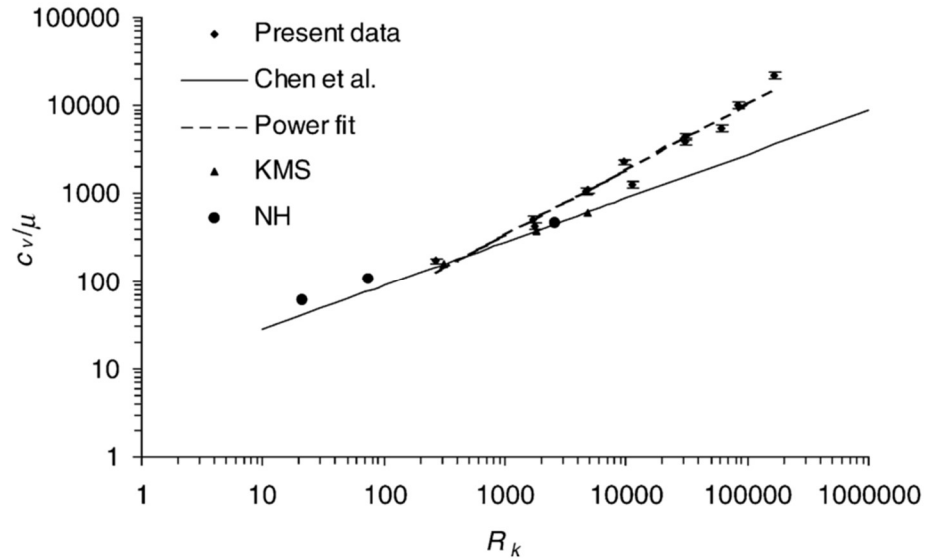
Figure 3.22. Normalized viscous damping coefficient vs. R_k (Naik et al. 2003).

Approximating R_f as constant, the viscous fluid damping coefficient is

$$c_f \cong \left(\frac{\int_0^L \psi^2 ds}{\int_0^L \psi W ds} \right) R_f = 1650 \ \frac{Pa * s}{m} \tag{3.80}$$

Finally, based on the results summarized in Table 3.10 and Equation 3.80, the combined viscous damping coefficient is

$$c = c_c + c_f = 1727 \ \frac{Pa*s}{m} \qquad (3.81)$$

The damping model described in this section is approximate since it was derived from vibrating reed data in contrast with pressure driven, square wave type motion. Results obtained through its use should be interpreted accordingly. If reed vibrations are induced when the valve is open, but not pressured against the stop, they will be damped. Since the frequency of oscillation and damping coefficient depend on each other, iteration is required. To avoid this, the natural frequency has been assumed, which may overestimate R_k and therefore R_f, c_f, and c. However, research has shown that when a cantilever in liquid is located near a wall, as is the case for reed valves, the damping term is increased (Naik et al. 2003). Further research is required to more accurately characterize these affects.

3.8.4 Pressure Load Multiplier

In the following analysis, the mode function for stepped reed #2 under a uniform load is used to calculate the pressure load multiplier for the prototype reed. Without an analytical method to calculate the mode function for a reed with grooves, such an approximation is necessary. As previous analysis has shown, the mode function is relatively insensitive to geometry and load and therefore this approximation is reasonable.

3.8.4.1 Poiseuille Flow Regime

The prototype reed has a sealing width of 1.59 mm and an outer radius of 7.94 mm, resulting in an inner radius of 6.35 mm. From Equation 3.59, the average pressure differential fraction for the third section is calculated as $F_3 = 0.463$. Figure 3.23 shows the average pressure differential fraction across the prototype reed face. The pressure distribution is difficult to quantify in the fourth section of the reed so the value of F_4 is unknown. However, since it is near the clamped end, it is expected to have a relatively minor influence on the pressure load multiplier.
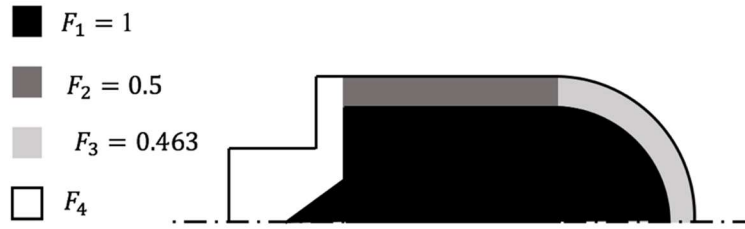
Figure 3.23. Average pressure fraction across the prototype reed.

If the mode function of the prototype reed is approximated as that of a reed of stepped reed #2 under a uniform pressure load, the mode function can be easily calculated analytically as described in Section 3.6.1. Then, given dimensions of the reed and an assumed value of F_4, the pressure load multiplier can be calculated from Equation 3.60. The pressure load multiplier as a function of values of F_4 between 0 and 1 is summarized in Table 3.12.

Table 3.12 Dependence of pressure load multiplier on F_4 for the experimental reed

Value of F_4	Pressure load multiplier, X
0	0.824
0.5	0.835
1	0.845

As expected, the pressure load multiplier is quite insensitive to the value of F_4, varying approximately 2.5% between the minimum and maximum possible values. For modeling purposes, the median value of $F_4 = 0.5$ is chosen resulting in $X = 0.835$ in the Poiseuille flow regime.

3.8.5 Orifice Flow Regime

At larger valve openings, fluid is no longer in the Poiseuille flow regime and the pressure distribution characteristics fundamentally change. As such, a method of characterizing the pressure load multiplier in the orifice regime must be developed. To

determine X, consider a static reed subjected to a non-uniform pressure distribution. Recall that in this case, the pressure load multiplier is given by

$$X = \frac{\kappa(x - x_0)}{\Delta P_{u-d}} \tag{3.82}$$

Equation 3.82 is especially well-suited for experimental determination of the pressure load multiplier. κ can be readily calculated analytically for simple geometries using the technique developed in Section 3.5 or with FEA for more complex geometries. The remaining terms on the right hand side can be measured in an experimental setup. For the prototype reed valve $\kappa = 7.709$ MPa/m and $x_0 = -0.18$ mm.

Experimental determination of the pressure load multiplier was achieved by using a hydraulic power unit in series with a needle valve to set the flow rate through the reed valve, which was measured with a gear flow meter downstream of the needle valve. A pair of pressure transducers measured the upstream and downstream pressure to determine ΔP_{u-d} while a laser triangulation sensor measured the tip opening, x. Steady state measurements were averaged over a ten second sampling period. Results of the experiment are shown in Figure 3.24. Note that transition between Poiseuille and orifice flow is taken to be the point where the respective correlations intersect. Using a non-linear least squares rational fit, the correlation, assuming X is a function of tip opening only, is

$$X(x) \tag{3.83}$$
$$= max\left[0, min\left(0.835, \frac{-52.28x + 0.07158}{x^3 + 0.8145x^2 - 50.23x + 0.08292}\right)\right]$$

where x has the units of meters.
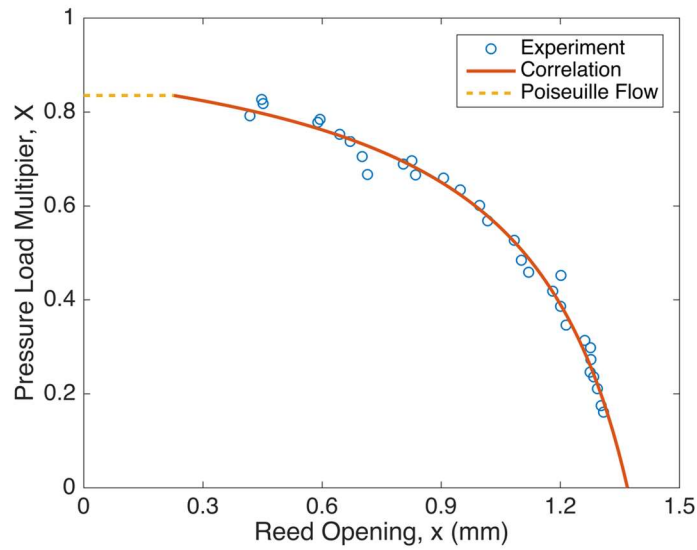
Figure 3.24. Pressure load multiplier as a function of reed tip opening.

Experimental measurements of X suggest there is a maximum reed opening, for which additional pressure differential does not influence the reed position. Since this value of approximately 1.4 mm is less that the maximum opening allowed by the stop of 1.9 mm, the reed never contacts the stop in the experiments. There are many geometric factors that likely have an effect on the pressure load multiplier such as the reed, seat, and valve manifold geometry.

3.8.6   Discharge Coefficient

As discussed previously in Section 3.4, flow rate through the valve is modeled as the sum of orifice flow and the rate of fluid displaced by valve motion. Flow is modeled as quasi-steady so that the steady state orifice equation may be applied. The flow rate dependence discharge coefficient is defined as

$$C_d(Q_o) = \frac{Q_o}{A_o \sqrt{\dfrac{2\Delta P_{up-d}}{\rho}}} \tag{3.84}$$

98

For orifice flow, the characteristic length is chosen to be the hydraulic diameter, D_H, so that the Reynolds number is defined as

$$Re = \frac{\rho V D_H}{\mu} \qquad (3.85)$$

where V is the average fluid velocity. The hydraulic diameter is calculated as $D_H = 4A_o/p_o$ where p_0 is the orifice perimeter, which is calculated for the prototype reed valve as

$$p_o = 2\int_C ds' = 91.2 \text{ mm} \qquad (3.86)$$

The average fluid velocity is calculated as $V = Q_o/A_o$. Therefore, given a hydraulic oil density and dynamic viscosity of 876 kg/m³ and 0.0683 Pa*s respectively, the Reynold number for the prototype reed valve is defined in terms of the orifice flow rate as

$$Re = \left(\frac{4\rho}{p_o\mu}\right)Q_o = \left(1.778 \times 10^{-6} \frac{s}{m^3}\right)Q_o \qquad (3.87)$$

The same experimental data used to calculate the pressure load multiplier was used to calculate the discharge coefficient. The discharge coefficient was calculated according to Equation 3.84 with the orifice area calculated from LTS tip opening measurements using Equation 3.25 where $l_o = 19.4$ mm for the prototype reed valve. The form of the discharge coefficient correlation was taken such that C_d is zero at an orifice flow rate of zero and approaches a finite value as the orifice flow rate approaches infinity (Wu et al. 2002).

$$C_d = C_{d\infty} + Ae^{-B\sqrt{Re}} - (C_{d\infty} + A)e^{-C\sqrt{Re}} \qquad (3.88)$$

The empirical discharge coefficient correlation, shown in Figure 3.25, is

$$C_d(Re) = 0.5740 + 6.144e^{-0.3661\sqrt{Re}} - 6.718e^{-0.3379\sqrt{Re}} \qquad (3.89)$$

Experimental data shows that the discharge coefficient indeed approaches zero as the orifice flow rate approaches zero. The correlation predicts a maximum discharge coefficient of 0.5740.
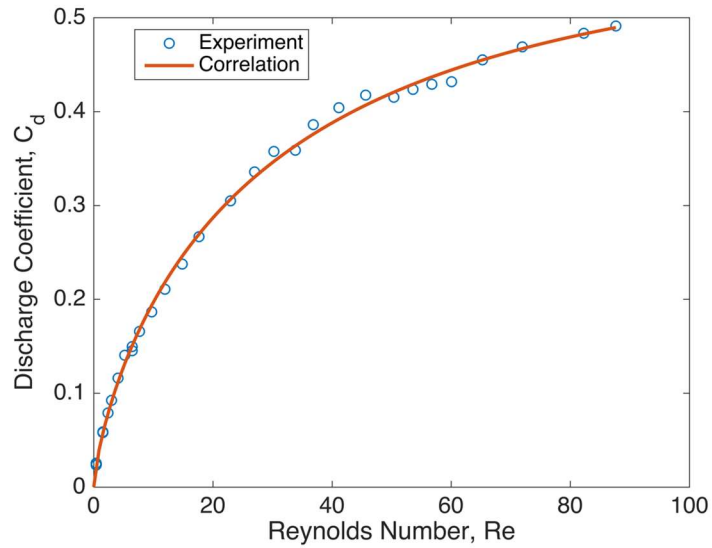
Figure 3.25. Empirical reed valve discharge coefficient correlation

3.8.7   Fluid Displacement Area

Due to the complex geometry or the reed valve, analytical determination of the reed valve fluid displacement area is unclear. Computational fluid dynamics is perhaps the best method of determining the appropriate fluid displacement area as it would be difficult to isolate in experiments. Detailed CFD analysis is required to determine correlations for the fluid displacement area as a function of relevant parameters. With such analysis being outside of the scope of this work, the reed valve fluid displacement area, specifically the fluid displacement area parameters, f_1 and f_2, are left as tuning parameters.

3.8.8   Summary

In this chapter, a computationally inexpensive hydraulic reed valve model was presented. Model parameters were defined and several methods were discussed for determining their values including analytical, computational, and experimental methods. The prototype reed valve was analyzed and its model parameters were determined as summarized in Table 3.13.

Table 3.13. Prototype reed valve parameters.

Parameter	Symbol	Value	Units
Theoretical minimum value of A_Q	A_1	55.1	mm^2
Theoretical maximum value of A_Q	A_2	338.4	mm^2
Combined viscous damping coefficient	c	1650	Pa*s/m
Internal damping coefficient	c_c	77.50	Pa*s/m
Viscous fluid damping coefficient	c_f	1727	Pa*s/m
Reed material elastic modulus	E	2.9	GPa
Nominal reed thickness	h	1.35	mm
Effective reed thickness	h_{eff}	1.161	mm
Reed length	L	25.4	mm
Orifice area per tip opening	l_o	19.4	mm
Fraction of reed length of width W_1	R_1	0.1875	dimensionless
Hydraulic oil temperature	T	22	°C
Width of first reed section	W_1	7.94	mm
Width of second reed section	W_2	15.8	mm
Initial reed deflection – inlet	x_0	0	mm
Initial reed deflection – delivery	x_0	–0.18	mm
Maximum valve opening	x_{stop}	1.9	mm
First mode function parameter	γ_1	1.640	dimensionless
Second mode function parameter	γ_2	0.6986	dimensionless
Third mode function parameter	γ_3	0.8663	dimensionless
Hydrodynamic function	Γ_f	0.8850	dimensionless
Reed stiffness	κ	7.709	MPa/m
Hydraulic oil dynamic viscosity	μ	0.0683	Pa*s
Reed material density	ρ_c	1410	kg/m^3

3.9   Conclusion

In previous literature, reed valves have been modeled using both the finite element method, and one-dimensional analytical methods. In this chapter, a one-dimensional

analytical model was developed for application in hydraulic systems. Unlike the majority of reed valve literature that focuses on applications where air as the primary working fluid, this chapter presented an approach designed for use in hydraulic systems where the fluid density and viscosity may be significant.

A one-dimensional ODE was developed from Euler-Bernoulli beam theory. Valve parameters were identified in order to formulate the equation of motion in accurate and consistent manner. The pressure distribution on the reed, which represents the forcing function, was captured by the pressure load multiplier. Novel analytical, computational, and experimental methods of determining reed valve parameters were presented and analyzed. This chapter contributes to the field of reed valve modeling through the development of simple, accurate, and computationally inexpensive modeling techniques.

Chapter 4 Mass Conservative Piston Pump Model

4.1   Introduction

In Chapter 2 and Chapter 3, dynamic models were developed for disc and reed style hydraulic check valves. These models were designed for implementation in a wide range of hydraulic systems. However, before these models can be used with confidence for design and optimization, they must be validated. This work does not attempt to provide a comprehensive validation across a wide range of systems and conditions. Rather, an experimental validation methodology is presented, including a novel measurement technique. A single cylinder piston pump is chosen as the system in which the disc and reed valve models are validated. Because valve dynamics are so tightly coupled to pump dynamics, the entire pump is modeled rather than using experimental pressure and/or flow rate measurements as check valve model inputs. The purpose of this chapter is to outline the pump model in which the check valve models will be implemented for validation. Note that the pump model is designed to simulate an experimental pump setup that will be presented in Chapter 5.

4.2   Pump Models

4.2.1   Complete Pump Model

In this work, a complete single cylinder pump circuit, shown in Figure 4.1, is modeled using a 0-D lumped parameter approach. In three discrete regions – the tank, pump cylinder, and load line – the pressure is assumed to be spatially uniform. The corresponding locations where the fluid pressure is assumed to change instantaneously are the inlet and delivery check valves and the variable orifice.
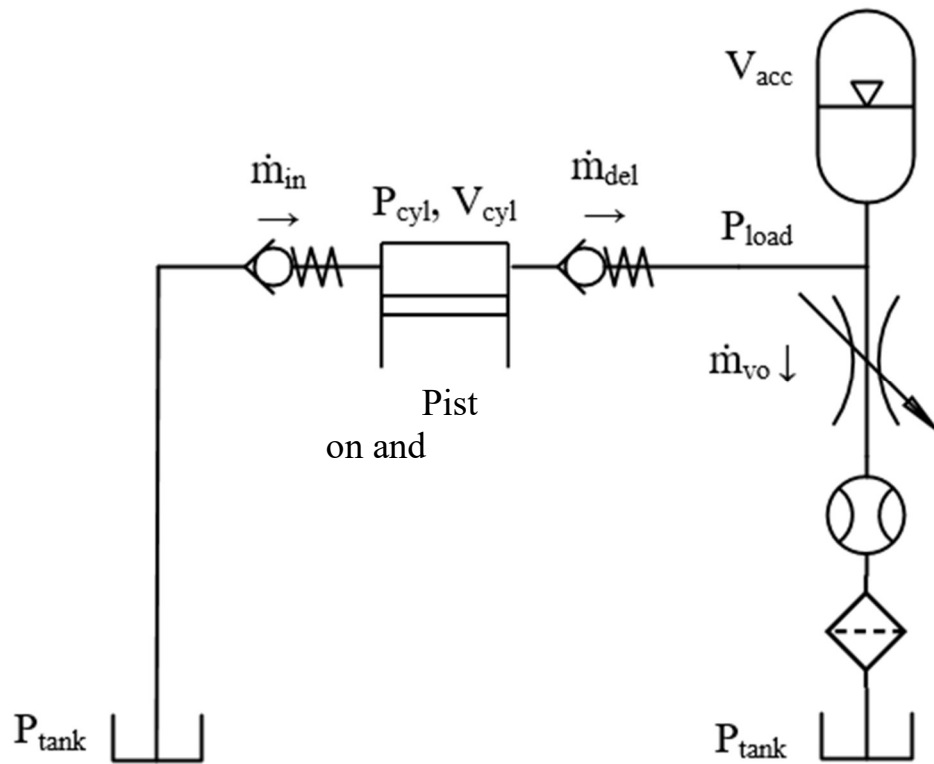
Figure 4.1. Complete pump circuit schematic

As discussed in Chapter 2 and Chapter 3, check valve motion is calculated from two first-order ODEs per valve for a total of four ODEs in a single cylinder pump. Two additional first-order ODEs are necessary to describe the mass flow rate through the cylinder and the accumulator volume. Thus a total of six first-order ODEs must be solved for the complete pump model.

4.2.2   Simplified Pump Model

If the accumulator is able to sufficiently smooth out load pressure variations, the load pressure may be approximated as constant, simplifying the pump model. The simplified pump circuit is shown in Figure 4.2. A constant load pressure approximation allows the accumulator, needle valve, flow meter, and filter to be removed from the model. Removing the accumulator reduce the number of ODEs from six to five. The simplification

also eliminates the need to correctly estimate the accumulator and load line initial conditions or simulate a large number of cycles to charge the accumulator and reach cyclic steady state. The constant load pressure simplified pump model was implemented in this work. Details on implementing the complete pump model can be found in prior work by the author (Knutson & Van de Ven 2016b).
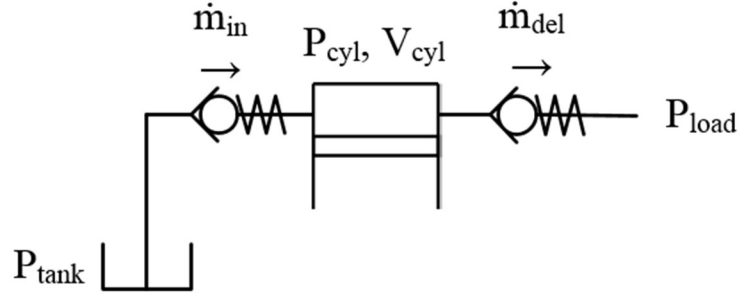
Figure 4.2. Constant load pressure simplified pump model.

4.3   Model Description

4.3.1   Kinematic Linkage

The piston is driven by a 4-bar crank-slider mechanism with a crank radius of r and connecting rod length of l as shown in Figure 4.3. The angle of the crank from its position at top dead center (TDC) is θ. Geometric analysis of Figure 4.3 reveals displacement of the piston from top dead center, assuming rigid links, is described by the following expression:

$$x_p = r(1 - \cos\theta) + l - \sqrt{l^2 - r^2 sin^2\theta} \qquad (4.1)$$

Instantaneous cylinder volume, V_{cyl}, is the sum of the cylinder volume at top dead center, V_{tdc}, and the volume swept by the piston, which is the product of the piston area, A_p, and displacement:

106

$$V_{cyl} = V_{tdc} + A_p \left[r(1 - \cos\theta) + l - \sqrt{l^2 - r^2 sin^2\theta} \right] \tag{4.2}$$
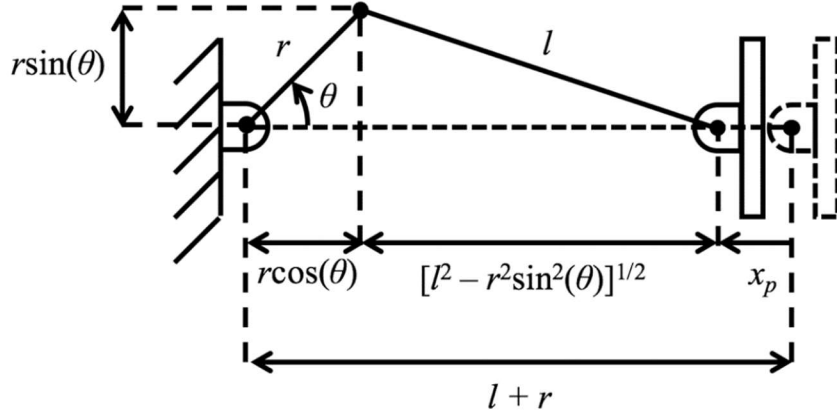
Figure 4.3. Crank-slider linkage geometry

4.3.2   Valve Mass Flow Rate

Flow rate through both the disc and reed valve model was calculated as the sum of the orifice flow rate through the valve and the rate of fluid displacement caused by the disc displacement. To track mass flow into and out of the cylinder, the volumetric flow rate is multiplied by the fluid density. Therefore, the mass flow rate through the inlet valve, $\dot{m}_{in}$, is

$$\dot{m}_{in} = C_d A_o \sqrt{2\rho |P_{tank} - P_{cyl}|} \, sign(P_{tank} - P_{cyl}) + \rho A_Q \dot{x}_{in} \tag{4.3}$$

Similarly, the mass flow rate through the delivery valve, $\dot{m}_{del}$, is

$$\dot{m}_{del} = C_d A_o \sqrt{2\rho |P_{cyl} - P_{load}|} \, sign(P_{cyl} - P_{load}) + \rho A_Q \dot{x}_{del} \tag{4.4}$$

4.3.3   Cylinder Pressure

The mass of fluid in the cylinder is described by the following ordinary differential equation:

$$\frac{dm_{cyl}}{dt} = \dot{m}_{in} - \dot{m}_{del} - \dot{m}_{leak} \qquad (4.5)$$

where $\dot{m}_{leak}$ is the leakage between the piston and cylinder. In this work leakage is assumed to be negligible.

The mass in the cylinder can be calculated by numerically integrating Equation 4.5. Fluid density may then be determined from Equation 4.2 and 4.5 as

$$\rho_{cyl} = \frac{m_{cyl}}{V_{cyl}} \qquad (4.6)$$

Finally, the cylinder pressure must be determined. In practice, a small amount of air is entrained in oil so that the fluid is a liquid-gas mixture. Several compressibility models have been developed relating the pressure and density of hydraulic oil with entrained air (Jinghong et al. 1994; Cho et al. 2002). In this work, the model developed by Cho et al. was used (Cho et al. 2002).

4.3.4   Density of Oil with Entrained Air

To develop an analytical expression relating pressure and fluid density, the following assumptions will be employed (Cho et al. 2002):

1. The air content is constant
2. The solubility of the air is very low and almost constant
3. The bulk modulus of pure oil is constant
4. The system pressure is significantly lower than the bulk modulus of pure oil
5. The mass of mixed air is negligible compared to that of oil.

In subsequent analysis, nomenclature defined in Table 4.1 and subscripts defined in Table 4.2 will be used.

Table 4.1. Nomenclature

Parameter	Symbol	Units
Pressure	P	Pa
Volume fraction of air at 1 atmosphere	R	dimensionless
Volume	V	m^3
Bulk modulus of air free oil	β	Pa
Ratio of specific heats of air	γ	dimensionless
Density	ρ	kg/m^3

Table 4.2. Subscripts

Indication	Subscript
Quantity at pressure	*none*
Quantity at atmospheric pressure	*0*
Air	*a*
Fluid	*f*

From mass conservation, density of the mixture can be expressed in terms of volume as

$$\frac{\rho}{\rho_0} = \frac{V_0}{V} = \frac{V_{a0} + V_{f0}}{V_a + V_f} = \frac{\left(\frac{V_{a0} + V_{f0}}{V_{f0}}\right)}{\left(\frac{V}{V_{f0}}\right)} \tag{4.7}$$

From the definition of R,

$$\frac{V_{a0} + V_{f0}}{V_{f0}} = \frac{1}{1 - R} \tag{4.8}$$

The mixture volume is related to the fluid volume at atmospheric pressure by (Cho et al. 2002)

$$\frac{V}{Vf_0} = \left(\frac{P_0}{P}\right)^{1/\gamma} R + e^{-\frac{P-P_0}{\beta}} \tag{4.9}$$

Combining Equation 4.7, 4.8, and 4.9 yields the following relationship between density and pressure:

$$\frac{\rho}{\rho_0} = \frac{1}{(1-R)R\left(\frac{P_0}{P}\right)^{1/\gamma} + (1-R)e^{\frac{P_0-P}{\beta}}} \tag{4.10}$$

If $R << 1$ then $R^2 \approx 0$ such that

$$\frac{\rho}{\rho_0} \cong \frac{1}{R\left(\frac{P_0}{P}\right)^{1/\gamma} + (1-R)e^{\frac{P_0-P}{\beta}}} \tag{4.11}$$

Although density can be readily calculated from pressure with Equation 4.11, the author is unaware of a method to explicitly solve for pressure as a function of density.

4.3.5   Orifice Equation Density

One of the assumptions used to derive the steady state orifice equation is constant fluid density. In hydraulic applications, especially those at high pressures and with a high air content in oil, density is not constant. The orifice equation could be corrected for density variations, however, in this work the discharge coefficient was experimentally determined at relatively low pressures where density is approximately constant. Therefore, in the pumping model, it is not clear what density should be used. Noting that hydraulic oil is

quite stiff, for small pressure drops, it is reasonable to simply use the density of oil in the cylinder. That is, $\rho = \rho(P_{cyl})$. For large pressure drops, an averaged density could be used instead. For the inlet valve, the density used in Equation 4.3 would be $\rho = \frac{1}{2}[\rho(P_{cyl}) + \rho(P_{tank})]$. Similarly, for the delivery valve, the density used in Equation 4.4 would be $\rho = \frac{1}{2}[\rho(P_{cyl}) + \rho(P_{load})]$. It's not clear which approach is more appropriate as both are estimates that lack a theoretical underpinning. Nonetheless, pressure drop across the check valves is expected to be quite small most of the time and since density changes little with pressure, the results are insensitive to the chosen density. For experimental validation, the disc valve model used the averaged density while the reed valve model used a density evaluated at cylinder pressure.

4.3.6 Calculating Pressure from Density

To solve for pressure as a function of density the iterative Newton-Raphson method was employed. First, Equation 4.11 was rewritten as

$$RP_0^{1/\gamma}P^{-1/\gamma} + (1-R)e^{\frac{P_0}{\beta}}e^{-\frac{1}{\beta}P} = \frac{\rho_0}{\rho} \tag{4.12}$$

Equation 4.12 has the form

$$AP^B + Ce^{DP} = E \tag{4.13}$$

where A, B, C, D, and E are known constants. Therefore, the function we seek the root of is

$$f = AP^B + Ce^{DP} - E \tag{4.14}$$

For the Newton-Raphson method, knowledge of $\frac{\partial f}{\partial P}$ is required. From Equation 4.14

111

$$\frac{\partial f}{\partial P} = ABP^{B-1} + CDe^{DP} \tag{4.15}$$

Successive estimates of pressure are then found by iteration as follows:

$$P^{n+1} = P^n - \frac{f^n}{\left(\frac{\partial f}{\partial P}\right)^n} \tag{4.16}$$

Figure 4.4 shows pressure as a function of density for an air-oil mixture. Figure 4.5 shows the number of iterations required for convergence as a function of density and tolerance. In the pump model, a tolerance of 1×10^{-6} was chosen to provide an accurate estimate of pressure.
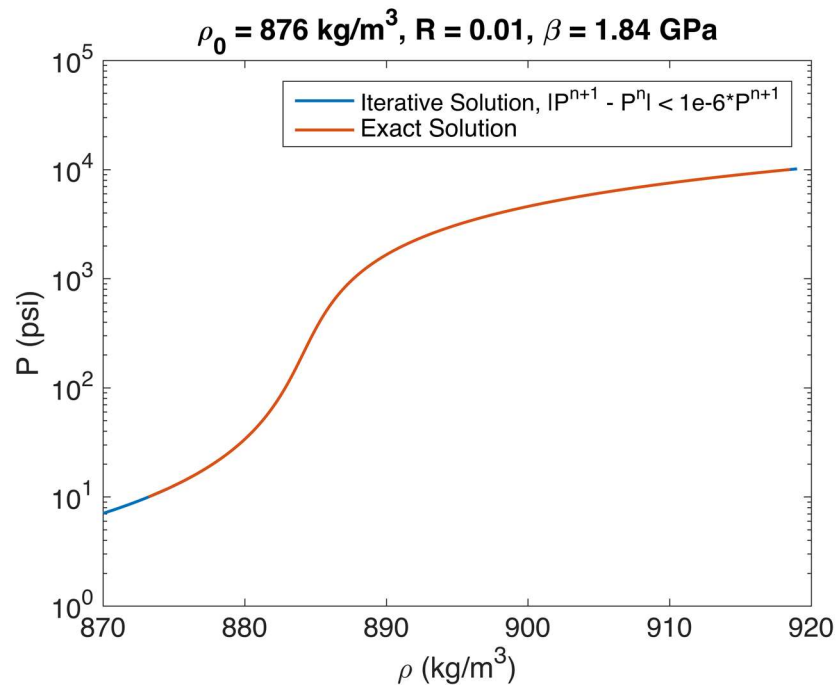
Figure 4.4. Air-oil mixture pressure as a function of density
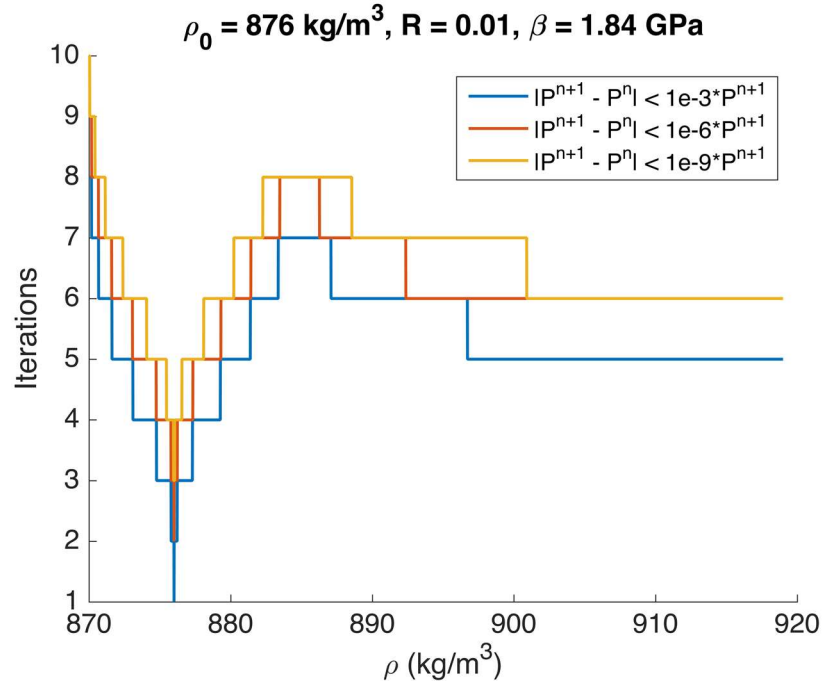
Figure 4.5. Effect of convergence tolerance on computational expense

4.3.7 Iteration Scheme

The scheme used to march the pump model forward in time is outlined in the following steps:

1. Calculate $\dot{m}_{in}{}^n$ and $\dot{m}_{del}{}^n$ from Equation 4.3 and 4.4 using data from time n–1
2. Calculate $(dm_{cyl}/dt)^n$ from Equation 4.5
3. Numerically integrate $(dm_{cyl}/dt)^n$ to obtain $m_{cyl}{}^n$
4. Calculate $V_{cyl}{}^n$ from Equation 4.2
5. Calculate $\rho_{cyl}{}^n$ from Equation 4.11
6. Calculate $P_{cyl}{}^n$ from Equation 4.16
7. Calculate valve dynamics at time n
8. Calculate $\dot{m}_{in}{}^{n+1}$ and $\dot{m}_{del}{}^{n+1}$

4.3.8 Pump Delivery Calculation

Pump delivery, V_{del}, defined as the volume of fluid pumped per revolution, is an important pump performance metric and therefore must be modeled. The choice of where in the circuit the flow rate is measured affects the pump delivery volume as pressure variations cause density variations. In the experiment described in this thesis, the pump delivery was measured at atmospheric pressure. If the sampling period, T, is equal to the time per revolutions, $2\pi/\omega$, then the pump delivery can be calculated as

$$V_{del} = \frac{1}{T} \int_0^T \frac{\dot{m}_{del}}{\rho_0} dt \tag{4.17}$$

4.4   Summary

In this chapter, two mass conservative pump models are introduced: one with a needle valve to provide a load and an accumulator to smooth out pressure ripple, and one with a constant load pressure. The latter was chosen for its computational speed and ability to well approximate the former. Pump modeling was then described in detail including a kinematic linkage model, valve mass flow rate model, cylinder pressure model, and air-oil compressibility model. The model presented in this section was developed with experimental validation of check valves in mind. Given that the pump model is mass conservative and accounts for density variations, a definition of volumetric efficiency is presented that yields itself to direct comparison with experimental flow rate data taken at atmospheric pressure.

Chapter 5 Experimental Validation

5.1   Background

Two sets of pumping experiments were performed – one with commercially available disc style check valves and the other with custom reed valves build for this thesis project. In this chapter, the experimental setup will be described and the results will be compared to results from the mathematical model to give objective evidence of model validity. In this work, validation is not treated as a binary metric. Experimental results will provide insight into which aspects of the model have predictive value and how the model can be correctly used. Given the nature of a model designed to be computationally inexpensive with many simplifying assumptions, care must be taken to understand the limitations.

Often in modeling, not every parameter can readily be determined analytically. Experimental data can be used to guide a semi-empirical determination of such parameters, or the parameters can be tuned without regard to their physical or mathematical interpretation in order to make models match experimental results. Clearly, the former is a more rigorous approach and has more predictive value. The distinction may not always be clear so care must be taken to avoid reverting to the latter. A good measure of the quality of a tuned parameter is its applicability to a wide range of model inputs and operating conditions. A tuning parameter that is defined and applied on a physical basis with a semi-empirical approach and performs well across a wide range of operating conditions is a useful in model development. However, a tuning parameter that is simply added to make a model agree with experimental data may cancel out fundamental errors in the model while lacking general applicability and physical justification. As such, results should be interpreted accordingly and the limitations acknowledged and understood.

5.2   Overview

The check valve model will be validated on the basis of two metrics: check valve position and pump delivery. The purpose of this chapter is twofold. First is to provide evidence that the valve models presented in this work have predictive value. Second is to provide an *in situ* model validation approach for hydraulic check valves.

A schematic of the instrumented piston pump circuit is shown in Figure 5.1. The circuit parameters used in the model and experimental setup are given in Table 5.1. The setup is capable of directly measuring cylinder and load pressure, piston position, return flow rate, and check valve position. All other quantities must be inferred from known quantities. In this work, the primary quantities of interest are the valve position and volumetric efficiency, which can be directly measured. As such, validation will focus on characterizing the ability of the check valve models to predict these quantities.
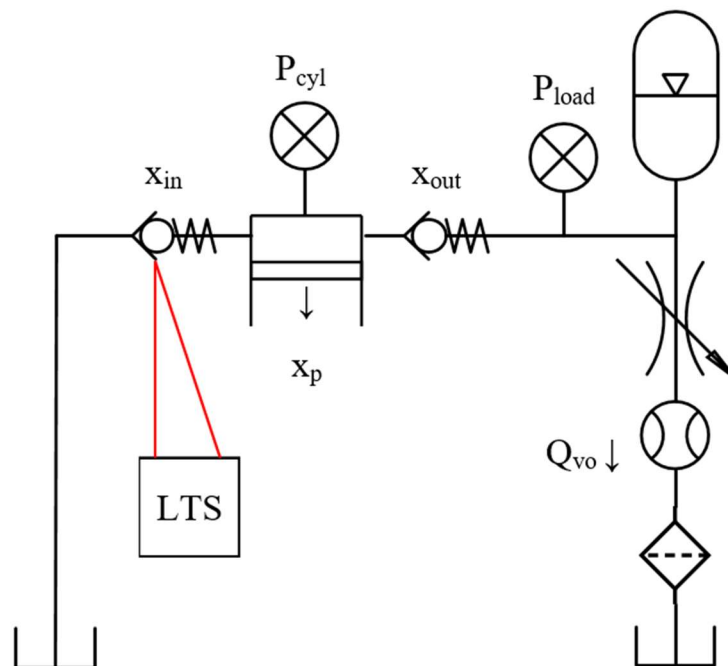

Figure 5.1. Instrumented experimental setup schematic

Table 5.1. Pump experimental parameters.

Parameter	Symbol	Units	Value
Piston diameter	d_{piston}	mm	15.88
Connecting rod length	l	mm	86
Atmospheric pressure	P_o	kPa	101.325
Tank pressure	P_{tank}	kPa	101.325
Crank radius	r	mm	5.6
Pump displacement	V	cc/rev	2.22
Cylinder volume at top dead center	V_{tdc}	m^3	2.17×10^{-5}
Bulk modulus of air free oil at P_o	β	GPa	1.84
Ratio of specific heats for air/nitrogen	γ	ratio	1.4
Hydraulic oil dynamic viscosity	μ	Pa*s	0.0683
Hydraulic oil density at P_o	ρ_0	kg/m^3	876

5.3 Position Measurement Through Multiple Interfaces

5.3.1 Laser Triangulation Sensor Measurement Technique

To experimentally validate the model, the position of the check valve disc was optically measured with a laser triangulation sensor (LTS). A method for measuring liquid film thickness through quartz using a laser triangulation sensor (Peterson & Peterson 2006) was modified for measuring the check valve disc position in hydraulic oil through acrylic (PMMA). The sensor output voltage, ΔV, is converted to the apparent change in position, x_{app}, using an apparent scale factor, C_{app}, which is specified by the manufacturer for measurements taken in air. Refraction of the laser light at the air-acrylic and acrylic-oil interfaces changes the scale factor and introduces nonlinearity (Yudell & Van de Ven 2015). The actual scale factor, C_{act}, can be estimated experimentally by measuring the change in output voltage, given a known actual change in position, x_{act}. While this method is simple, its use is limited to the experimental setup. To avoid this limitation, a method to analytically calculate the actual scale factor was developed. Figure 5.2 shows a laser

triangulation sensor measuring a change in position through an acrylic sight glass and hydraulic oil.
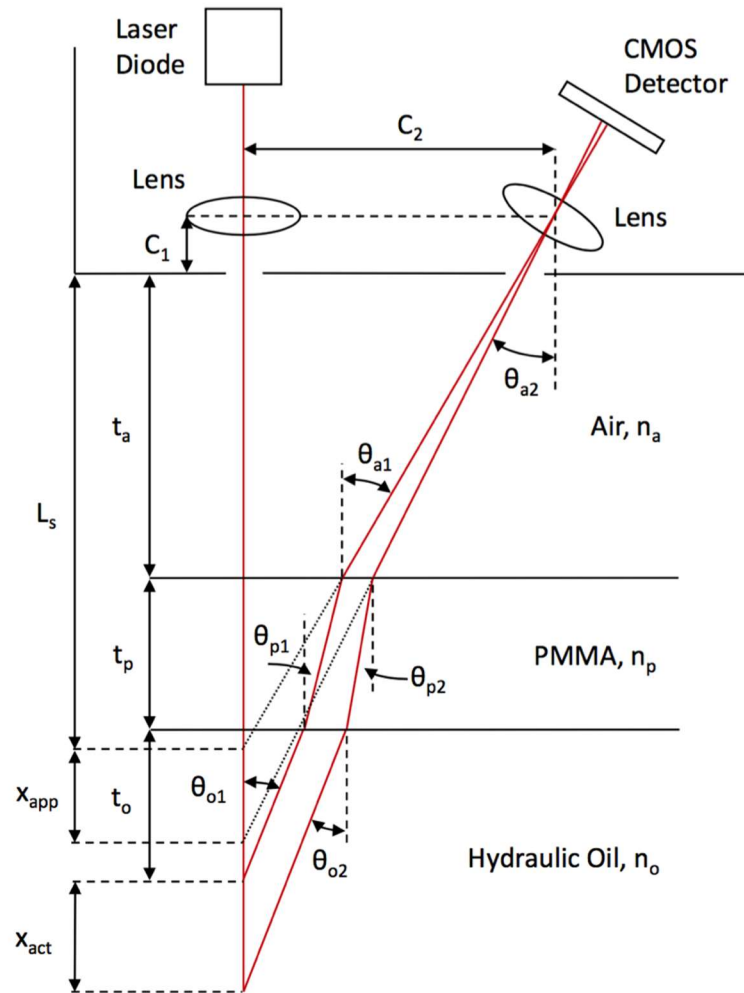
Figure 5.2. Laser triangulation sensor position measurement

The variables C_1, C_2, L_s, t_a, t_p, n_a, n_p, and n_o, were measured and the actual change in position was chosen as an input, leaving nine unknown variables – six laser angles, θ, oil gap thickness, t_o, apparent change in position, and the sensor output voltage. Details on measurement of refractive indices, n_p and n_o, can be found in Appendix B. Nine equations are required to solve for the output voltage given the actual change in position. Snell's law provides four equations:

$$\frac{n_a}{n_p} = \frac{\sin\theta_{p1}}{\sin\theta_{a1}} \tag{5.1}$$

$$\frac{n_p}{n_o} = \frac{\sin\theta_{o1}}{\sin\theta_{p1}} \tag{5.2}$$

$$\frac{n_a}{n_p} = \frac{\sin\theta_{p2}}{\sin\theta_{a2}} \tag{5.3}$$

$$\frac{n_p}{n_o} = \frac{\sin\theta_{o2}}{\sin\theta_{p2}} \tag{5.4}$$

An additional four equations can be derived from the geometry of the experimental setup:

$$\tan\theta_{a1} = \frac{C_2}{C_1 + L_s} \tag{5.5}$$

$$(C_1 + t_a)\tan\theta_{a1} + t_p\tan\theta_{p1} + t_o\tan\theta_{o1} = C_2 \tag{5.6}$$

$$(C_1 + t_a)\tan\theta_{a2} + t_p\tan\theta_{p2} + (t_o + x_{act})\tan\theta_{o2} = C_2 \tag{5.7}$$

$$x_{app} = C_2\left(\frac{1}{\tan\theta_{a2}} - \frac{1}{\tan\theta_{a1}}\right) \tag{5.8}$$

Lastly, by definition the apparent scale factor is related to the apparent change in position by

$$C_{app} = \frac{x_{app}}{\Delta V} \tag{5.9}$$

Rather than seek an analytical solution for the actual change in position as a function of the sensor output voltage, Equations 5.1 through 5.9 were solved numerically

119

for 11 discrete values of the actual change in position between 0 and 1.2 mm. The resulting relationship was found to be highly linear so the actual scale factor was as the slope of a least squares linear fit. From the actual scale factors, the position of the disc can be calculated from LTS voltage data as

$$x_{act} = C_{act}\Delta V \qquad (5.10)$$

5.3.2   Scale Factor Calculation

5.3.2.1 Disc Valve Manifold

The input parameters that define the LTS measurements of the disc valve are given in Table 5.2. The actual scale factors calculated for inlet and delivery valves were 3.751 mm/V and 3.740 mm/V respectively as shown in Figure 5.3 and Figure 5.4.

Table 5.2. Laser triangulation sensor position measurement input parameters – disc valve

| Parameter	Symbol	Units	Value
Apparent analog out scale factor	C_{app}	mm/V	2.50 ± 0.00
LTS geometric constant	C_1	mm	8.35 ± 0.10
LTS geometric constant	C_2	mm	44.06 ± 0.10
Standoff length	L_s	mm	120.00 ± 0.00
Refractive index of air	n_a	ratio	1.000 ± 0.000
Refractive index of hydraulic oil	n_o	ratio	1.476 ± 0.016
Refractive index of PMMA	n_p	ratio	1.509 ± 0.025
Thickness of air gap – inlet valve	t_a	mm	90.67 ± 0.10
Thickness of PMMA window – inlet valve	t_p	mm	12.14 ± 0.05
Thickness of air gap – delivery valve	t_a	mm	84.10 ± 0.10
Thickness of PMMA window – delivery valve	t_p	mm	11.84 ± 0.05
Actual change in position	x_{act}	mm	$(0.00 - 1.20) \pm 0.00$
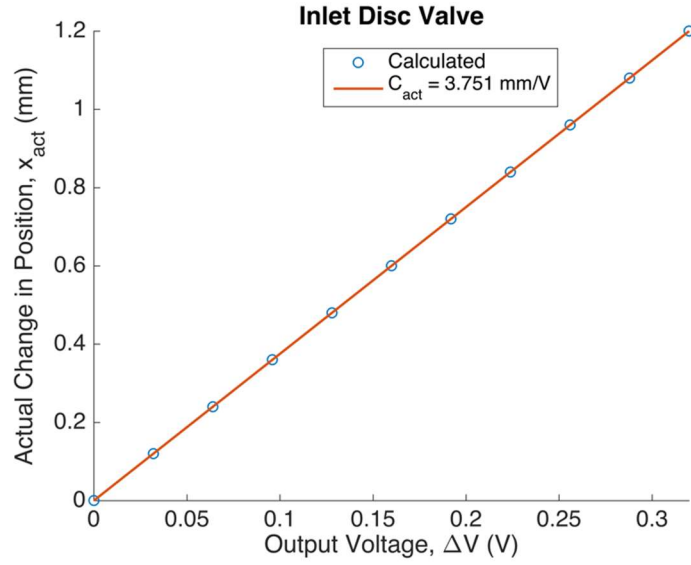
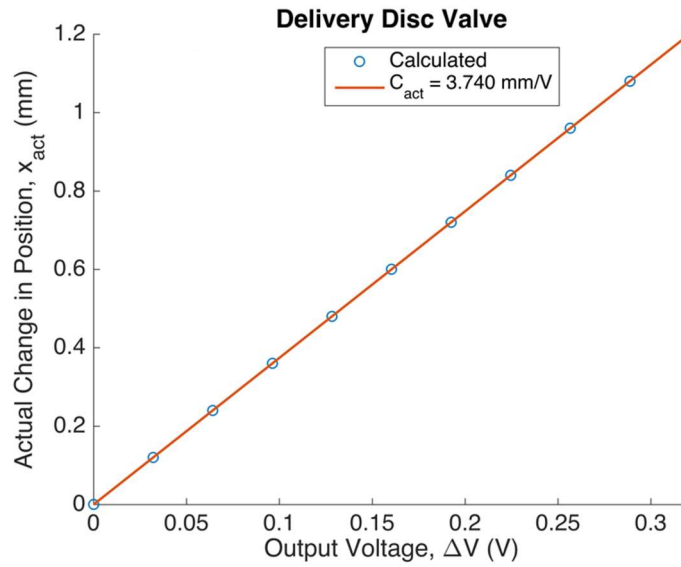Figure 5.3. Inlet valve actual scale factor

Figure 5.4. Delivery valve actual scale factor

In this work, uncertainty in a quantity f, which is a function of variables $x_1,\ldots,x_n$ is calculated as follows:

$$\Delta f(x_1, \ldots, x_n) = \sum_{i=1}^{n} |f(x_1, \ldots, x_i + \Delta x_i, \ldots, x_n) - f(x_1, \ldots, x_n)| \qquad (5.11)$$

Inputting the data from Table 5.2 into Equation (5.11, the uncertainty in the actual scale factor for the inlet and delivery disc valve manifold was calculated to be ±1.120% and ±1.111% respectively. Since the uncertainty in the voltage measurement is significantly smaller than the uncertainty in the actual scale factors, the uncertainty of the position measurement as calculated from Equation 5.11 is approximately equal to that of the actual scale factors. The slight difference in actual scale factor between the inlet and delivery valve manifold is due to the difference in thickness of the air gap, sight glass, and oil.

5.3.2.2 Reed Valve Manifold

Using the same approach as for the disc valve manifolds, the actual scale factor for both the inlet and delivery reed valve manifold was calculated to be 3.746 mm/V. The LTS measurement system and experimental setup geometry were nearly identical to that used in the disc valve experiments. As a result, the uncertainty is expected to be approximately the same. Therefore, the uncertainty in position measurements of the LTS was estimated to be ±1.12%.

5.4   Disc Valve

5.4.1   Experimental Setup

To validate the check valve model, experiments are performed using a single cylinder crank-slider piston pump shown in Figure 5.5. The pump crankshaft is driven by an electric motor controlled by a variable frequency drive (VFD). Piston position is measured using a linear variable differential transformer (LVDT) displacement transducer attached directly to the piston. Both the inlet and delivery valve manifolds have acrylic covers to allow a laser triangulation sensor (LTS) to measure the position of the valve discs as shown in Figure 5.6.
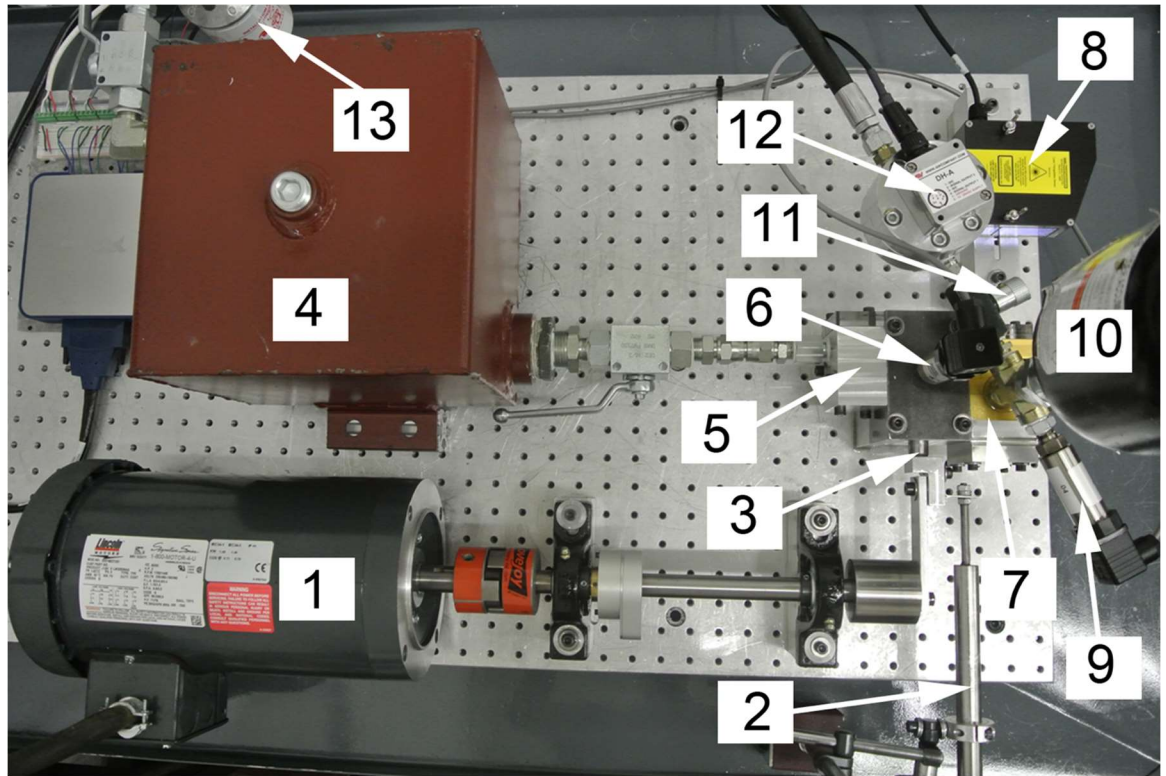
Figure 5.5. Instrumented experimental setup consisting of a 1. Motor 2. Piston 3. LVDT 4. Tank 5. Inlet check valve 6. Cylinder pressure transducer 7. Delivery check valve 8. LTS 9. Load pressure transducer 10. Accumulator 11. Variable orifice (VO) needle valve 12. Gear flow meter and 13. Filter
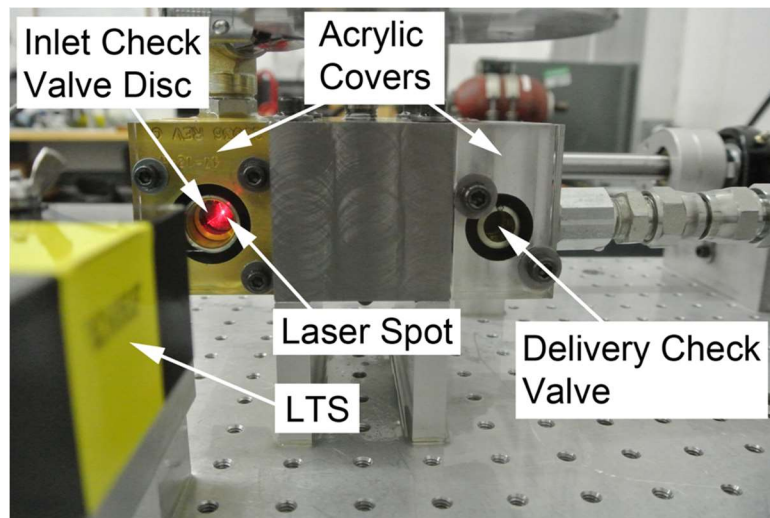

Figure 5.6. Valve position measurement with a LTS

Cylinder and load pressure were measured with Silicon-on-Sapphire pressure transducers with a response time of 0.2 ms. A positive displacement gear flow meter measured the average volumetric flow rate downstream of the variable orifice needle valve. All measurements were taken at a sampling frequency of 10 kHz.

5.4.2 Experimental Methods

Three experimental conditions were used to validate the disc valve model, as summarized in Table 5.3. For each condition, two experiments were run – one measuring the inlet check valve position and one measuring the same for the delivery. Thus a total of six experiments were conducted. The ranges in load pressure and pump speed are a result of the accumulator and discharging and the crankshaft accelerating and decelerating due to the single cylinder pump. The mean load pressure varied slightly between inlet and delivery valve experiments due to a lack of fine control of the needle valve used to set pressure. Conversely, the speed was quite constant due to fine control of the variable frequency drive.

Table 5.3. Disc valve pump experiment conditions

Condition	Pump Speed (rpm)	Mean load pressure (MPa)
Baseline	593	2.76 – 2.79
High Speed	734	2.75 – 2.81
High Pressure	591	3.67 – 3.78

Experiments were performed by first setting the motor speed using the variable frequency drive. Next, the load pressure was set by adjusting the needle valve and allowing the pump to run until the load pressure reached cyclic steady state. Data was collected for a period of five seconds. During post processing, the timing of top dead center, which was used to align model and experimental results, was determined from LVDT piston position data.

Due to the short duration of the experiments and low flow rate relative to the tank volume, the effects of the fluid temperature were not considered. The duration of each

experiment was approximately 1-2 minutes, with sufficient time between experiments to prevent a rise in temperature. Therefore, oil properties were selected at room temperature and the instrumentation did not require any temperature corrections to their calibration. No leakage was observed during experiments.

5.4.3   Valve Opening Results

The goal of measuring valve position during operation is to understand its behavior and major features and examine the extent to which the model captures these details. Therefore, validation of position data is left qualitative while pump displacement is chosen as a qualitative measure of model performance. Figure 5.7 through Figure 5.9 shows the modeled and experimental inlet disc valve position over three pumping cycles for the conditions given in Table 5.3. Similarly, delivery valve position is shown in Figure 5.10 through Figure 5.12. Note that time = 0 corresponds to top dead center.
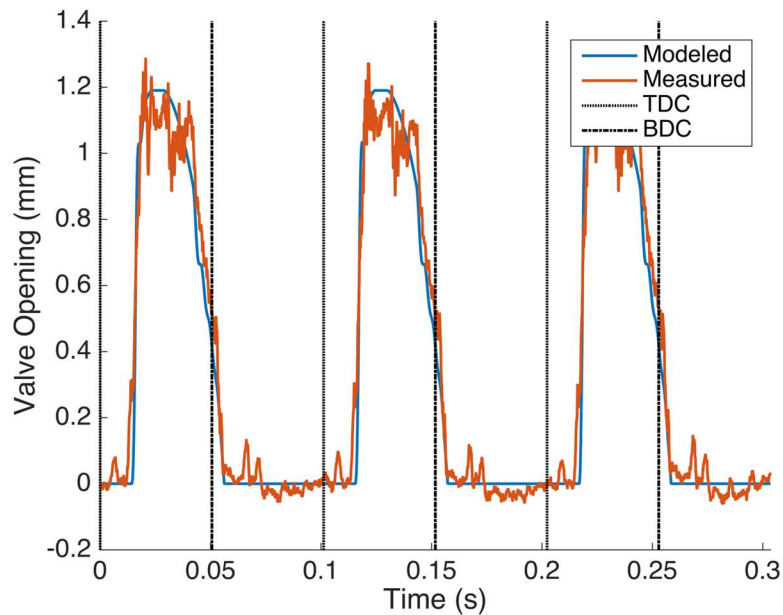
Figure 5.7. Inlet disc valve position – baseline case
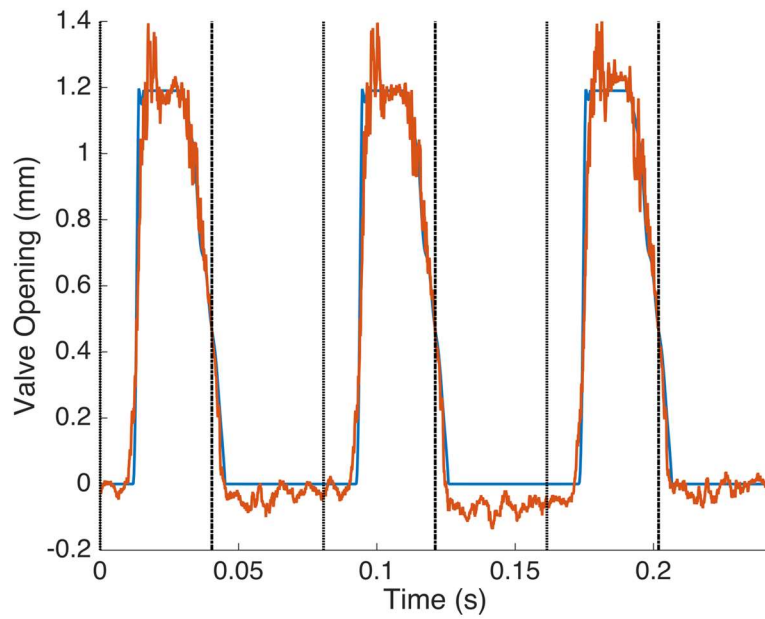
Figure 5.8. Inlet disc valve position – high speed case
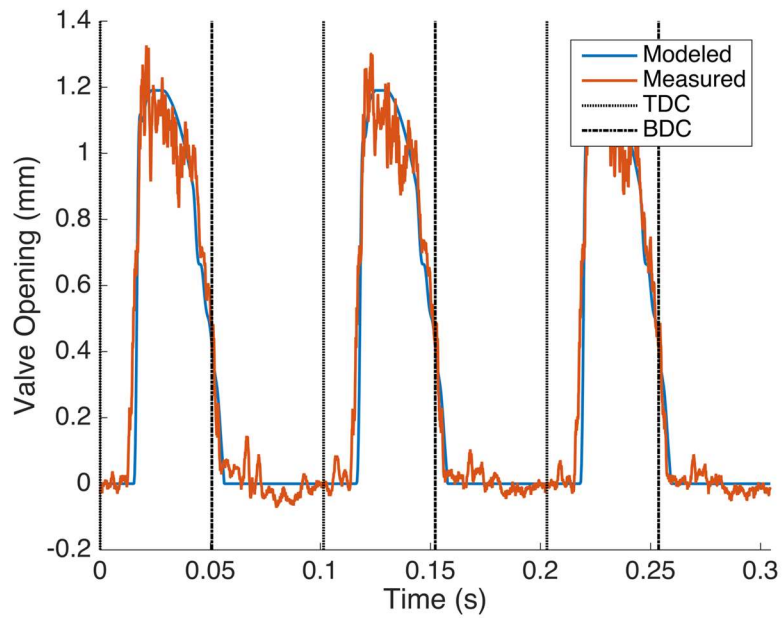
Figure 5.9. Inlet disc valve position – high pressure case.

126
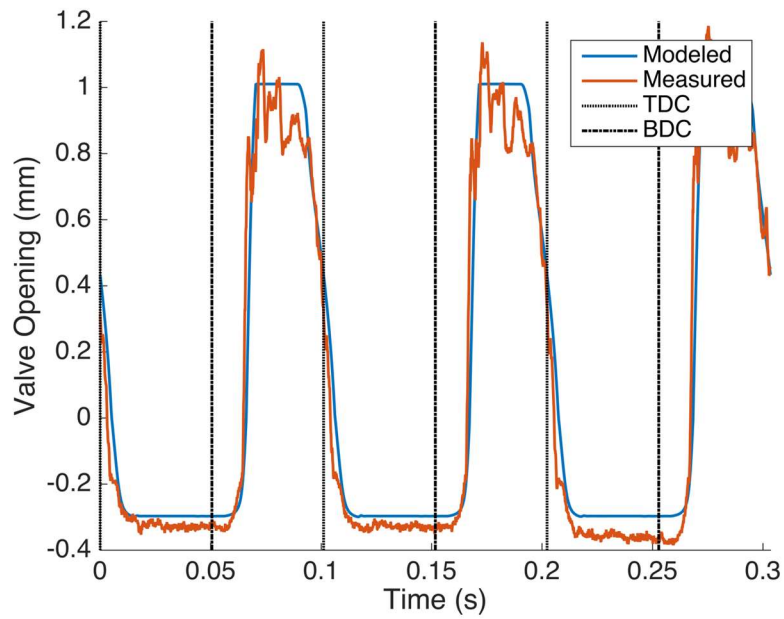
Figure 5.10. Delivery disc valve position – baseline case.
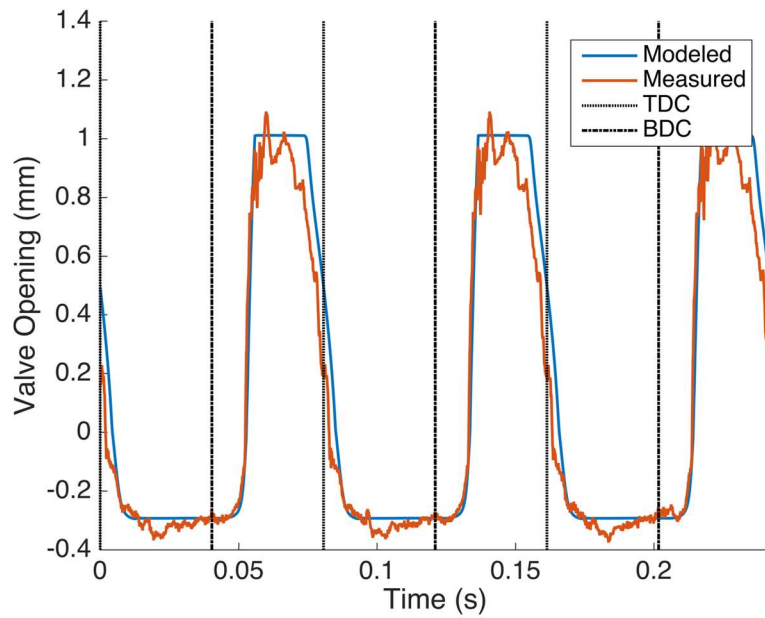
Figure 5.11. Delivery disc valve position – high speed case.
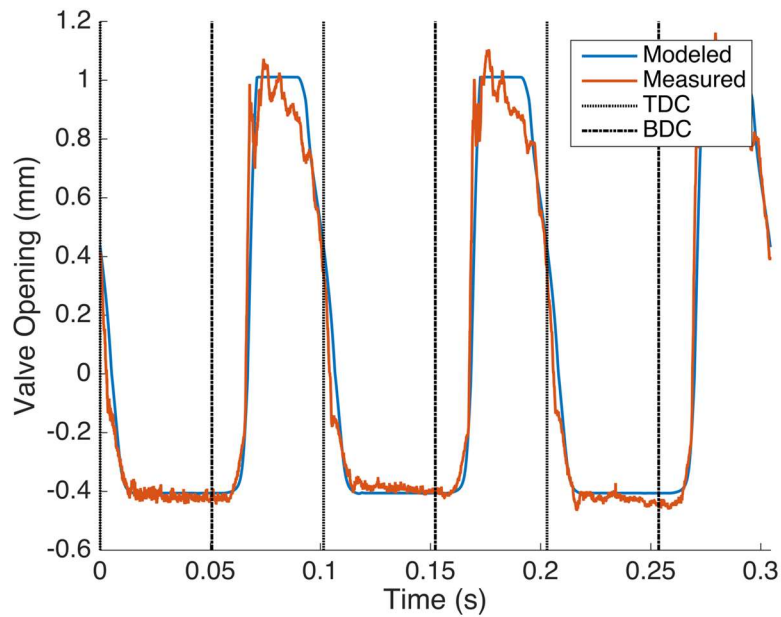
Figure 5.12. Delivery disc valve position – high pressure case.

5.4.4   Pump Delivery Results

Recall that pump delivery is defined as the net volume of fluid pumped per revolution measured at atmospheric pressure. Several factors affect pump delivery, including pump geometry, fluid compressibility, cylinder volume, dead volume, and check valve behavior. Back flow reduces pump delivery and represents a volumetric efficiency loss. Since check valve behavior has a significant effect on back flow, pump delivery is an informative and convenient quantitative measure by which check valve model performance may be assessed. Table 5.4 summarizes the measured and modeled disc valve pump delivery for the three conditions listed in Table 5.3. During one revolution, the piston sweeps a volume of $2A_p r$, which represents the maximum theoretical pump delivery. For reference, the pump described in this work has a piston swept volume of 2.22 cc/rev.

Table 5.4. Disc valve pump delivery (cc/rev) – measured and modeled.

Experiment Conditions	Air Content, R	Inlet Disc Valve Measured		
		Measured	Modeled	% Error
Baseline, 593 rpm, 2.76 MPa	0.013	1.720	1.731	+0.640
High speed, 743 rpm, 2.81 MPa	0.013	1.684	1.716	+1.900
High pressure, 591 rpm, 3.67 MPa	0.013	1.713	1.697	–0.934
Experiment Conditions	Air Content, R	Delivery Disc Valve Measured		
		Measured	Modeled	% Error
Baseline, 593 rpm, 2.79 MPa	0.013	1.790	1.730	–3.3352
High speed, 743 rpm, 2.75 MPa	0.013	1.678	1.717	+2.324
High pressure, 591 rpm, 3.78 MPa	0.013	1.616	1.693	+4.765

The three operating conditions were approximately the same for experiments where inlet valve position was measured as the delivery valve case. Therefore, the measured delivery should be approximately the equal for corresponding experiments. However, as can be seen in Table 5.4, the measured pump delivery varied by up to nearly 6%. The reason for the large variance is a failure to identify cyclical steady state accurately. If the accumulator is still charging, even very slowly, the measured pump delivery will be decreased. This was almost certainly the case for the high pressure case when the delivery valve was measured.

5.4.5 Discussion

A striking difference between the inlet and delivery check valve position measurements is the relatively large negative position of the delivery valve. After conducting experiments, it was discovered that the delivery check valve housing was not fully seated in the manifold. As a result, the O-ring acted as a relatively compliant spring, allowing the entire disc valve housing to be displaced as the O-ring compressed during large negative pressure differentials. There was no evidence of leaking or that check valve performance was adversely affected because the valve wasn't fully seated. This effect was accounted for with a modified seat stiffness as discussed in Section 2.4.3.2.

A distinct feature of the experimental disc position measurements was oscillations that occurred when the valve was open. High speed video taken of the valves during pumping showed the disc wobbling after opening. At the instants shown, the disc is untilted in Figure 5.13a and tilted in Figure 5.13b. A uniform shadow around the circumference of the disc indicates the disc is normal to the camera and therefore untilted. The source of this wobble is believed to be an imbalance of forces created by the fluid exiting the manifold to one side. This behavior has a couple of notable effects on the results. First, when the disc is wobbling, the edge of the disc bounces off the stop preventing the disc from fully opening. Second, when the pressure differential across the disc becomes negative and the valve begins the close, if the disc is tilted or bouncing off the stop, its center of mass is nearer to the seat, causing it to close faster than a fully open valve.
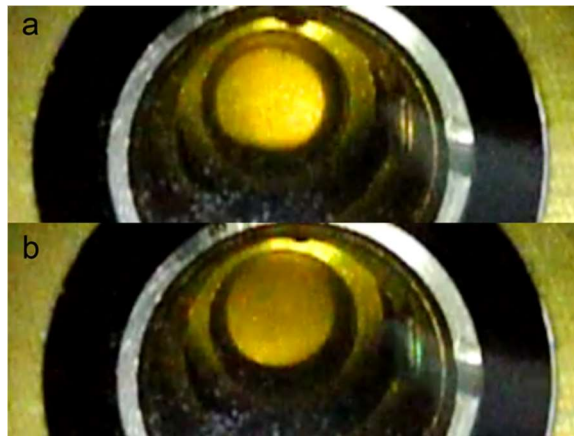
Figure 5.13. Untilted disc (a) and tilted disc (b)

Another feature of the measurements is the varying seating distance. This is especially apparent in Figure 5.8. The disc is not constrained from rotation and therefore does not necessarily seat normal to the x-axis. This can lead to slight variations in the measured position of the seated disc.

Inclination of the disc may lead to some error in the measured position. If this were the case, wobbling of the disc would result in an oscillatory position measurement. High speed camera footage also shows the disc bouncing in the x-direction. Therefore, the effect of each phenomenon cannot be captured independently. Additionally, small air bubbles can be seen in the oil. This changes the effective refractive index of the fluid, further

contributing to noise in the measurements. Despite these disturbances, the oscillations in the position measurements are on the order of 0.1 mm. While measurements were not taken using the high speed camera, qualitatively, the magnitude of oscillations in the actual disc appear to be on the order of the measured oscillations. It should be noted that no cavitation was observed or measured.

5.5   Reed Valve

5.5.1   Experimental Setup

The reed valve experimental setup, shown in Figure 5.14, is identical to the disc valve setup with the exception of the check valves and manifolds. While not shown in Figure 5.14, the LVDT was connected to the piston during experiments as shown in Figure 5.5. The pump experimental parameters are the same as those provided in Table 5.1. To measure the reed valve opening, an acrylic sight glass was installed in the check valve manifolds to allow for optical access as shown in Figure 5.15.
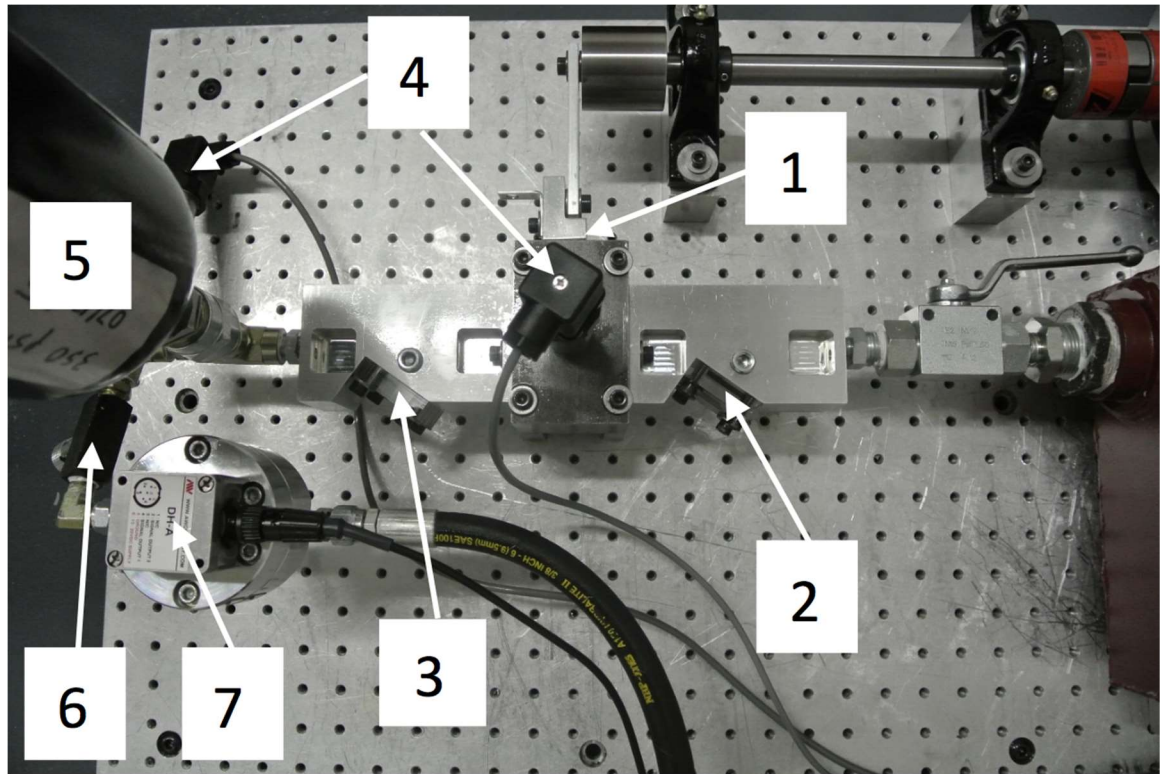
Figure 5.14. Instrumented experimental setup consisting of a (1) piston, (2) inlet reed check valve, (3) delivery check valve, (4) cylinder and load pressure transducers (5) accumulator, (6) needle valve, and (7) gear flow meter.
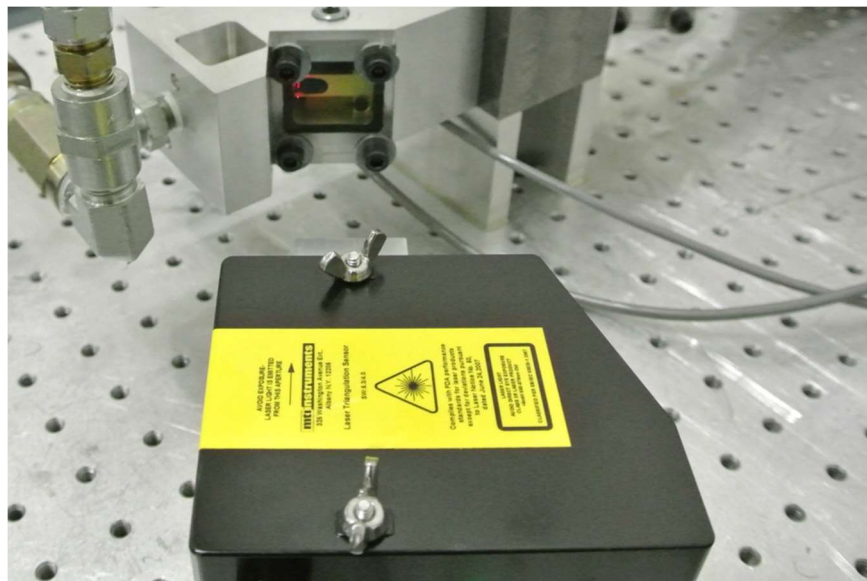

Figure 5.15. Laser triangulation sensor measurement of reed tip position.

5.5.2 Experimental Methods

Rather than run a baseline, high pressure, and high speed test, as was done with the disc valve pump, the load pressure was kept constant while the speed was varied for the reed valve experiments. Experiments were conducted at three speeds as summarized in Table 5.5. A total of six experiments were conducted: three measuring the inlet valve position at each condition and three measuring the delivery valve.

Table 5.5. Reed valve experiment conditions.

Condition	Pump Speed (rpm)	Mean load pressure (MPa)
Low Speed	595	2.76 – 2.93
Medium Speed	743	2.76 – 2.86
High Speed	893	2.72 – 3.03

To begin, the needle valve was opened and the variable frequency drive was set to the desired speed. Once the pump speed reached steady state, the needle valve was gradually closed until the accumulator pressure reached approximately 2.76 MPa. Variability in the load pressure was observed due to the coarse adjustment of the needle valve. The pump was allowed to run until it reached cyclic steady state before data was taken. Cyclic steady state was identified by a constant flow rate through the gear flow meter, indicating no net flow into or out of the accumulator over a cycle.

As with the disc valve experiments, the mean load pressure varied slightly between inlet and delivery valve experiments, while the speed was relatively constant. Also, no leakage or increase in oil temperature was observed during experiments.

5.5.3 Estimation of Fluid Displacement Area

Determining the rate of fluid displacement by reed motion analytically is not a straightforward task. The reed valve seat has several grooves creating many possible flow paths and obstructions. Thus, the most appropriate values of f_1 and f_2 are therefore A_Q are unclear. As a result, estimates are obtained from experimental data. The first step is to

recognize what effect each parameter has on reed motion during pumping. Note that during opening where $u > 0$

$$A_Q(u) = A_1 + f_2(A_2 - A_1) \tag{5.12}$$

and during closing where $u < 0$

$$A_Q(u) = A_1 + f_1(A_2 - A_1) \tag{5.13}$$

The parameter f_1 affects valve behavior during closing whereas f_2 affects opening behavior. It turns of that pump delivery is significantly more affected by closing behavior than opening so that f_1 has a large effect of pump delivery while f_2 hardly influences it. Measured pump delivery can therefore be used to estimate f_1.

A larger value of f_2 simulates the reed displacing a large amount of fluid during valve opening. This creates a fast change in net flow into or out of the cylinder, and a larger corresponding change in cylinder pressure which opposes valve motion. A similar effect is observed during closing but to a much lesser extent so that f_1 has a relatively small influence on the valve closing profile. Therefore, measured valve position can be used to estimate f_2.

The ability to isolate the effects of model parameters improves the ability to estimate their values based on experimental data. Still, tuned values require physical interpretation and testing across a range of conditions to demonstrate predictive valve. Through a process of tuning to match measured pump delivery and reed valve position, the values of f_1 and f_2 were estimated to be 0.22 and 0.35 respectively. Physically, this means the reed creates a larger net fluid displacement during opening than closing. Note these values are specific to the reed valve geometry used to derive them and may have limited applicability in terms of operating conditions.

5.5.4   Valve Opening Results

As with the disc valve, modeled and measured reed valve position data is compared visually by plotting. Figure 5.16 through Figure 5.18 shows the inlet valve reed tip position over three pumping cycles for the conditions given in Table 5.5. Similarly, delivery valve position is shown in Figure 5.19 through Figure 5.21.

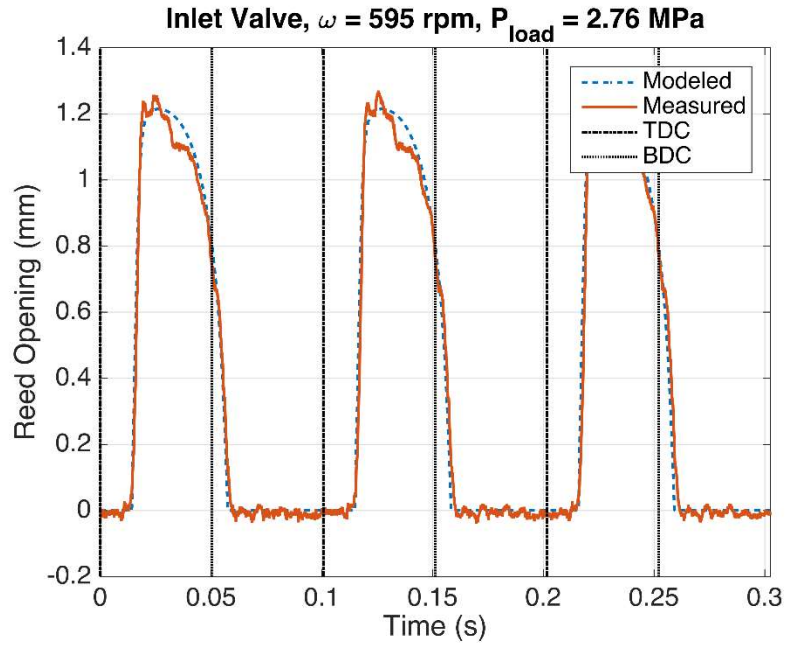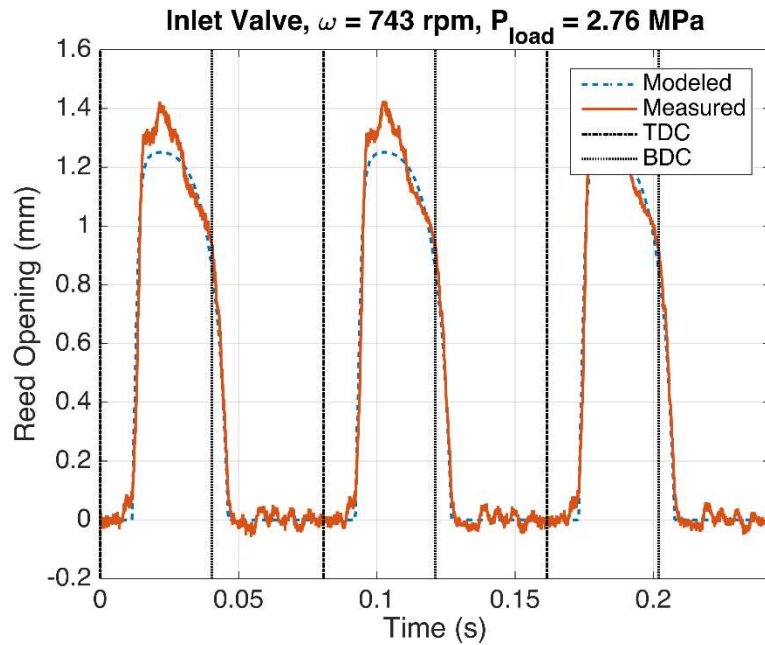Figure 5.16. Inlet valve reed tip position – low speed case.

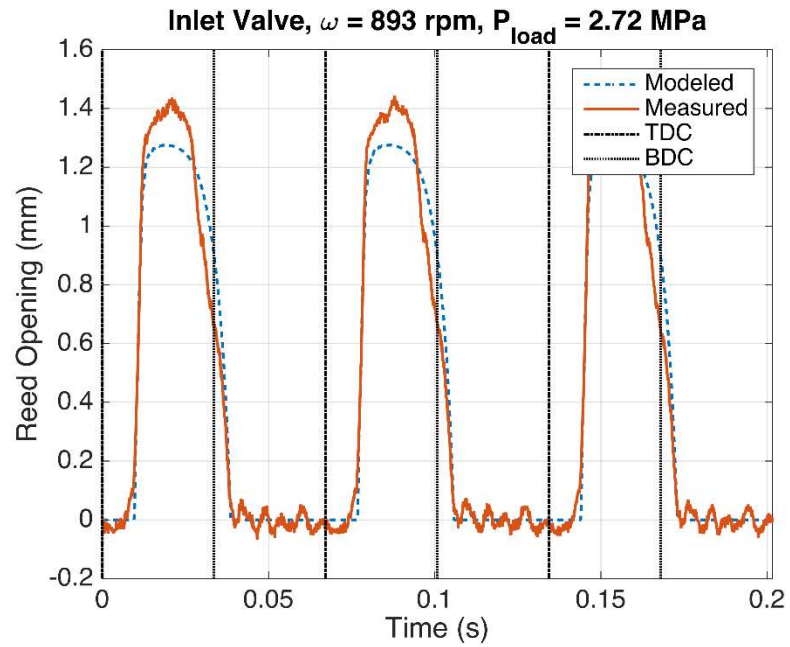Figure 5.17. Inlet valve reed tip position – medium speed case.

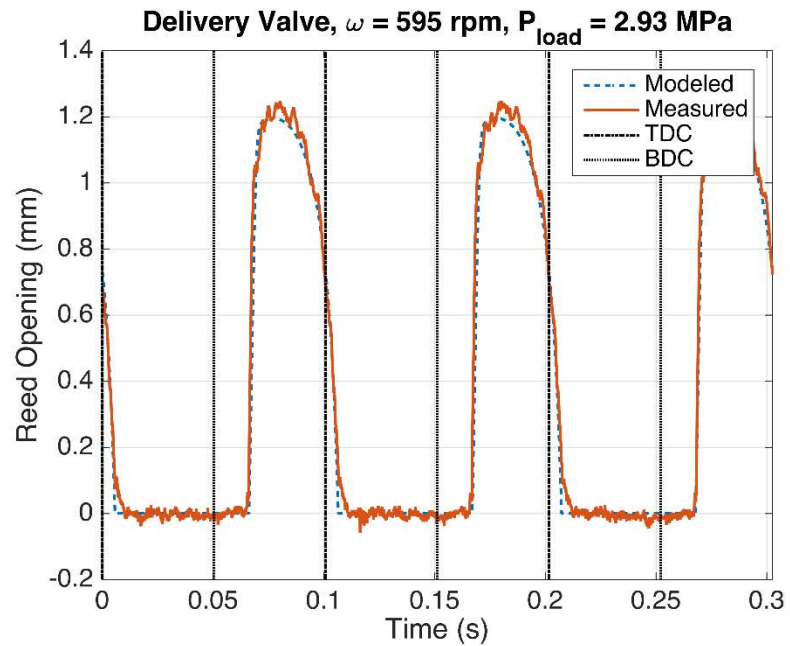Figure 5.18. Inlet valve reed tip position – high speed case.

Figure 5.19. Delivery valve reed tip position – low speed case.
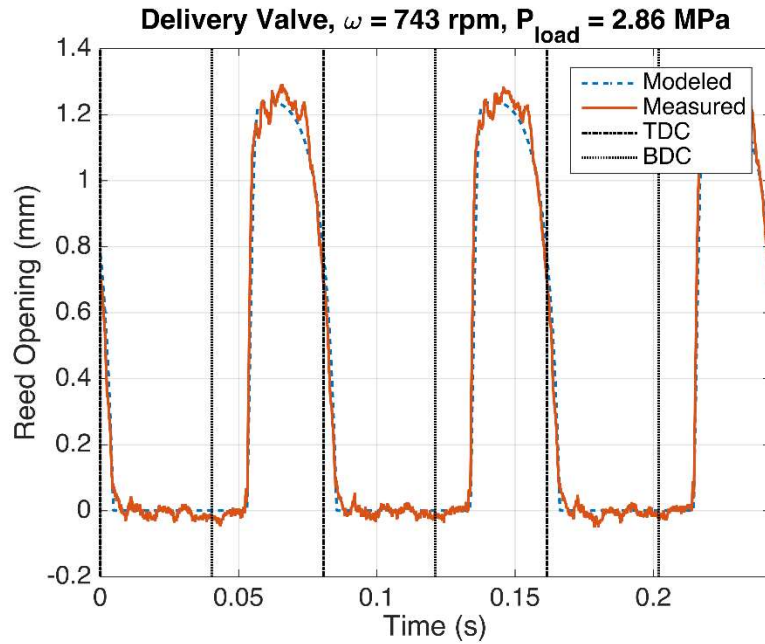
Figure 5.20. Delivery valve reed tip position – medium speed case.
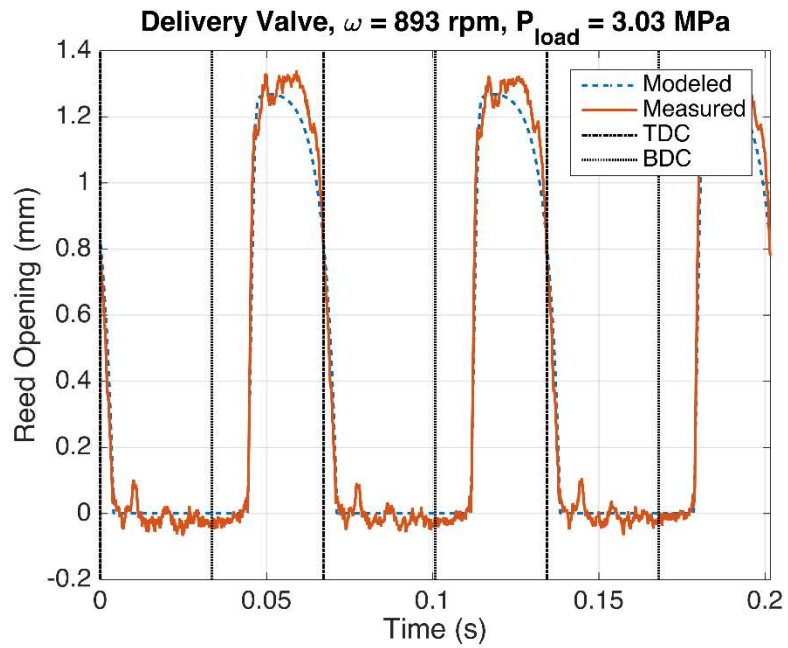
Figure 5.21. Delivery valve reed tip position – high speed case

5.5.5 Pump Delivery Results

Table 5.6 summarizes the measured and modeled reed valve pump delivery for the three conditions listed in Table 5.5.

Table 5.6. Reed valve pump delivery (cc/rev) – measured and modeled

Experiment Conditions	Air Content, R	Inlet Reed Valve Measured		
		Measured	Modeled	% Error
Low speed, 595 rpm, 2.76 MPa	0.008	1.683	1.693	+0.594
Medium speed, 743 rpm, 2.76 MPa	0.008	1.680	1.682	+0.119
High speed, 893 rpm, 2.72 MPa	0.008	1.675	1.673	–0.119
Experiment Conditions	Air Content, R	Delivery Reed Valve Measured		
		Measured	Modeled	% Error
Low speed, 595 rpm, 2.93 MPa	0.008	1.736	1.688	–2.765
Medium speed, 743 rpm, 2.86 MPa	0.008	1.686	1.679	–0.415
High speed, 893 rpm, 3.03 MPa	0.008	1.648	1.664	+0.971

5.5.6   Discussion

Agreement between the modeled and measured reed opening is quite good in all six cases presented, with the possible exception of the inlet valve high speed case (Figure 5.18), although the timing of the opening and closing transition events are still captured well in that case. There are several possible sources, both in the model and experiments, for the discrepancies observed.

First, the pressure and flow dynamics in a pump are quite complex. A lumped parameter approach, while favorable due to its simplicity and relatively low computational expense, cannot be expected to capture all the physics of the system. At best, it can predict some metrics the modeler may care about such as reed transition timing, maximum opening, and volumetric efficiency.

Second, consider the LTS measurements and how they may differ from the actual reed valve opening. During its operation, the single cylinder pump induced moderate vibration of the experimental setup. The effects of vibrations in the test setup are not captured by the model and therefore have a bearing on model agreement with experimental

results. Nonetheless, experiments have shown that a simple, semi-empirical reed valve model can capture the behavior of reed valves in a pumping circuit with a high degree of accuracy.

Error in the pump delivery was less than 3% in all cases. This reveals several things about the model. First is that the reed position is not so tightly coupled to the average flow rate that error in one will necessarily induce error in the other. For example, the worst agreement in reed opening profile was for the inlet reed at 893 rpm, which corresponded to excellent agreement in the pump delivery. Second, application of the steady state orifice equation is a good approximation across the range of conditions in this study. It seems likely that careful, experimental measurement of the discharge coefficient contributes significantly to the accuracy of the flow rate model.

5.6   Computational Expense

Pump model simulations were run on a computer having a 2.6 GHz Intel Core i5 processor and 8 GB of 1600 MHz DDR3 memory. The Adam-Bashforth numerical method was used for integration so data from the previous time step was kept in memory. A convergence study was performed with pump delivery as the variable by which convergence was assessed. For the experimental conditions simulated in this thesis, a time step of 0.5 μs was used to ensure convergence. At each time step, iteration is required to calculate the cylinder and orifice flow rate. A tolerance of 10^{-5} was chosen for the former and 10^{-4} for the latter. The pump model reached cyclic steady state within two revolutions so each pumping simulation was run for five revolutions to obtain three revolutions of steady state data. With these settings, 23 s of computing time was required to simulate 1 s of pumping.

Chapter 6 Conclusion

6.1   Review

Chapter 1 presented a literature review of modeling techniques for disc and reed style check valves. Discussion of check valve modeling was divided into the mechanical and fluid domain. The primary finding was that while disc valve modeling has been well established in hydraulic systems, modeling of reed valves has been limited to applications with a gaseous working fluid. Finally, check valve model validation techniques were discussed with the focus on direct measurement of valve motion. Based on the findings of Chapter 1, the need for a hydraulic reed valve modeling approach and non-invasive method of validation was identified and represent the primary contribution of this thesis.

In Chapter 2, a computationally inexpensive, analytical disc valve modeling approach was discussed in detail. The modeling approach was presented in the context of a specific disc valve architecture that would later be used for experimental model validation. While Chapter 2 does not represent a primary contribution of this thesis, it lays the groundwork for the modeling and experimental validation techniques that were applied to hydraulic reed valves.

Chapter 3 presented a computationally inexpensive, analytical reed valve modeling approach. The reed valve equation of motion was developed from Euler-Bernoulli beam theory, while the flow rate model was developed from the steady state orifice equation. Much of Chapter 3 dealt with techniques for calculating parameters that define a reed valve. A computationally efficient method of characterizing the three dimensional pressure distribution on a reed was presented. The modeling approach for a general reed valve architecture was developed and applied to a specific reed valve that would later be used for experimental model validation.

A piston pump was chosen as the circuit in which the disc and reed check valve models would be experimentally validated. Chapter 4 described a lumped parameter, mass conservative pump model with a focus on accounting for fluid compressibility. The pump

model was developed to correspond with an experimental pump setup that would be used for check valve model validation.

Chapter 5 described the experimental setup comprised of a piston pump instrumented to measure pump and check valve behavior. The check valve model validation approach was discussed including details of the instrumented pump and experimental methods. A novel, non-contact method of measuring check valve motion in hydraulic circuits during operation was presented along with an uncertainty analysis. The metrics chosen for model validation were check valve position and pump delivery. Finally, a comparison between the predicted and experimentally measured metrics showed good agreement.

6.2   Conclusions

Based on experimental validation, both the disc and reed style check valve models presented in this thesis have been shown to accurately predict the timing of opening and closing events. Both the best and worst agreement in valve opening was observed in the delivery reed valve experiments.

Figures 5.18 and 5.19 show the range agreement between modeled and measured reed tip position. The disc valve hit the stop during every simulation and experiment while the reed valve never did. Generally, the reed valve model predicted the maximum opening quite well, with the maximum error, seen in Figure 5.18, being less than 10%.

Pump delivery was predicted with less than 5% error in the disc valve cases and less than 3% in the reed valve cases. The ability to predict pump delivery is evidence that the flow rate is captured well by the valve models. The flow rate model relies an empirical discharge coefficient correlation to achieve such high predictive value.

The LTS based experimental validation approach presented in this work is capable of measuring valve position at frequencies up to 40 kHz through multiple interfaces, including acrylic and hydraulic oil, with an uncertainty of approximately 1.12%. However, other quantities such as pressure distribution and three dimensional valve dynamics were not captured.

The computing resources currently available to most designers limit the complexity a check valve model may have while remaining computationally inexpensive in terms of an optimization routine. Assumptions and simplifications that are used to lower the computational expense of a check valve model also limit how well the complex physics involved in check valve operation can be simulated. Experimental results showed such limitations in the check valve models presented in this work. Physical phenomena not accurately captured include opening speed, finer details of opening and closing profiles, and three dimensional valve dynamics. To properly use a check valve model for predictive analysis, it is imperative that the limitations are understood.

6.3   Recommendations for Future Work

Modeling and application of reed valves in hydraulic systems has been little explored compared to more traditional poppet, disc, and ball style valves. This thesis contributes a mathematical modeling approach and an experimental validation strategy, but there is room for improvement and expansion of the research. Future research should focus not only on improvement of the modeling approach presented in this thesis, but also on different modeling approaches such as those based on finite element methods and computational fluid dynamics.

In future work, the model presented in this thesis should be expanded to predict the disc wobble and reed torsion and their effects on valve response and flow rate. A more accurate method for calculating stiction and flow forces, such as utilizing computational fluid dynamics, would improve estimates of their relative significance and effect on valve dynamics. Implementing a predictive rather than empirical method of calculating the discharge coefficient and pressure load multiplier correlations would aid in valve optimization. Validation over a wider range of operating conditions, valve architectures, and circuit types would increase confidence in the model.

As long as computational resources are a limiting factor in design and optimization, trade-offs must be made between speed, and complexity. Several possible courses of action exist to bridge the gap. First, sensitivity analyses should be done to identify the physical phenomena that have the greatest effect on valve behavior and focus on capturing their

effects in the model. Second, methods should be developed to collapse larger data sets from experiments and CFD simulations into compact forms for implementation in a computationally inexpensive models. Finally, improved valve designs that mitigate undesirable physical effects, such as stiction, should be explored to not only improve valve performance but simplify modeling.

Finally, applications should be identified in which a reed valves present a benefit over more traditional check valve types. Reed valve models should be implemented in optimization routines in a wide range of applications to realize their potential advantages.

Bibliography

Angeletti, a et al., 2009. Optimisation of reed valves dynamics by means of Fluid Structure Interaction Modelling. *Structure*, (July).

Battistoni, M. & Grimaldi, C.N., 2005. Fluid Dynamic 1D Modeling for the Design Optimization of Reed Valve Devices in Secondary Air Injection Applications Fluid Dynamic 1D Modeling for the Design Optimization of Reed Valve Devices in Secondary Air Injection Applicati. In *7th International Conference on Engines for Automobiles*.

Baudille, R. & Biancolini, M.E., 2008. A general approach for studying the motion of a cantilever beam interacting with a 2D fluid flow. , 1(4), pp.449–465.

Baudille, R., Biancolini, M.E. & Mottola, E., 2009. Non-linear models of reed valve dynamics. *Int. J. Vehicle Systems Modelling and Testing*, 4(3), pp.150–184.

Bredesen, A.M., 1974. Computer Simulation of Valve Dynamics as an Aid to Design. In *International Compressor Engineering Conference School*. pp. 171–177.

Buchanan, H.J. & Shih, C.C., 1971. The drag on oscillating flat plates in liquids at low Reynolds numbers. *Journal of Fluid Mechanics*, 48, pp.229–239.

Bukac, H., 2002. Understanding Valve Dynamics. *International Compressor Engineering Conference*. Available at: http://docs.lib.purdue.edu/icec/1564.

Cho, B.B.-H., Lee, H.H.-W. & Oh, J.-S.J., 2002. Estimation technique of air content in automatic transmission fluid by measuring effective bulk modulus. *International journal of automotive technology*, 3(2), pp.57–61. Available at: http://210.101.116.115/fisita/pdf/A103.pdf.

Costagliola, M., 1949. *Dynamics of a reed type valve*. Available at: http://dspace.mit.edu/handle/1721.1/12752.

Dave, A. et al., 2004. Development of a reed valve model for engine simulations for two-stroke engines. *SAE Technical Papers*, (724). Available at: http://dx.doi.org/10.4271/2004-01-1455.

Edge, K.A., Brett, P.N. & Leahy, J.C., 1984. Digital Computer Simulation as an Aid in Improving the Performance of Positive Displacement Pumps with Self-Acting Valves. *Proceedings of the Institution of Mechanical Engineers, Part B: Journal of Engineering Manufacture*, 198(14), pp.267–274.

Exxon Mobil Corporation, 2001. Mobil DTE 20 Series. , p.3. Available at: http://www.chemcorp.co.uk/creo_files/upload/related-items/mobil_dte_20.pdf [Accessed June 16, 2016].

Van Eysden, C.A. & Sader, J.E., 2006. Resonant frequencies of a rectangular cantilever beam immersed in a fluid. *Journal of Applied Physics*, 100(11).

Ferreira, R.T.S., Deschamps, C.J. & Prata, A.T., 1989. Pressure distribution along valve reeds of hermetic compressors. *Experimental Thermal and Fluid Science*, 2(2), pp.201–207.

Gere, J.M. & Timoshenko, S.P., 1997. *Mechanics of Materials* Fourth., Boston, MA: PWS Publishing Company. Available at: http://books.google.com/books?hl=en&lr=&id=PVA8AAAAQBAJ&oi=fnd&pg=P R3&dq=Mechanics+of+Materials&ots=6wz7OB1uK1&sig=fKUbxuIyEMxKu0DV u099XcGk37E.

Habing, R.A., 2005. *Flow and plate motion in compressor valves*, Available at: http://doc.utwente.nl/50744/1/thesis_Habing.pdf.

Hamrock, B.J., Schmid, S.R. & Jacobson, B.O., 2004. *Fundamentals of Fluid Film Lubrication, Second Edition*,

Han, S.M., Benaroya, H. & Wei, T., 1999. Dynamics of Transversely Vibrating Beams Using Four Engineering Theories. *Journal of Sound and Vibration*, 225(5), pp.935–988. Available at: http://www.sciencedirect.com/science/article/pii/S0022460X99922575.

Jajcevic, D. et al., 2010. Reed Valve CFD Simulation of a 2-Stroke Engine Using a 2D Model Including the Complete Engine Geometry. , 3(2), pp.448–461.

Jalil, J.M. et al., 2015. Experimental and numerical investigation of fluid flow of truncated conical poppet valve. *International Journal of Fluid Power*, 16, pp.25–34. Available at: http://www.tandfonline.com/doi/abs/10.1080/14399776.2015.1017360.

Jinghong, Y., Zhaoneng, C. & Yuanzhang, L., 1994. The Variation of Oil Effective Bulk Modulus With Pressure in Hydraulic Systems. *Journal of Dynamic Systems, Measurement, and Control*, 116(1), p.146. Available at: http://link.aip.org/link/?JDS/116/146/1.

Johnston, D.N., 1991. Numerical Modelling of Reciprocating Pumps with Self-Acting

Valves. *Proceedings of the Institution of Mechanical Engineers, Part I: Journal of Systems and Control Engineering*, 205, pp.87–96.

Johnston, D.N., Edge, K. a & Vaughan, N.D., 1991. Experimental investigation of flow and force characteristics of hydraulic poppet and disc valves. *ARCHIVE: Proceedings of the Institution of Mechanical Engineers, Part A: Journal of Power and Energy 1990-1996 (vols 204-210)*, 205(31), pp.161–171. Available at: http://archive.pepublishing.com/openurl.asp?genre=article&id=doi:10.1243/PIME_PROC_1991_205_025_02.

Knutson, A.L. & Van de Ven, J.D., 2016a. MODELING AND EXPERIMENTAL VALIDATION OF A REED CHECK VALVE FOR HYDRAULIC APPLICATIONS. In *Proceedings of the ASME/BATH Symposium on Fluid Power & Motion Control*.

Knutson, A.L. & Van de Ven, J.D., 2016b. Modelling and experimental validation of the displacement of a check valve in a hydraulic piston pump. *International Journal of Fluid Power*, 9776(March), pp.1–11. Available at: http://www.tandfonline.com/doi/full/10.1080/14399776.2016.1160718.

Leati, E., Gradl, C. & Scheidl, R., 2016. Modeling of a Fast Plate Type Hydraulic Check Valve. *Journal of Dynamic Systems, Measurement, and Control*, 138(6). Available at: http://dynamicsystems.asmedigitalcollection.asme.org/article.aspx?doi=10.1115/1.4032826.

Love, L., Lanke, E. & Alles, P., 2012. *Estimating the Impact (Energy, Emissions and Economics) of the US Fluid Power Industry*,

Ludu, A., Betto, A. & Regner, G., 2000. Endoscope video of compressor valve motion and pressure measurement assist simulations for design improvements. In *International Compressor Engineering Conference*. pp. 443–450. Available at: http://docs.lib.purdue.edu/icec/1420.

Machu, G. et al., 2004. a Universal Simulation Tool for Reed Valve Dynamics. *Engineering Conference Purdue*, pp.1–8.

Manring, N.D., 2005. *Hydraulic Control Systems*, John Wiley & Sons.

Merritt, H.E., 1967. *Hydraulic Control Systems*, John Wiley & Sons.

Naguleswaran, S., 2002. Natural Frequencies, Sensitivity and Mode Shape Details of an

Euler–Bernoulli Beam With One-Step Change in Cross-Section and With Ends on Classical Supports. *Journal of Sound and Vibration*, 252(4), pp.751–767. Available at: http://linkinghub.elsevier.com/retrieve/pii/S0022460X01937435.

Naik, T., Longmire, E.K. & Mantell, S.C., 2003. Dynamic response of a cantilever in liquid near a solid wall. *Sensors and Actuators, A: Physical*, 102(3), pp.240–254.

Peterson, J.P. & Peterson, R.B., 2006. Laser Triangulation for Liquid Film Thickness Measurements through Multiple Interfaces. *Applied Optics*, 45(20), pp.4916–4926.

Prasad, B.. G.S. & Woollatt, D., 2000. Valve dynamic measurements in a VIP compressor. In *International Compressor Engineering Conference*. pp. 361–368. Available at: http://docs.lib.purdue.edu/icec/1408.

Roemer, D.B. et al., 2015. Fluid Stiction Modeling for Quickly Separating Plates Considering the Liquid Tensile Strength. *Journal of Fluids Engineering*, 137(6), p.061205. Available at: http://fluidsengineering.asmedigitalcollection.asme.org/article.aspx?doi=10.1115/1.4 029683.

Rothbauer, R.J. et al., 2007. Reed Valve , Crankcase and Exhaust Models Coupled to 3D Fluid Domains for the Predictive CFD Simulation. *Sae Paper 2007-32-0030*, 20076530, pp.1–12.

Sanada, K. et al., 1993. A finite element model of hydraulic pipelines using an optimized interlacing grid system. *Proceedings of the Institution of Mechanical Engineers, Part I: Journal of Systems and Control Engineering*, 207(4), pp.213–222.

Scheidl, R. & Gradl, C., 2016. An Approximate Computational Method for the Fluid Stiction Problem of Two Separating Parallel Plates With Cavitation. *Journal of Fluids Engineering*, 138(6), p.061301. Available at: http://www.scopus.com/inward/record.url?eid=2-s2.0-84958818311&partnerID=tZOtx3y1.

Scheidl, R. & Gradl, C., 2015. MODELING AND DESIGN OF A CUSHIONING GROOVE CONSIDERING A SLANTING IMPACT. In *Proceedings of the ASME/BATH 2015 Symposium on Fluid Power and Motion Control*. pp. 1–8.

Singh, P.J. & Madavan, N.K., 1987. Complete Analysis and Simulation of Reciprocating Pumps Including Piping System. In *Fourth International Pump Symposium*. pp. 55–

73.

Soedel, W. & Cohen, R.-, 1976. A General Method for Simulating the Flow Dependent Nonlinear Vibrations of Compressor Reed Valves. , pp.930–934.

Tarnopolsky, A.Z., Fletcher, N.H. & Lai, J.C.S., 2000. Oscillating reed valves - An experimental study. *Journal of the Acoustical Society of America*, 108(1), pp.400–406. Available at: <Go to ISI>://000088054100037.

Traill-Nash, R.W. & Collar, A.R., 1953. The effects of shear flexibility and rotatory inertia on the bending vibrations of beams. *Quarterly Journal of Mechanics and Applied Mathematics*, 6(2), pp.186–222.

Vaughn, N.D., Johnston, D.N. & Edge, K.A., 1992. Numerical Simulation of Fluid Flow in Poppet Valves. *Proceedings of the Institution of Mechanical Engineers, Part C: Journal of Mechanical Engineering Science*, 206, pp.119–127.

Del Vescovo, G. & Lippolis, A., 2006. A review analysis of unsteady forces in hydraulic valves. *International Journal of Fluid Power*, 7(3), pp.29–39.

Wu, D., Burton, R. & Schoenau, G., 2002. An Empirical Discharge Coefficient Model for Orifice Flow. *International Journal of Fluid Power*, 3(3), pp.13–19. Available at: http://www.tandfonline.com/doi/abs/10.1080/14399776.2002.10781143.

Wylie, E.B., 1984. Simulation of Vaporous and Gaseous Cavitation. *Journal of Fluids Engineering*, 106(3), p.307.

Wylie, E.B. & Streeter, V.L., 1993. *Fluid Transients in Systems*,

Xiong, S. & Lumkes, J.H., 2014. Coupled Physics Modelling for Bi-Directional Check Valve System. *International Journal of Fluid Power*, 15(2), pp.55–67. Available at: http://www.tandfonline.com/doi/abs/10.1080/14399776.2014.897500.

Yudell, A.C. & Van de Ven, J.D., 2015. Predicting solenoid valve spool displacement through current analysis. *International Journal of Fluid Power*, 9776(November), pp.1–8. Available at: http://www.tandfonline.com/doi/full/10.1080/14399776.2015.1068549.

Zeng, Y. et al., 2004. Predicting and Optimizing Two-Stroke Engine Performance Using Multidimensional CFD. , (724).

Appendix A: Calculation of Mobil DTE 25 Hydraulic Oil Viscosity

The viscosity of hydraulic oil depends heavily on its temperature with viscosity decreasing as temperature increases. The Reynolds viscosity-temperature equation is among the simplest viscosity-temperature models and was chosen because only two data points are readily available from the manufacturer. The Reynolds equation gives the temperature dependent dynamic viscosity, μ, as a function of absolute temperature, T:

$$\mu(T) = \mu_0 e^{-bT} \tag{A.1}$$

where μ_0 is a reference viscosity and b is an inverse temperature parameter. The hydraulic oil used in this thesis' experiments is Mobil DTE 25 anti-wear hydraulic oil (Exxon Mobil Corporation 2001). The kinematic viscosity and specific gravity of Mobil DTE 25 oil is listed in Table A.1.

Table A.1. Mobil DTE 25 Hydraulic Oil Properties (Exxon Mobil Corporation 2001)

Property	Symbol	Value	Units
Kinematic viscosity @ 40 °C	v_1	44.2	cSt
Kinematic viscosity @ 100 °C	v_2	6.65	cSt
Specific Gravity @ 15.6° C	SG	0.876	dimensionless

Assuming a constant fluid density for the purposes of viscosity calculation, the inverse temperature parameter is calculated from Equation A.1 as follows:

$$b = \frac{\ln\frac{\mu_1}{\mu_2}}{T_2 - T_1} = \frac{\ln\frac{v_1}{v_2}}{T_2 - T_1} \tag{A.2}$$

Inserting the data from Table A.1 into Equation A.2 gives an inverse temperature parameter of $b = -0.03157$ K^{-1}. From Equation A.1, the reference viscosity may then be solved for as $\mu_0 = \mu_1 e^{bT_1} = \rho_1 v_1 e^{bT_1}$. Noting a density of 876 kg/m^3, the reference viscosity is

therefore 761.1 Pa*s. The temperature dependent dynamic viscosity of Mobil DTE 25 oil is thus modeled as:

$$\mu(T) = (761.1\ Pa * s)e^{-(0.03157\ K^{-1})T} \qquad (A.3)$$

From Equation A.3, the dynamic viscosity of Mobil DTE 25 hydraulic oil at room temperature, taken to be 22 °C, is 0.0683 Pa*s.

Appendix B: Experimental Refractive Index Measurement

The LTS was used to measure the position of the check valve moving element, with the laser beam passing through air, acrylic, oil, back through acrylic, and back through air to the sensor. In order to calibrate the position measurement, the refractive index of hydraulic oil and acrylic were required. Figure B.1 shows the experimental setup used to measure the index of refraction with an LTS.
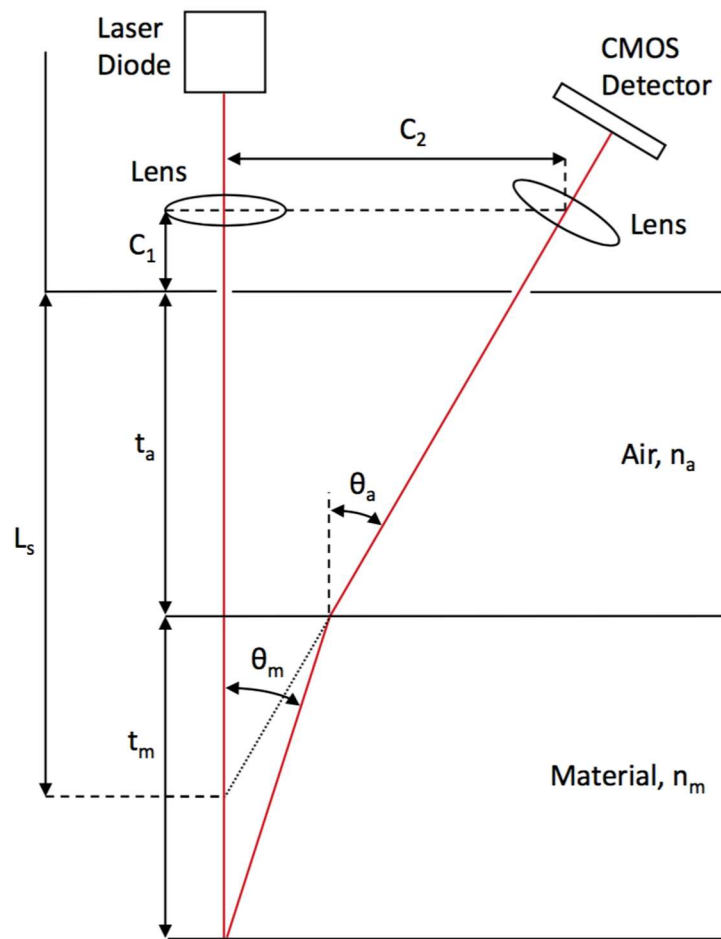

Figure B.1. Experimental setup to measure index of refraction

The laser angle, θ_a, is calculated from the experiment geometry as follows:

$$\theta_a = \tan^{-1}\left(\frac{C_2}{C_1 + L_s}\right) \tag{B.1}$$

where L_s is the standoff length and C_1 and C_2 are constants determined by the LTS geometry. Combining Snell's law and measurements of the experimental setup geometry, the refractive index of the material is calculated as

$$n_m = n_a \sin \theta_a \sqrt{\left[\frac{t_m}{C_2 - (C_1 + t_a)\tan\theta_a}\right]^2 + 1} \tag{B.2}$$

Water and 70% isopropyl alcohol were used to estimate the measurement error. Table B.1 summarizes the measurements used to experimentally determine the refractive indices.

Table B.1. Refractive index experiment measurements.

Symbol	Units	Value
C_1	mm	8.35 ± 0.10
C_2	mm	44.06 ± 0.10
L_s	mm	120 ± 0
n_a	ratio	1.000 ± 0.000
$t_{a,\ water}$	mm	96.12 ± 0.10
t_{water}	mm	32.23 ± 0.20
$t_{a,\ alcohol}$	mm	97.39 ± 0.10
$t_{alcohol}$	mm	32.23 ± 0.20
$t_{a,\ oil}$	mm	98.82 ± 0.10
t_{oil}	mm	32.23 ± 0.20
$t_{a,\ acrylic}$	mm	112.21 ± 0.10
$t_{acrylic}$	mm	12.13 ± 0.05

The results of the refractive index experiments are reported in Table B.2. Uncertainty in the refractive index was calculated from Equation 5.11 using values from Table B.1. The

percent error for water was larger than the estimated uncertainty. This may be due to impurities, as tap water was used rather than distilled.

Table B.2. Refractive index experiment results (Chu and Thompson 1962, Budwig 1994).

Material	Water	Isopropanol, 70%	Hydraulic Oil	Acrylic
Refractive index, n, Measured	1.318 ± 0.9932%	1.387 ± 1.024%	1.476 ± 1.062%	1.509 ± 1.668%
Refractive index, n, Literature	1.3312	1.3742	NA	1.489
% Error	0.997	0.927	NA	1.334

Note that the refractive index of acrylic is readily available in the literature. But, it is a function of the manufacturing technique and thus was determined experimentally.